



## DIPLOMARBEIT

# Ultrasonic resonator for on-line enrichment of functionalized nanoparticles

Ausgeführt am Institut für  
Angewandte Physik  
in Zusammenarbeit mit dem  
Institut für Chemische Technologien und Analytik  
der Technischen Universität Wien

unter der Anleitung von Ao.Univ.-Prof. Dr. Martin Gröschl und Dipl.-Ing. Cosima Koch

durch

Lukas STROBL

2062 Großkadolz 34

---

Datum

---

Unterschrift (Student)

# Table of Contents

Table of Contents .....	1
Symbol nomenclature .....	3
Abstract .....	4
Kurzfassung .....	4
1. Introduction.....	5
1.1. Project synopsis.....	5
1.2. Scientific background .....	5
1.2.1. Fluid dynamics.....	6
1.2.2. Particle manipulation by ultrasonic standing waves.....	7
1.3. COMSOL Multiphysics .....	9
1.3.1. Computational Fluid Dynamics CFD module - laminar flow module (spf) .....	9
1.3.2. Acoustics module - pressure acoustic module (acpr) .....	10
1.3.3. Particle tracing module (fpt) .....	11
1.3.4. Structural mechanics module – Piezoelectric devices (pzd) .....	12
1.4. Laser Doppler vibrometer .....	12
1.5. ICP-OES.....	13
2. Materials and methods .....	14
2.1. Particles.....	14
2.2. Cell 1 design.....	15
2.3. Cell 2 design.....	15
2.4. Ink experiment method.....	17
2.5. Ultrasound equipment .....	18
2.5.1. PZTs .....	18
2.5.2. Conductance measurement .....	19
2.5.3. Frequency Power Synthesizer .....	20

2.6.	Vibrometer experiment.....	20
2.7.	ICP-OES experiments.....	22
2.8.	COMSOL Simulations.....	24
2.8.1.	Fluid dynamics.....	26
2.8.2.	Acoustic Field.....	28
2.8.3.	Particle Manipulation.....	30
3.	Results and discussion.....	33
3.1.	Admittance measurements.....	33
3.1.1.	Choosing the PZTs.....	33
3.1.2.	Preparing the PZTs.....	34
3.2.	Vibrometer measurements.....	41
3.3.	Ink experiments.....	46
3.4.	Simulation results.....	48
3.4.1.	Fluid dynamics.....	48
3.4.2.	Acoustic characteristics.....	49
3.4.3.	Particle manipulation.....	53
3.5.	ICP-OES results.....	62
3.5.1.	Filling the cell.....	62
3.5.2.	0.5 – 2 – 2.5 measurement.....	63
3.5.3.	5 – 9 – 1 measurement.....	65
4.	Conclusion.....	65
5.	Outlook.....	66
	Acknowledgements.....	66
	Bibliography.....	67
	Appendix.....	68

## Symbol nomenclature

There is a mix of two nomenclatures in this thesis. First the introduction equations are kept in accordance with the quoted papers, and second the COMSOL module descriptions are presented with the hard coded equations in COMSOL. To make the equations interchangeable the variables of each equation were explained next to the respective equation. An overview of the used symbols is presented in order of appearance in Table 1.

Symbol	Description	Unit
<b>Fluid dynamics and acoustics variables</b>		
$\partial_t$	Time derivation	
$\rho$	Mass density	kg / m <sup>3</sup>
$v, u$	Velocity	m / s
$T$	Temperature	K
$s$	Entropy per unit mass	J / K
$\sigma'$	Viscous stress tensor	N / m <sup>2</sup>
$\kappa$	Thermal conductivity coefficient	W / m K
$p$	Pressure	Pa
$\eta, \mu$	Dynamic viscosity	Pa s
$\beta$	Viscosity ratio	
$g$	Acceleration of gravity	m / s <sup>2</sup>
$Re$	Reynold number	
$d$	Pipe diameter	m
$F_D$	Drag force	N
$a$	Particle diameter	m
$\langle F_{rad} \rangle$	Time-averaged acoustic axial primary radiation force	N
$\hat{\Phi}$	Velocity potential of the standing wave field	
$k$	Wavenumber	1 / m
$K_s$	Acoustic contrast factor	1 / m
$\lambda$	Wavelength	m
$\sigma$	Ratio of the speeds of sound and the wavenumbers	
$x$	Spatial position in axial direction	m
$i$	Imaginary unit	
$\omega$	Angular frequency	1 / s
$f$	Frequency	Hz
$t$	Time	s
$I$	Identity Matrix	
$F$	Volume Force	N
$q_d$	Acoustic dipole source	N / m <sup>3</sup>
$Q_m$	Acoustic monopole source	1 / s <sup>2</sup>
$c$	Speed of sound	m / s
$m_p$	Particle mass	kg
$Z$	Acoustic Impedance	Pa s / m
<b>Structural mechanics and piezoelectric effect variables</b>		
$u$	Displacement field	m
$\lambda$	Eigenvalue	
$D$	Electric displacement	C / m <sup>2</sup>
$\rho_v$	Free electric charge density	C / m <sup>3</sup>
$\sigma$	Stress	N / m <sup>2</sup>
$c_E$	Elasticity matrix	N / m <sup>2</sup>
$\varepsilon$	Strain	
$e$	Coupling matrix	N / V m
$E$	Electric field	V / m
$\varepsilon_S$	Relative permittivity	

**Table 1: Variable description**

## Abstract

The focus of this thesis is the development of an ultrasonic resonator. The purpose of the resonator is to capture nanoparticles for trace analysis chemistry. The Institute of Applied Physics of the Vienna University of Technology has experience in building ultrasonic resonators and their previous knowledge was used for optimization of possible cells. The focus of the optimization was the flow and acoustic characteristics. A cell with a good flow through characteristic was purchased and equipped with piezo ceramics to be used as an ultrasonic resonator. This prototype was used for simulations and experiments, which showed very good flow characteristics with a syringe pump and a decent acoustic capturing force. In a setting of silica particles (MCM-41) in a 1% HNO<sub>3</sub> suspension flowing through the cell, possible application methods were investigated for trace analysis chemistry with an ICP-OES measurement device.

## Kurzfassung

Der Fokus dieser Arbeit liegt auf der Entwicklung eines Ultraschall Resonators zum Anreichern von Nanopartikeln für die chemische Spurenanalyse. Das Institut für angewandte Physik der Technischen Universität Wien hat bereits Erfahrungen im Bau solcher Zellen, welche zur Optimierung hinsichtlich ihrer Strömungscharakteristik und akustischen Eigenschaften genutzt wurden. Als Ultraschall Resonator wurde eine Quarzglas Durchfluss-Küvette angeschafft und mit Piezo Keramiken ausgestattet. Dieser Prototyp wurde für Simulationen und Experimente verwendet, die sehr gute Strömungseigenschaften mit einer Spritzenpumpe zeigten. Zudem wurde eine annehmbare akustische Schallstrahlungskraft zum Einfangen der Partikel demonstriert. In Experimenten mit Silizium Partikeln (MCM-41) in einer 1% HNO<sub>3</sub> Suspension, die durch die Zelle fließt, wurden mögliche Anwendungsmethoden für die chemische Spurenanalyse mit einem ICP-OES Messgerät untersucht.

# 1. Introduction

The introduction was split into a general project synopsis to explain the project circumstances and a short scientific background of ultrasonic resonators.

## 1.1. Project synopsis

The overall goal is to increase reliability and reproducibility of trace analysis by reducing manual sample handling. The approach of realization was to replace error prone particle enrichment by centrifugation with on-line enrichment in an ultrasonic resonator.

The focus of this thesis is the development of an ultrasonic resonator as part of a project to capture particles with a size of approximately 500 nm up to 3  $\mu\text{m}$  in a water flow. These particles are surface-functionalized silica-oxides (MCM-41) to capture certain analytes for trace analysis chemistry.

Head of the project is Assistant Prof. Dipl.-Ing. Dr.techn. Andreas Limbeck. The main project members are Felix Horak for the chemistry part and me for the physics part. The project members were coordinated by Dipl.-Ing. Cosima Koch. Additionally, Clemens Ditterstorfer was involved in the beginning of the project to characterize possible cell designs and Géza Horváth did fluid dynamic simulations of cells with peristaltic and syringe pumps.

Furthermore, consulting support was always provided by Ao.Univ.-Prof. Dr. Martin Gröschl and Ao.Univ.Prof. Dr. Bernhard Lendl.

## 1.2. Scientific background

Such an ultrasonic resonator, as seen in Figure 1, focuses on optimizing the acoustic radiation force from external ultrasound waves on suspended micro particles, this effect is known as acoustophoresis. Generally speaking it has to find a balance between 3 primary forces: gravity, the water flow drag force and the acoustic radiation force to capture particles. Therefore one has to understand the fluid dynamics and ultrasound fundamentals necessary for such a resonator.

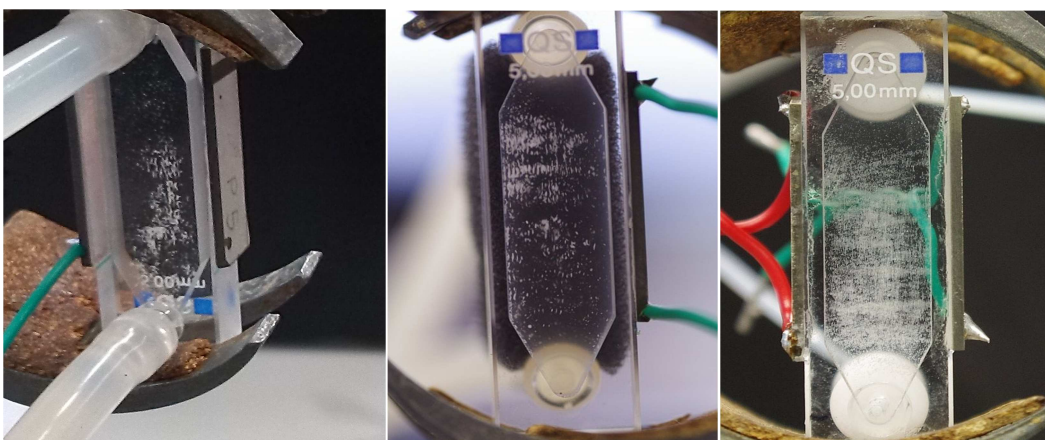


**Figure 1: Pictures of three different piezo ceramics settings with the same cell: At the top and bottom of the cells there are the inlet and outlet in between the particle-water suspension flows through the cells. On the side of the cells there are piezo ceramics powered by a frequency generator to create the acoustic field in which the particles get captured and become visible as white agglomerates.**

### 1.2.1. Fluid dynamics

The governing equations in fluid dynamics relevant for acoustophoresis following the description of Henrik Bruus [1] are:

- **The continuity equation** which expresses the conservation of mass in classical mechanics. Since mass cannot spontaneously appear or disappear in a classical system, a relation exists which links the mass density change over time  $\partial_t \rho$  with the mass density flux ( $\rho * v$ ) using the convection velocity  $v$  in a fixed region.

$$\partial_t \rho = -\nabla(\rho * v) \quad \text{Equation 1}$$

- **The heat-transfer equation** of the fluid which represents the energy conservation in the system. It relates the rate of change of energy density to energy density flux.

$$\rho T [\partial_t s + (v * \nabla) s] = \sigma' : \nabla v + \nabla * (\kappa \nabla T) \quad \text{Equation 2}$$

The left-hand side is density  $\rho$  times temperature  $T$  times the total time derivative of the entropy per unit mass  $s$ , hence it expresses the total gain in heat density per unit time, while the right-hand side represents the sources for heat gain, namely viscous friction and thermal conduction using the viscous stress tensor  $\sigma'$  in a double dot product of two tensors which results in a scalar and the thermal conductivity coefficient  $\kappa$ .

- **The Navier-Stokes equation** which is based on the momentum conservation. In contrast to mass which can only change by advection, momentum can change by convection, body forces that act on the interior of the fixed region (e.g. gravitational and electrical forces) and contact forces that act on the surfaces of the region (e.g. pressure and viscosity forces).

$$\rho [\partial_t v + (v * \nabla) v] = -\nabla p + \eta \nabla^2 v + \beta \eta \nabla(\nabla * v) + \rho g \quad \text{Equation 3}$$

The left side can be interpreted as the inertial force densities, density times the sum of the local and the convective acceleration. The right side is the sum of the intrinsic and applied forces, namely the pressure, convection, viscous friction and gravity forces. The not yet mentioned symbols are the dynamic viscosity  $\eta$  of the fluid, the viscosity ratio  $\beta$  and the acceleration of gravity  $g$ .

The Reynolds number  $Re$  is a dimensionless quantity from rearranging the Navier-Stokes equation to be dimensionless. The Reynolds number characterizes different flow types and is usually used to determine between laminar and turbulent flow. It is defined as the ration between the mean velocity  $v$  times the fluid density  $\rho$  times the pipe diameter  $d$  (or hydraulic diameter in case of non-circular geometry) over the dynamic viscosity  $\eta$  of the fluid.

$$Re = \frac{v * \rho * d}{\eta} \quad \text{Equation 4}$$

The density of water at room temperature is approximately  $\rho = 1000 \text{ kg/m}^3$ , the dynamic viscosity  $\eta = 1000 \text{ Pa*s}$ . The used pump tube has a diameter  $d = 0.13 \text{ mm}$  which results at a flow rate of  $\dot{V} = 1 \text{ ml/min}$  in a mean inlet velocity  $v = \frac{\dot{V}}{A} = \frac{1.67 * 10^{-8} \text{ m}^3/\text{s}}{(0.13 \text{ mm})^2 * \pi / 4} \sim 1 \text{ mm/s}$ .

Therefore our Reynolds number using Equation 4 is  $Re \sim 0.013$  which determines a laminar flow characteristic.

The drag force  $F_D$  for low Reynolds number ( $Re < 1$ ) is also known as Stokes drag, because it is derived from Stokes’ Law which is obtained by linearizing the steady state Navier-Stokes equation. An important example of Stokes flow relates to particle solutions with spherical particles of the diameter  $a$  and a particle velocity  $v_p$  in a water flow (Equation 5).

$$F_D = 6 * \pi * \eta * a * (v - v_p) \quad \text{Equation 5}$$

### 1.2.2. Particle manipulation by ultrasonic standing waves

Particle manipulation with ultrasonic standing waves is a known phenomenon, which is used in multiple applications for concentrating particles at certain locations [2], [3].

Forces are affecting dispersed particles in a carrier medium when an ultrasonic standing wave is applied. The origin of these forces is a spatial distribution of the acoustic pressure amplitude in the standing wave.

For the generation of an ultrasonic standing wave two acoustic waves of equal frequency and amplitude and opposite propagation direction have to interfere with each other. A simple way to realize this condition is an ultrasonic resonator with a transducer as the source of the ultrasonic wave, a carrier medium and a reflector. In Figure 2 the generation of a standing wave in an ultrasonic resonator is shown.

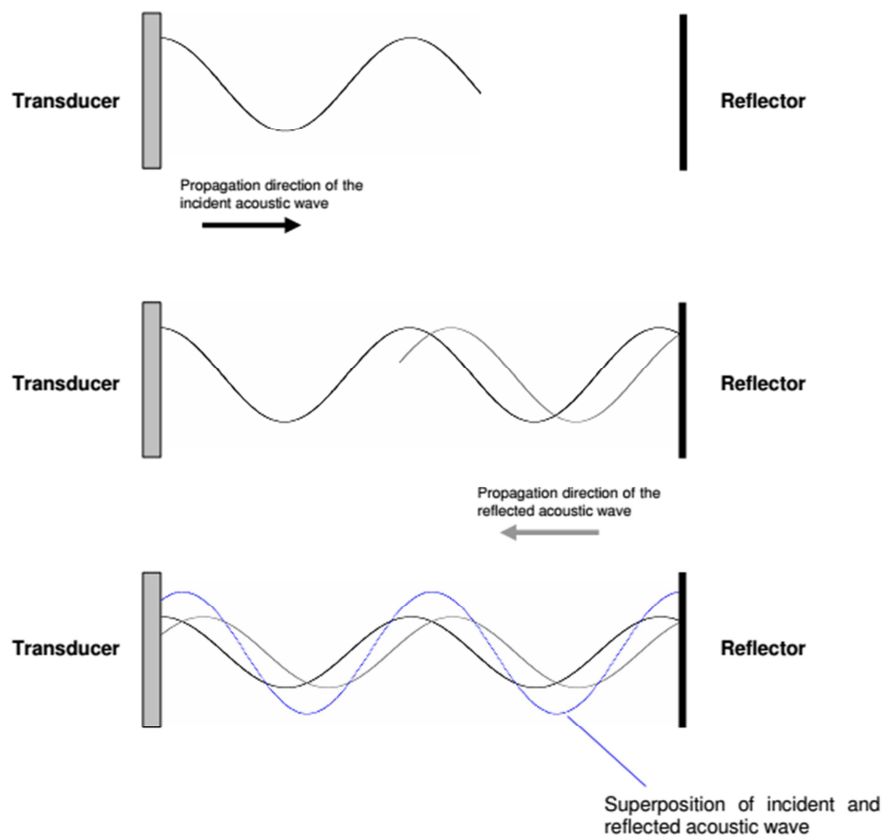


**Figure 2: Generation of a standing wave in an ultrasonic resonator. By courtesy of Dr. Stefan Radel and Dr. Markus Brandstetter [4].**



When the points of equal phase are located in a plane it is called a plane acoustic wave. The pressure nodal and anti-nodal planes are then perpendicular to the propagation direction of the sound waves as seen in Figure 3.

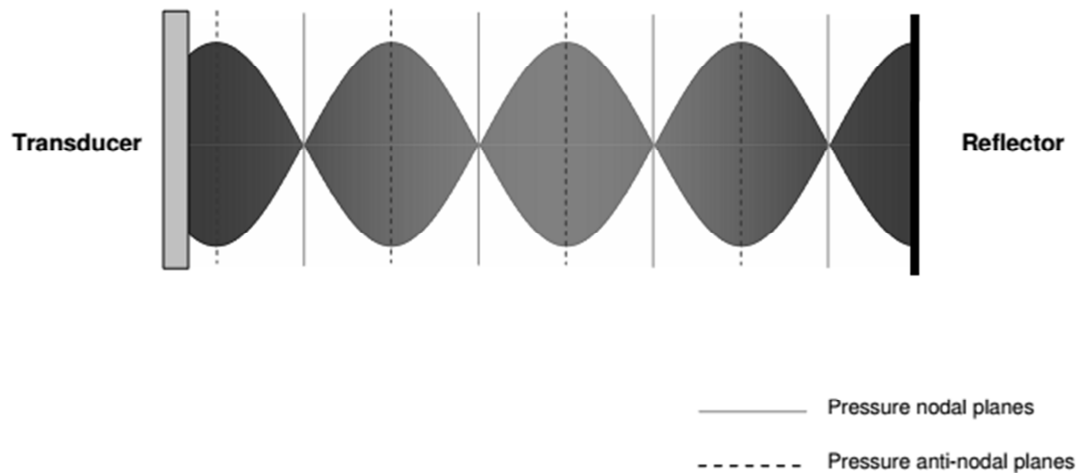


**Figure 3: Planes of an ultrasonic standing wave. By courtesy of Dr. Stefan Radel and Dr. Markus Brandstetter [4].**

This spatial distribution of the acoustic pressure amplitude exerts forces on particles in the acoustic resonator carrier medium. The acoustic properties of the particles and the carrier medium determine the axial forces which push dispersed particles into pressure nodes or pressure anti-nodes of the standing wave dependent on the ratio of the mass densities and the ratio of the sound speeds of particle and carrier medium.

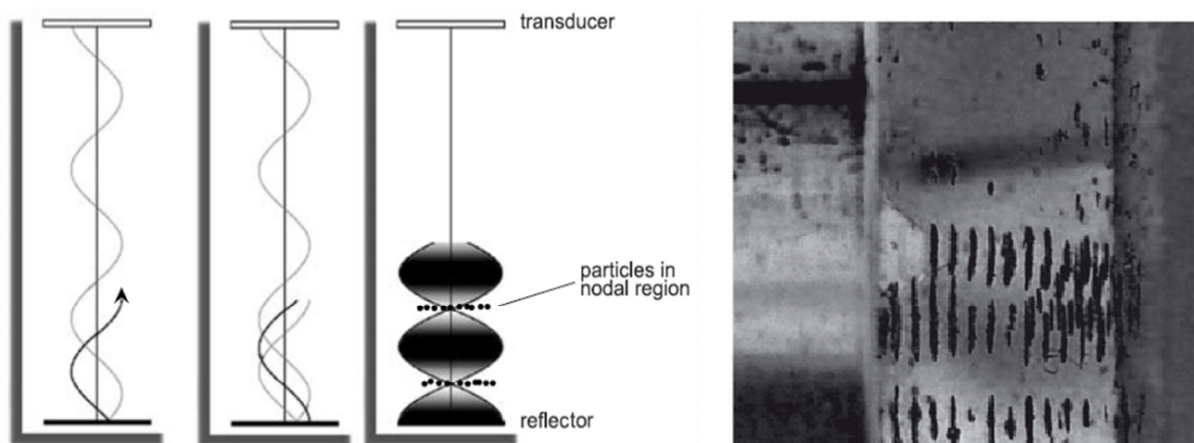


**Figure 4: Left: Development of a standing wave, which leads to the alignment of the particles in the nodal regions. Right: Alignment of particles between the reflector (left side) and the transducer (right side). By courtesy of Dr. Stefan Radel and Markus Brandstetter.**

Gröschl gave a comprehensive description about the theory of particle manipulation by an ultrasonic field and the theoretical aspects important for resonator design in [5], [6].

The first explanation of acoustic forces on a particle suspension was written by King [7]. His assumption was a rigid sphere located in an ideal fluid of zero viscosity which was influenced by a plane ultrasonic standing wave. The result was a non-vanishing axial force on the particles by the acoustic radiation pressure, named axial primary radiation force. Later, Yosioka and Kawasima

extended King’s work to a compressible sphere. [8] This led to the expression for the time-averaged axial primary radiation force  $\langle F_{rad} \rangle$  in a plane standing wave field as seen in Equation 6.

$$\langle F_{rad} \rangle = 4\pi * \rho * \hat{\Phi}^2 * (k * a)^3 * K_s(\lambda, \sigma) * \sin(2kx) \quad \text{Equation 6}$$

for  $ka \ll 1$ ,  $k_0a \ll 1$  and  $\lambda=O(1)$

The used variables are the density  $\rho$  of the compressible sphere, the amplitude of the velocity potential  $\hat{\Phi}$  of the standing wave field, as described in Equation 7, the wavenumber  $k$  of the acoustic wave, the radius  $a$  of the sphere and the acoustic contrast factor  $K_s$  of the respective particle – fluid combination.  $x$  is the spatial position in axial direction, therefore  $F_{rad}$  has a sinusoidal amplitude distribution of half the wavelength of the acoustic field.

The condition  $ka \ll 1$  and  $k_0a \ll 1$  ( $k_0$  is the wavenumber of the acoustic wave in the particle) expresses that the particle diameter  $a$  must be small compared to the acoustic wavelength.

$$\Phi(x, t) = \hat{\Phi}(e^{i(\omega t - kx)} + e^{i(\omega t + kx)}) \quad \text{Equation 7}$$

$$K_s(\lambda, \sigma) = \frac{1}{3} \left( \frac{5\lambda - 2}{2\lambda + 1} - \frac{1}{\lambda\sigma^2} \right) \quad \text{Equation 8}$$

In Equation 8 the mass density ratio  $\lambda = \rho/\rho_0$  of the host fluid ( $\rho$ ) and the particle ( $\rho_0$ ) and  $\sigma = v_0/v = k/k_0$ , the ratio of the speeds of sound and the wavenumbers, are used. The sign of the contrast factor determines if the particles will be pushed into the pressure nodes ( $K_s > 1$ ) or into the anti-nodal region ( $K_s < 1$ ).

The second condition of Equation 6 is  $\lambda = O(1)$ , therefore the mass densities of particle and fluid have to be of the same order of magnitude.

Especially pointed out should be the term  $(ka)^3$  which represents the particle’s volume, hence the particle diameter influences  $F_{rad}$  by the power of three. In comparison, the strength of the standing wave field  $\Phi$ , the contrast factor  $K_s$  and the density of the particle  $\rho$  are of linear influence.

These considerations were adapted to an arbitrary sound field by Gor’kov, who derived an equation for three-dimensional space based on a general radiation force potential.

### 1.3. COMSOL Multiphysics

COMSOL Multiphysics is a simulation program which has the possibility to combine different physics modules into one simulation model.

The modules used for this thesis are described in the following chapters.

#### 1.3.1. Computational Fluid Dynamics CFD module - laminar flow module (spf)

As a short description a direct quote is given from the COMSOL Multiphysics product homepage <http://www.comsol.com/cfd-module>:

“The CFD Module is the platform for simulating devices and systems that involve sophisticated fluid flow models. As is the case with all modules in the COMSOL Product Suite, the CFD Module provides ready-made physics interfaces that are configured to receive model inputs via the graphical user interface (GUI), and to use these inputs to formulate model equations. The particular physics interfaces that the CFD Module is equipped with enable you to model most aspects of fluid flow, including descriptions of compressible, nonisothermal, non-Newtonian, two-phase, and porous media flows – all in the laminar and turbulent flow regimes. The CFD Module can be used as a standard tool for simulating computational fluid dynamics (CFD), or in collaboration with the other modules in the COMSOL Product Suite for multiphysics simulations where fluid flow is important.

The CFD Module GUI grants you full access to all steps in the modeling process. This includes the following steps:

- Selecting the appropriate description of the flow, for example single-phase or two-phase, laminar or turbulent flows, etc.
- Creating or importing the model geometry
- Defining the fluid properties
- Adding source and sink terms, or editing the underlying equations of the fluid model, if required
- Selecting mesh elements and controlling the density of the mesh at different positions
- Selecting solvers and tuning them, if required”

The used equation is the stationary Navier-Stokes Equation for a compressible Newtonian fluid:

$$\rho(\mathbf{u} \cdot \nabla)\mathbf{u} = \nabla \cdot [-p\mathbf{I} + \mu(\nabla\mathbf{u} + (\nabla\mathbf{u})^T - \frac{2}{3}\mu(\nabla \cdot \mathbf{u})\mathbf{I})] + \mathbf{F} \quad \text{Equation 9}$$

$$\nabla \cdot (\rho\mathbf{u}) = 0 \quad \text{Equation 10}$$

where

$\rho$  is the density (SI unit: kg/m<sup>3</sup>)

$\mathbf{u}$  is the velocity vector (SI unit: m/s), previously noted in chapter 1.2.1 as  $\mathbf{v}$

$p$  is pressure (SI unit: Pa)

$\mu$  is the dynamic viscosity (SI unit: Pa·s)

$\mathbf{F}$  is the volume force vector (SI unit: N/m<sup>3</sup>)

$\mathbf{I}$  is the identity matrix

### 1.3.2. Acoustics module - pressure acoustic module (acpr)

As a short description a direct quote is given from the COMSOL Multiphysics product homepage <http://www.comsol.com/acoustics-module>:

“The Acoustics Module is designed specifically for those who work with devices that produce, measure, and utilize acoustic waves. Application areas include speakers, microphones, hearing aids,

and sonar devices, to name a few. Noise control can be addressed in muffler design, sound barriers, and building acoustic applications.

Straightforward user interfaces provide tools for modeling acoustic pressure wave propagation in air, water, and other fluids. Dedicated modeling tools for thermoacoustics enable highly accurate simulation of miniaturized speakers and microphones in handheld devices. You can also model vibrations and elastic waves in solids, piezoelectric materials, and poroelastic structures. Multiphysics interfaces for acoustic-solid, acoustic-shell, and piezo-acoustics bring your acoustic simulations to a new level of predictive power.”

The used equation is an inhomogeneous Helmholtz equation:

$$\nabla * \frac{1}{\rho_c} (\nabla p_t - \mathbf{q}_d) - \frac{k_{eq}^2 p_t}{\rho_c} = Q_m \quad \text{Equation 11}$$

$$p_t = p + p_b \quad \text{Equation 12}$$

$$k_{eq}^2 = \left(\frac{\omega}{c_c}\right)^2 - k_z^2 \quad \text{Equation 13}$$

The subscript  $c$  on the density  $\rho$  and the speed of sound  $c$  expresses that they may be complex numbers. The wave number  $k_{eq}$  contains both the ordinary wave number  $k$  as well as out-of-plane and circumferential contributions. Note also that the pressure is here the total pressure  $p_t$  which is the sum of the background pressure field  $p_b$  and scattered field  $p$ . There are two optional source terms: the dipole source  $q_d$  (SI unit: N/m<sup>3</sup>) and the monopole source  $Q_m$  (SI unit: 1/s<sup>2</sup>).  $\omega = 2\pi f$  (rad/s) is the angular frequency.

### 1.3.3. Particle tracing module (fpt)

As a short description a direct quote is given from the COMSOL Multiphysics product homepage <http://www.comsol.com/particle-tracing-module>:

“The Particle Tracing Module extends the functionality of the COMSOL environment for computing the trajectory of particles in a fluid or electromagnetic field, including particle-particle and particle-field interactions. You can seamlessly combine any application-specific module with the Particle Tracing Module for computing the fields that drive particle motion. Particles can have mass or be mass-less. The movement is governed by either the Newtonian, Lagrangian, or Hamiltonian formulations from classical mechanics. Boundary conditions can be imposed on the particles on the walls of the geometry to allow particles to freeze, stick, bounce, disappear, or reflect diffusely. User-defined wall conditions may also be specified, where the post collision particle velocity is typically a function of the incoming particle velocity and the wall normal vector. Secondary particles released when an incoming particle strikes a wall can be included. The number of secondary particles and their velocity distribution function can be functions of the primary particle velocity and the wall geometry. Particles can also stick to the wall according to an arbitrary expression or a sticking probability. Additional dependent variables can be added to the model which allows you to compute quantities like particle mass, temperature, or spin.

Particles can be released on boundaries and domains uniformly, according to the underlying mesh, as defined by a grid or according to an arbitrary expression. A wide range of predefined forces is

available to describe specifically how the particles interact with the fields. You can then add arbitrary forces as defined by a suitable expression. It is also possible to model the two-way interaction between the particles and the fields (particle-field interaction), as well as the interaction of particles between each other (particle-particle interaction).”

The used equation is Newton’s second law:

$$\frac{d(m_p * \mathbf{v})}{dt} = \mathbf{F}_t \quad \text{Equation 14}$$

Where  $m_p$  is the particle mass (SI unit: kg),  $\mathbf{v}$  is the particle velocity (SI unit: m/s) and  $\mathbf{F}_t$  is the force exerted on the particle (SI unit: N).

### 1.3.4. Structural mechanics module – Piezoelectric devices (pzd)

As a short description a direct quote is given from the COMSOL Multiphysics product homepage <http://www.comsol.com/structural-mechanics-module>:

“The Structural Mechanics Module is dedicated to the analysis of mechanical structures that are subject to static or dynamic loads. You can use it for a wide range of analysis types, including stationary, transient, eigenmode/modal, parametric, quasi-static, frequency-response, buckling, and prestressed.”

The used equations are:

$$-\rho\omega^2\mathbf{u} - \nabla * \sigma = \mathbf{F}v \quad \text{Equation 15}$$

$$-i\omega = \lambda \quad \text{Equation 16}$$

$$\nabla * \mathbf{D} = \rho_v \quad \text{Equation 17}$$

$$\sigma = c_E \varepsilon - e^T \mathbf{E} \quad \text{Equation 18}$$

$$\mathbf{D} = e \varepsilon + \varepsilon_S \mathbf{E} \quad \text{Equation 19}$$

The naming convention differs in piezoelectricity theory (Equation 18 and Equation 19) compared to structural mechanics theory, but the piezoelectric devices interface uses the structural mechanics nomenclature in COMSOL. The strain is named  $\varepsilon$  instead of  $S$ , and the stress is named  $\sigma$  instead of  $T$ . This makes the names consistent with those used in the other COMSOL structural mechanics interfaces. Furthermore,  $\rho$  is the density,  $\omega$  is the angular frequency,  $\mathbf{u}$  is the displacement field,  $\mathbf{F}$  is the volume body force,  $v$  is the velocity,  $\lambda$  is the eigenvalue,  $\mathbf{D}$  is the electric displacement,  $\rho_v$  is the free electric charge density,  $c_E$  is the elasticity matrix,  $e$  is the coupling matrix,  $\mathbf{E}$  is the electric field and  $\varepsilon_S$  is the relative permittivity.

## 1.4. Laser Doppler vibrometer

A Laser Doppler vibrometer is able to measure the Doppler shift of a vibrating surface without contact. It is possible to measure the vibration frequency and amplitude from the Doppler shift of the laser reflection of a moving surface to the original laser beam through interference. A strongly reflecting surface of the target is necessary for good signal processing. The basic principle is shown in

Figure 5 with the addition of a usually built in Bragg cell for a known additional frequency shift. The output of the photo detector is a frequency modulated signal with the Bragg cell frequency as carrier and the Doppler shift as modulation frequency which can be demodulated to derive the velocity vs. time of the vibrating target.

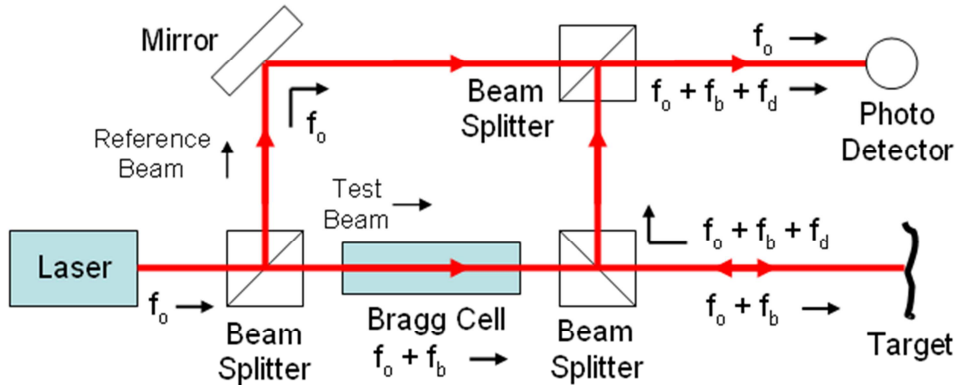


**Figure 5: Principle of a Laser Doppler vibrometer.**  
 [source: [http://en.wikipedia.org/wiki/File:LDV\\_Schematic.png](http://en.wikipedia.org/wiki/File:LDV_Schematic.png)]

### 1.5. ICP-OES

The inductively coupled plasma optical emission spectrometry (ICP-OES) is an analytical method used in trace analysis. It uses inductively coupled plasma to excite atoms and ions which emit electromagnetic radiation at distinct wavelength characteristic for particular elements, where the intensity correlates with the concentration of the sample. Figure 6 illustrates the different parts which process the liquid analyte to become an aerosol excitable by the plasma flame and hence deliver a signal at the detector.

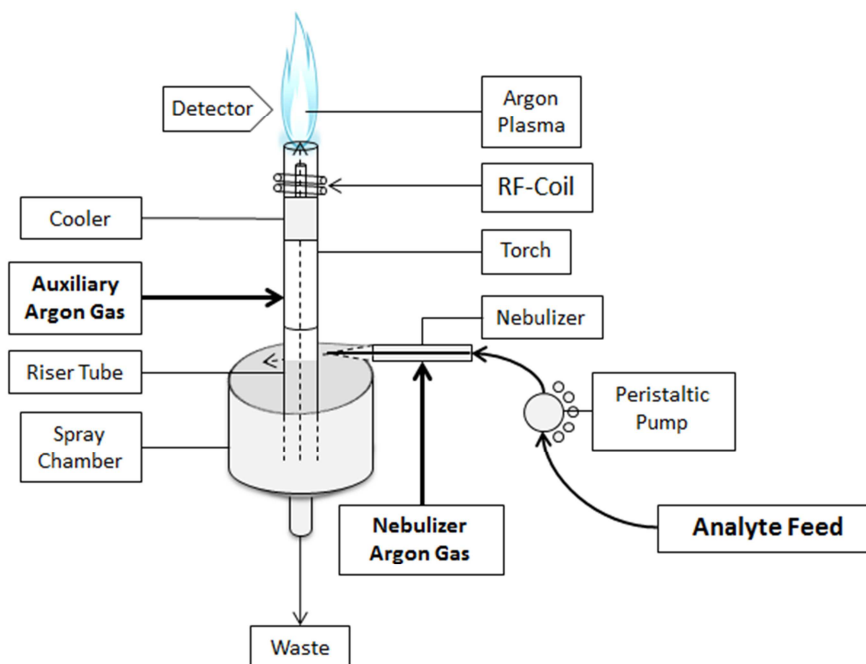


**Figure 6: Schematic of an ICP-OES measurement device. By courtesy of Felix Horak.**

## 2. Materials and methods

### 2.1. Particles

Felix Horak synthesized a batch of porous silicon particles (MCM-41) [9] which are surface functionalized for bonding with different analytes (i.e. zircon) particles [10]. Later it was discovered that the zircon did not bond with the silicon particles but built other structures distributed in the sample. A small sample of the silicon particles was coated with gold for measurement with a scanning electron microscope (SEM) to investigate the size distribution. The result is shown in Figure 7, the particles displayed a size spread from 500 to 1000 nm and a tendency to group together as agglomerates. The density of the silicon particles was estimated with around  $1300 \text{ kg/m}^3$  due to their porosity.

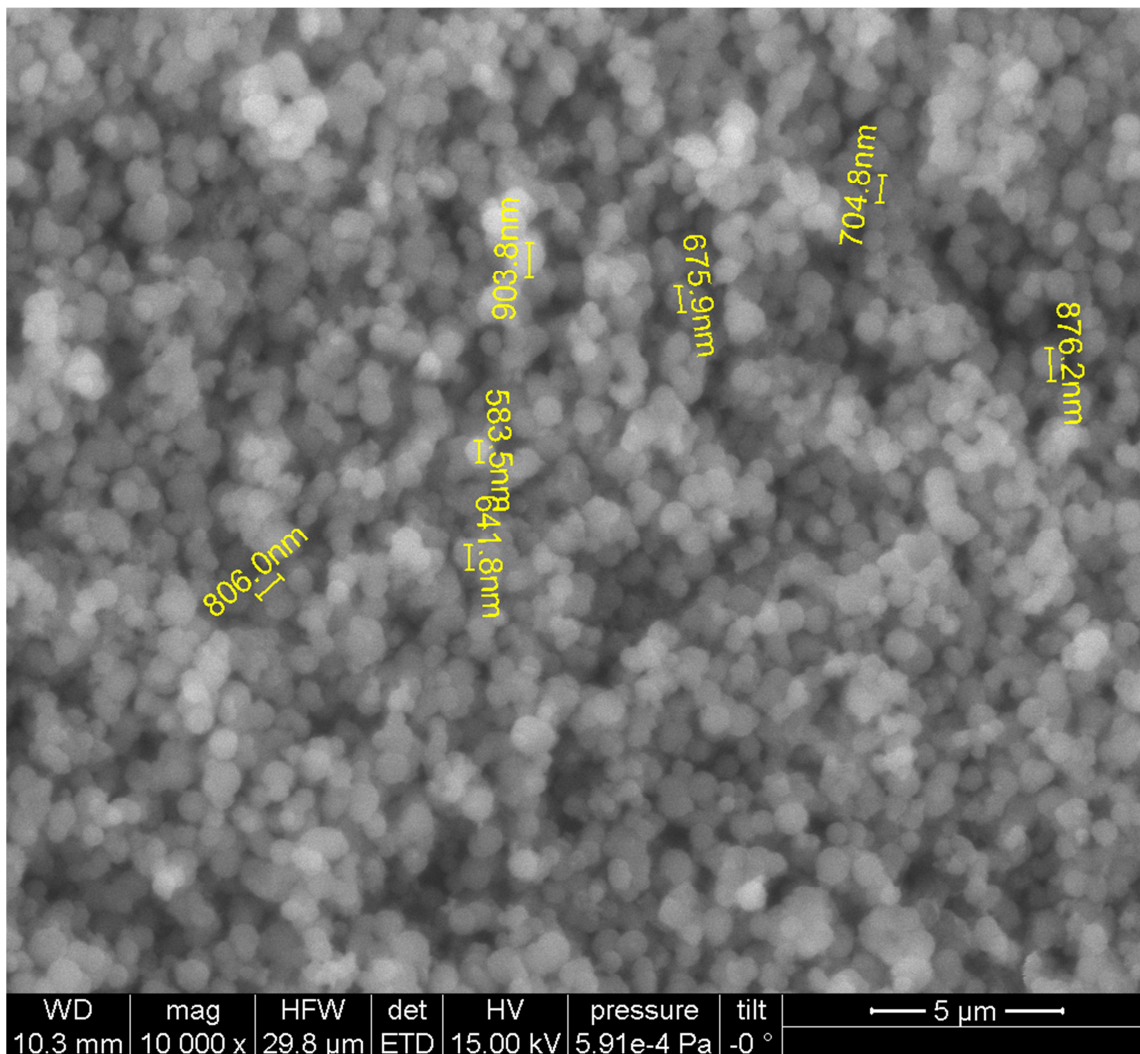


**Figure 7: SEM pictures with estimate of particle diameters and agglomerates of MCM-41 particles.  
By courtesy of Felix Horak**

## 2.2. Cell 1 design

This cell was purchased from Wagner & Munz GmbH at the beginning of my contribution to the project and was the basis for experiments and simulations in this thesis. It was chosen due to its good flowthrough characteristics and the volume capacity of 1.3 mL which was considered to be a good match for the ICP-OES pump speed of 1 mL/min. A picture from the cell including its measurements is illustrated in Figure 8.

• [Durchfluss-Küvette, Makro, mit Zu- und Abfluss-Stutzen \(Absorptionsmessung\) , T](#)



Abbildung kann vom Original abweichen

Bestell-Nr.: 137540

Preis auf Anfrage

für 1 Stück zzgl. gesetzl. MwSt. (19%) zzgl. Versandkosten

Durchfluss-Küvette, Makro, mit Zu- und Abfluss-Stutzen (Absorptionsmessung) ,  
 Typ: 137-QS ,  
 Material: Quarzglas SUPRASIL® ,  
 Schichtdicke mm: 5 ,  
 Außenmaße H x B x T mm: 45 x 12,5 x 7,5 ,  
 Apertur HxB mm oder Durchmesser: 20 x 9 ,  
 Volumen µl: 1300

(-) Technische Daten:

Schichtdicke: 5 mm

Material: Quarzglas

Artikel-Nr: 137-5-40

Warengruppe: ›

[Durchflussküvette](#)

Schlagworte: ›

[Durchflussküvette](#)

Packung (groß): 1 Stück

Gültigkeit: 31.12.2014

Letztes Update: 03.01.2014

Figure 8: The cell from the Wagner & Munz GmbH homepage with its measurements.

## 2.3. Cell 2 design

This cell was developed based on Cell 1 with the idea of a better acoustic field by using a material with a similar acoustic impedance to water for the narrowing to the inlet and outlet. Additionally the inlet and outlet should be placed in a way that all particles have to go diagonally across the nodal planes of the acoustic field when flowing through.

A possible material for such an impedance match is polydimethylsiloxane (PDMS) as described in [11]. It has acoustic impedance 30% below water as seen in Table 2 and was chosen due to its relative cheap price and good availability.

	PDMS	Water
Speed of sound $c$ [m/s]	1019	1484
Density $\rho$ [kg/m <sup>3</sup> ]	1028	1000
Acoustic impedance $Z=\rho*c$ [kg/(m <sup>2</sup> s)]	1.05E+06	1.48E+06

Table 2: Comparison of relevant acoustic parameters from PDMS and Water at 25°C.

The geometry of cell2 was chosen to have an end volume of approximately 1mL and the wall thickness was chosen based on the considerations in [6] for an optimized acoustic field in the water volume, transducer carrier wall and reflector wall as shortly explained below.

### Carrier wall thickness



The frequency range between the eigenfrequencies of the piezoceramic and carrier composite delivers the best performance numbers. Therefore the total phase shift of the acoustic wave between the outer boundary surfaces of the transducer would ideally be an odd multiple of  $\pi/2$  of the resonator operating frequency. (At the transducer eigenfrequencies the phase shift is equal to a multiple of  $\pi$ .) This phase shift condition implies Equation 20 as criteria for the optimal wall thickness of the carrier  $L_c$  depended on the operating frequency  $f_0$  and the speed of sound of the used material.

$$L_c = \frac{(2n - 1) * v}{2 * f_0} \tag{Equation 20}$$

Reflector wall thickness

To minimize power loss in the reflector, no eigenfrequencies of the reflector should appear within the resonator operating frequency range. Therefore the reflector thickness  $L_r$  should be close to an odd multiple of a quarter wavelength of the acoustic wave in the reflector material.

$$L_c = \frac{(2n - 1) * v}{4 * f_0} \tag{Equation 21}$$

Equation 20 and Equation 21 were used to plot the ideal wall thicknesses for two chosen frequencies ( $f_1=1.96$  MHz and  $f_2= 6.67$  MHz) considering that the material used for cell2 should be aluminum with a speed of sound  $v=6420$  m/s.

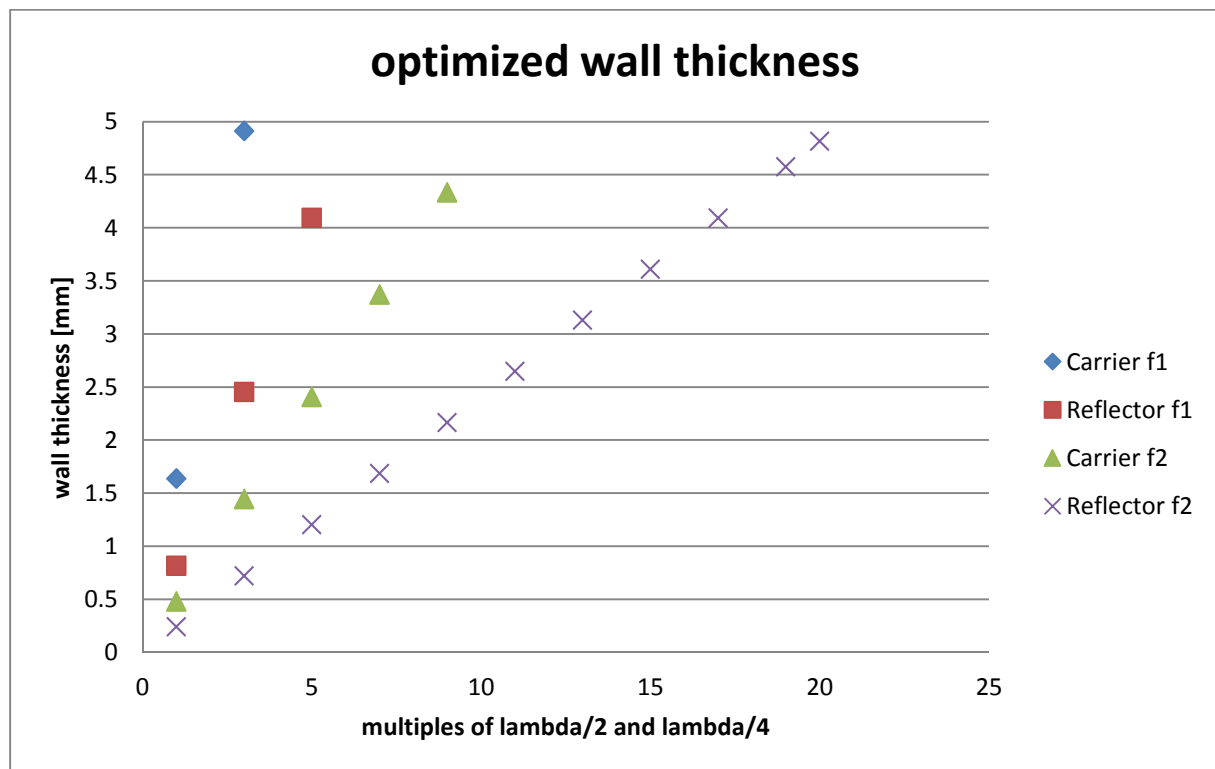


**Figure 9: optimized values of wall thickness for the frequencies  $f_1= 1.96$  MHz and  $f_2= 6.67$  MHz and a speed of sound for aluminum of  $v= 6420$  m/s.**

The decision fell on a wall thickness of 2.4 mm because of a minimum necessary structural strength for handling and production of the cell, as well as the closeness of the 6 MHz carrier value of 2.41 mm and reflector of 2.17 mm and 2.65 mm. The reason for a higher prioritization of the 6 MHz

peak is the greater difficulty of powering that resonance practically and that the 2 MHz peak range is usually broader.

The length of the cell was given by the PZT length of at least 25 mm plus a few mm for rounded corners and the height of the cell was chosen similar to Cell1 with 7 mm for reusability of the PZT pieces. The width should be as wide as possible to have a maximum amount of pressure nodes and therefore more potential to capture particles. Since the volume with included PDMS wedges should be approximately 1 mL, a width with 10.2 mm was chosen. The complete assembly can be seen in Figure 10, the construction drawing is in the appendix (Figure 77).

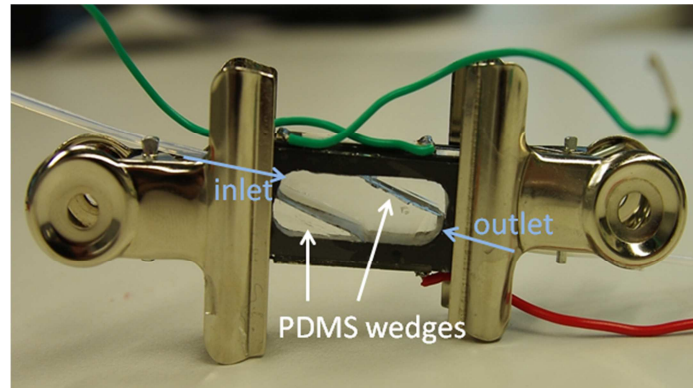


**Figure 10: Picture of Cell2 assembly with PDMS wedges. By courtesy of Felix Horak.**

To make sure the liquid is not absorbing too much power, a short calculation was done to estimate the power loss in the liquid layer.

The absorption coefficient  $\alpha$  is calculated as shown in Equation 22 by using the parameters for water at room temperature:  $\rho=1000 \text{ kg/m}^3$ ,  $\mu=10^{-3} \text{ kg/ms}$ ,  $\mu'=2.4\mu$ ,  $v=1500 \text{ m/s}$ .

$$\alpha = \frac{(2\pi f_0)^2 * (\mu' + 4\mu/3)}{2 * \rho * v^3} \quad \text{Equation 22}$$

Therefore the coefficients at the frequencies of  $f_1=2 \text{ MHz}$  and  $f_2=6 \text{ MHz}$  are  $\alpha_1(2\text{MHz}) = 0,087/\text{m}$  and  $\alpha_2(6\text{MHz}) = 0,786/\text{m}$ . Assuming a power  $P_0 = 1 \text{ W}$  and a width of  $x=10 \text{ mm}$  the power dissipation over the liquid layer is the following:

$$\mathbf{2MHz: P(x) = P_0 * e^{-\alpha_1 x} = 0,999W} \quad \text{Equation 23}$$

$$\mathbf{6MHz: P(x) = P_0 * e^{-\alpha_2 x} = 0,992W} \quad \text{Equation 24}$$

The values are less than 1% deviation from the initial power and therefore insignificant for our purposes.

## 2.4. Ink experiment method

Some ink experiments were previously performed by Clemens Ditterstorfer and Felix Horak with the purpose of finding cells with good fluid dynamics in the sense that there should not be any dead volume with low flow where particles could get trapped and not flushed out when necessary.

After I joined the project, a new cell was purchased from Wagner & Munz GmbH as seen in Figure 8. With this cell the three of us repeated ink experiments to characterize the fluid dynamics. The setup of these experiments is shown in Figure 11.

The used peristaltic pump has two speed settings (“rabbit” and “turtle”) which were both used for the ink experiments and depending on the tube diameter determined the volume flow amount. The two speed settings correspond to the two simulated velocity field choices.

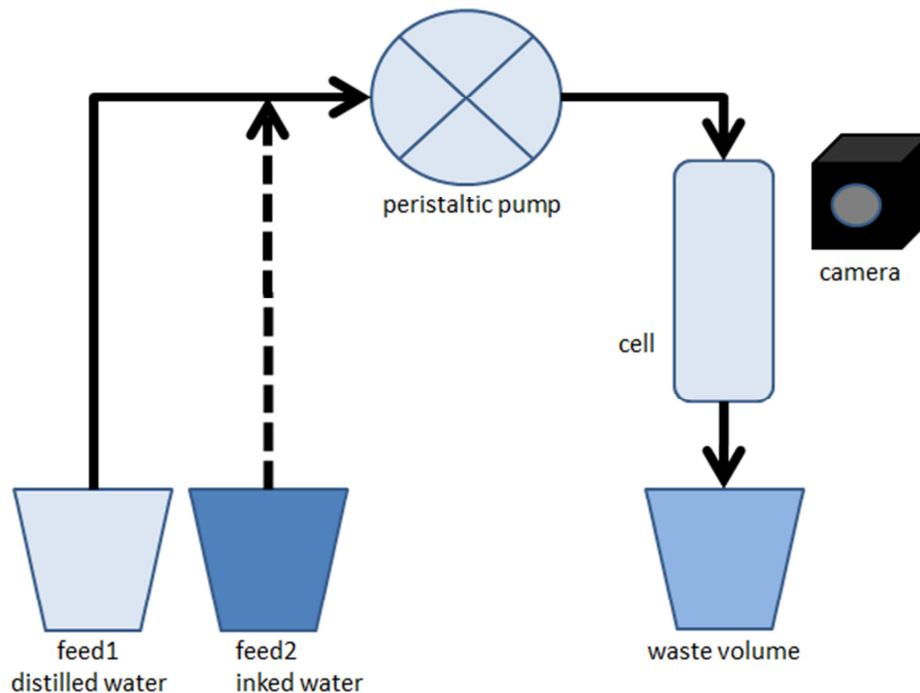


**Figure 11: Ink experiment setup**

The experiment was done following these steps:

- First the cell and the tubing was filled with distilled water avoiding air bubbles
- Stop the peristaltic pump
- Change to the inked water feed
- Start the pump and only fill the tube before the cell
- Stop pump and change back to distilled water feed
- Set up camera to make picture series
- Start pump and camera

## ***2.5. Ultrasound equipment***

### **2.5.1. PZTs**

The ultrasonic waves are generated with piezoelectric materials, which work in a similar manner as conventional loudspeakers. If an electric field is applied to a piezoelectric material it responds with an internal mechanical force which leads to either contraction or expansion of the material. If the electric field is periodic, the expansion also changes periodic and so it can be used as transducer.

Our chosen piezoelectric material is a PZT, which is a composite of lead, circonate and titanate. As seen in Figure 12 it is a 1 mm thick plate with wrap around electrodes with a length and width of 25mm and the electrodes are made of silver. Since the cells were smaller than 25 mm we had to

break it into smaller pieces as seen in Figure 12 by scratching it with a glass cutter and breaking over an edge.

They were purchased from Physik Instrumente(PI) Ceramic GmbH & Co. KG (Lederhose, Germany) and depending on the thickness the main resonance frequency is around 2 MHz for the chosen hard PZT type PIC181. It has a high curie temperature which is advantageous for soldering and gluing in an oven. One should first solder wires on the PZT and then glue it on the desired surface due to a possible sensitivity of the glue to the soldering temperature.

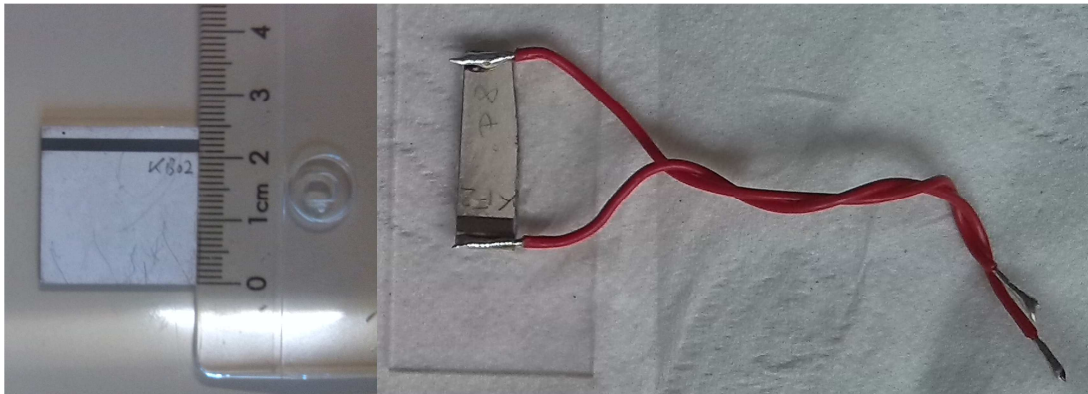


**Figure 12: Pictures of our PZTs. On the left an unused PZT, on the right a broken off piece of such a PZT, first soldered wires on the electrodes to power it and then glued to a glass plate.**

## 2.5.2. Conductance measurement

The resonance frequencies of a PZT are usually visualized in a conductance spectrum, each peak in such a spectrum is a mechanical and electrical resonance of the current setting. The conductance ( $G$ ) is the real part of the admittance ( $Y$ ), which is the inverse of the impedance ( $Z$ ) as noted in Equation 25. The conductance is measured in Siemens and the impedance in Ohm. In Figure 13 the used impedance analyzer (16777k, SinePhase Instruments) is shown in a possible setup how a conductance spectrum of a PZT is measured.

$$Y = \frac{1}{Z} \quad ; \quad Y = G + jB \quad \text{Equation 25}$$



**Figure 13: Picture of the Impedance Analyzer 16777k (SinePhase Instruments, Hinterbrühl, Austria) which is used to measure the conductance spectra of the PZTs.**

### 2.5.3. Frequency Power Synthesizer

At the laboratory there are two Frequency Power Synthesizer, the FPS4025 and the FPS2540. They have both the same design but an additional circuit to limit the power output to 2.5 W was added to the FPS2540. Therefore the FPS2540 (Figure 14) has a more detailed range and is usually used to power the PZTs. A general rule of thumb is to maximally drive a PZT with 1 W per 1 mL of water volume to avoid excessive heating.

Additionally, a third frequency generator (Sonosep Controller SC 010, SinePhase Instruments) was purchased since the before mentioned are not able to power the higher frequency resonances at around 6 MHz. One has to be careful with its power output for the higher frequency since it uses an internal frequency doubling mechanism to reach them; therefore the displayed power is only half of the actual power!



Figure 14: Picture of FPS2540 which is used to power the PZTs.

## 2.6. Vibrometer experiment

The vibrometer experiments were performed to decide which glue should be used for fixing the PZTs to the cells. For this purpose two test glue samples were created with an epoxy resin –glue (Duralco 4700 HT) and commercial super-glue (Loctite Superkleber PowerGel) on a small aluminum piece (both 2.9mm thick) to measure the different damping characteristics. The vibrometer is a Polytec MSA-400 (Micro System Analyzer) running the PSV Scanning Vibrometer Software 8.8.

The method of the experiment was to fix the test sample on the measurement table and set up the focus point of the laser on the edge of the length side at half-width. Then a measurement of the maximum displacement at a frequency range of 100 – 500 kHz was taken at every 1 mm staying at half-width until a non-reflective surface was reached (Figure 16). Afterwards the test sample was turned around as careful as possible and the experiment was repeated with the same amount of steps as illustrated in Figure 15. The result was a one dimensional grid of mechanical displacement over a frequency sweep on the PZT silver electrode and opposite aluminum surface with the glue in between which was used to characterize the glue damping. Additionally, at the first point on both sides a videos of a small grid (5x7 measurement points corresponding to an area of around 400x600  $\mu\text{m}$ ) of the strongest resonance modes were created.

The PZT was powered by a 10 V chirp signal without a reference signal. The chosen optics was VD-02 (25mm/s/V) with a 10x objective and the measurement points were complex mean values over 50 measurements. The vibrometer has an internal low pass with a cut-off frequency of around 1.5 MHz therefore it was not possible to measure the best resonances of our PZTs and the different frequency range was chosen which was sometimes used to clean the cell.

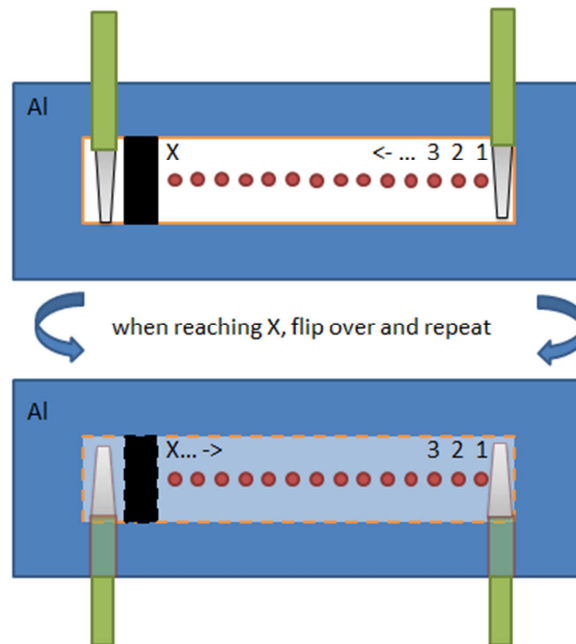
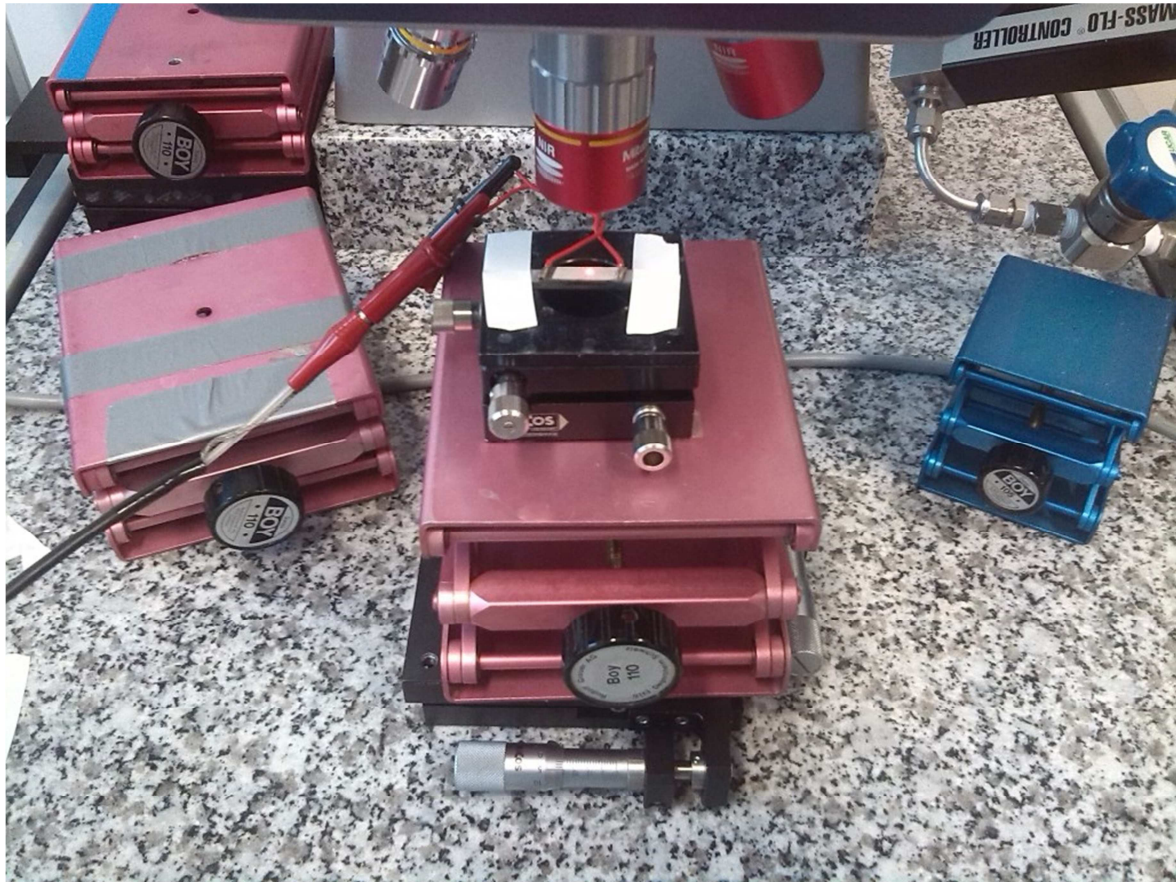


Figure 15: Measurement method of vibrometer experiment with a PZT glued to an aluminum base.



**Figure 16: Picture of the vibrometer experimental set-up. The micrometer screw at the bottom of the picture was used to move the focus point 1 mm per step.**

## **2.7. ICP-OES experiments**

The inductively coupled plasma - optical emission spectrometry (ICP-OES) experiments were done to quantify the actual retention of the cell as a proof of concept. The used ICP-OES is a Thermo Scientific iCAP6500 RAD of the iCAP 6000 series and the connected PC runs the software iTEVA Control Center version 2.8.0.96. 1% HNO<sub>3</sub> was used for the blank feed. The radio frequency power for the plasma was 1500 W, the peristaltic pump was set to 25 rpm which resulted in a volume flow of approx. 1 mL/min with the used tubing. The gas configurations were a nebulizer gas flow of 0.5 L/min, an auxiliary gas flow of 1 L/min and a coolant flow of 12 L/min. The particle concentration varied for the suspension feed with around 0.005g MCM-41 per 10mL 1% HNO<sub>3</sub>. It was always mixed high enough to have a base-line of at least a 3000 count/s signal for the silicon 251.6 nm characteristic line. The particle suspension was always kept in an ultrasonic bath to avoid settling effects and agglomeration. The measurements were done in the transient signal mode which cumulates the emission signal over time steps of 3 seconds. The displayed graphs are all background corrected by subtracting the detector offset signal. For better visualization of the acoustic filtering the data is presented as a first deviation of the cumulated signal to display plateaus instead of changes in the slope of the original reading. The set-up for the experiments is sketched in Figure 17 and a photograph is shown in Figure 18.

We developed the following different measurement methods:

- 0) Blank – for every new measurement series the first few readings are of a blank feed to guarantee a stable signal and to know the offset at the detector.
- 1) Filling the cell – then a reading was taken of how much time is necessary from changing the feed to a particle suspension to a stable ICP-OES signal.
- 2) 0.5 – 2 – 2.5 measurement – it is our standard retention measurement where the numbers stand for minutes: 0.5 minutes without acoustic field – 2 minutes acoustic field activated – 2.5 minutes watching the flush out process
- 3) 5 – 9 – 1 measurement – it is our advanced retention measurement where the first 5 minutes a particle suspension is captured in the acoustic field without taking readings due to inability in the software to stop the pump during measurement. Then changing to a blank feed and starting the data acquisition and watch 9 minutes of replacing the cell volume of particle suspension with a blank while the acoustic field is still active and holding particles, and once the 9 minutes are over the acoustic field gets deactivated and for 1 minute the flush out of the captured particles is observed.

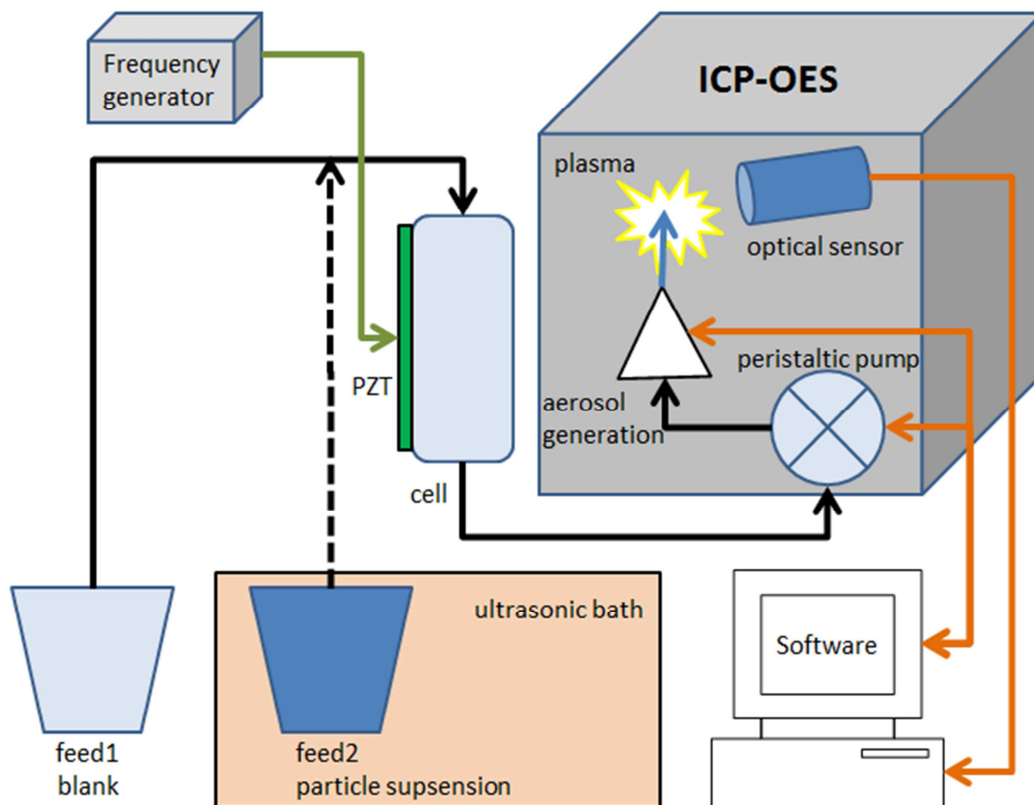


Figure 17: Schematic of ICP-OES experiment set-up



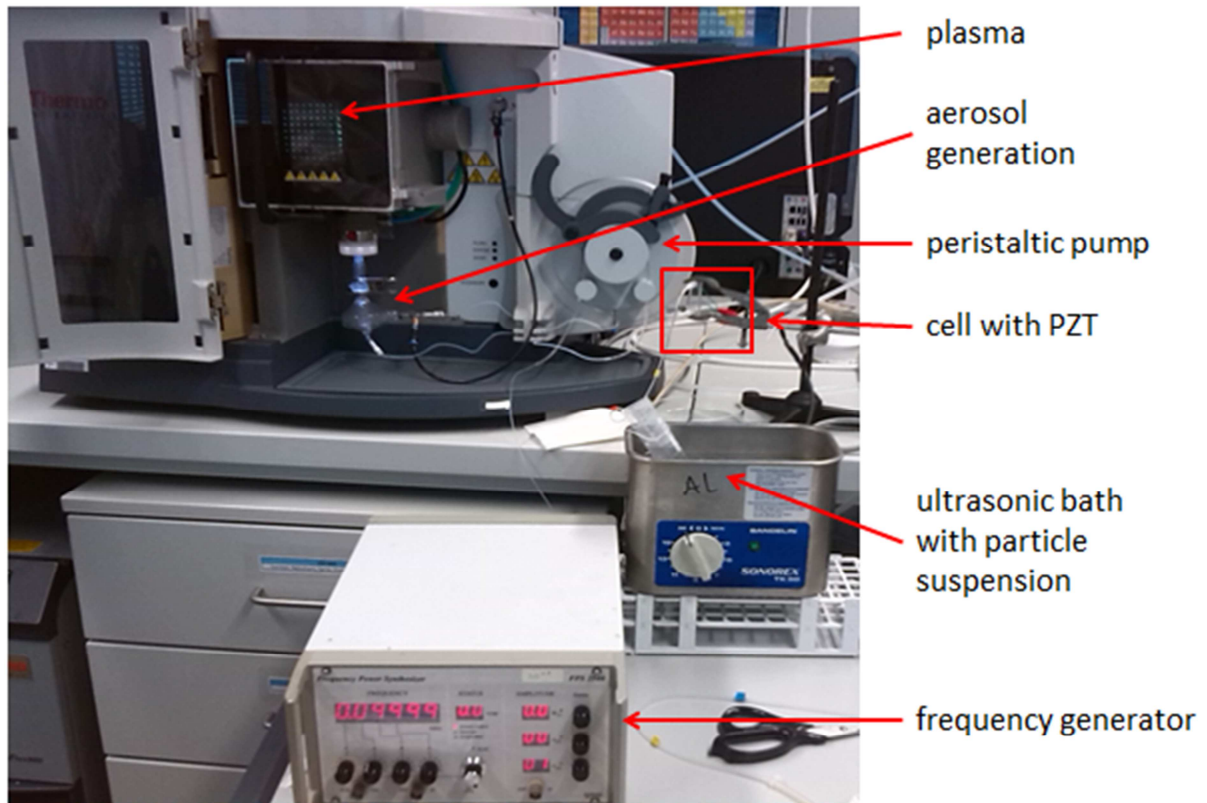
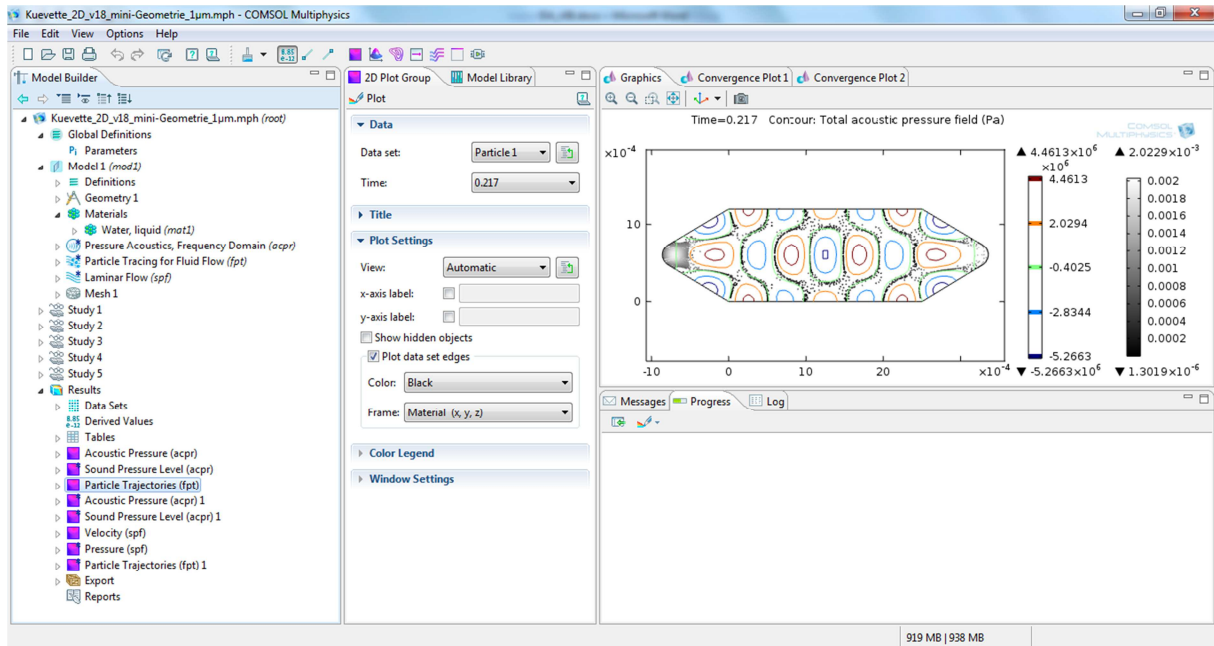


Figure 18: Picture of the ICP-OES experimental set-up.

## 2.8. COMSOL Simulations

Simulations were mainly done in a simplified 2D model to reduce the required processing power and if particles were included it was often necessary to scale down the geometry (1:10) for reasonable processing times and visibility.

An example of the user interface of the model for cell1 in two dimensions (Figure 19) will now be used for a general overview of the COMSOL Multiphysics 4.3a version.



**Figure 19: COMSOL User Interface screenshot**

The left window is the Model Builder in which all the navigation through the simulation process takes place, the middle window changes depending on the selection in the model builder and on the right the current graphic is displayed with information messages below.

The first point in the model builder is “Global definitions” which includes the parameters for the model. Using variables for all inputs in the geometry and boundary conditions has the great advantage of having them in a single place and being able to adjust them at any point in the future while doing so automatically updates the model. For this model the parameters seen in Table 3 were defined.

Name	Expression	Description
f0	2 [MHz]	Driving frequency
c0	1482 [m/s]	Speed of sound
lambda0	c0/f0	Wavelength
d_p	1 [μm]	Particle diameter
rho_p	1300[kg/m^3]	Particle density
a0	1.5e6[m/s^2]	Normal acceleration of transducer
W	25 [mm] / scale_factor	Width rectangle
H	12 [mm] /scale_factor	Height rectangle
D	10 [mm] /scale_factor	Distance triangle
R	3 [mm] /scale_factor	Radius inlet/outlet
u0	1e-3[m/s]	Flow Speed
K	2.2E9 [Pa]	Particle Bulk Modulus
epsilon	1 [eV]	Particle Interaction Force
potenz	3	Lenard-Jones Potential power
scale_factor	10	Geometry scale down factor

**Table 3: Parameters of cell1 2D model.**

The second point is the model itself which includes the physics modules selected, the built or imported geometry and the materials used. In my simulations all geometries were built in COMSOL and in 2D; only the water volume gets simulated and is therefore the only material used. Additionally it should be noted that if one wants to do acoustic particle manipulation, the predefined meshes of COMSOL are not sufficient and it is necessary to use a user defined mesh. In my simulations a triangular mesh with a maximum element size of  $\lambda/100$  was used.

The following points are the studies in which one has to define what should be calculated by choosing the physics modules and solver. In my simulations only preset studies were used. It is possible to connect the studies by defining the results of one study as input for the next study. In the above model, first a stationary study was calculated for the fluid dynamics, which was the input for the frequency domain study of the acoustic field. And last a time dependent study was calculated on top of the previous two for particle trajectories.

### 2.8.1. Fluid dynamics

The fluid dynamics were calculated for both cells in two dimensional space.

#### 2.8.1.1. Cell1

Cell1 is built with a rectangle of width W and height H in the middle and two triangles with the third corner at distance D of the rectangle on the left and right of it as seen in Figure 20. The corners are then filleted with radius R/2 and the inlet and outlet are modeled with points on a similar triangle at a radius of R from the original corner. In the end it is all combined together into a union.

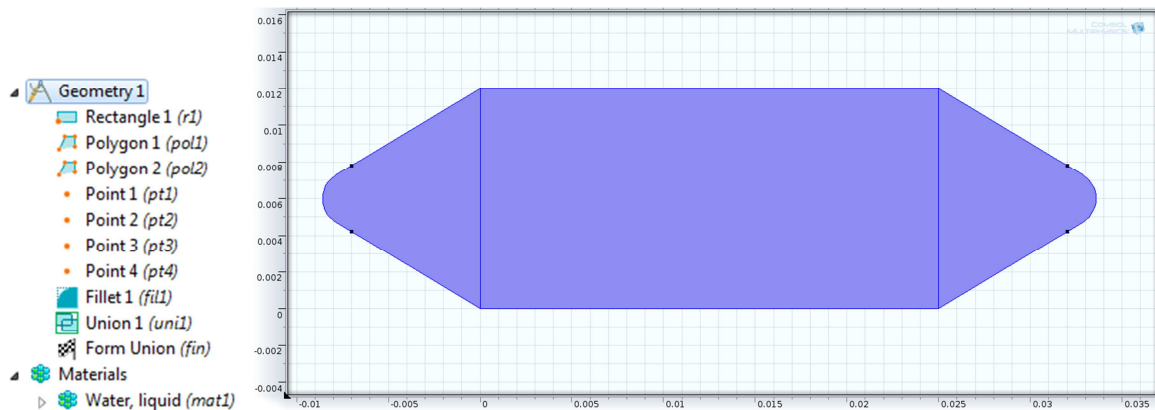


**Figure 20: Cell1 COMSOL geometry; on the left every single part and material and on the right the resulting geometry.**

The used parameters:

Name	Expression	Description
W	25 [mm] / scale_factor	Width rectangle
H	12 [mm] /scale_factor	Height rectangle
D	10 [mm] /scale_factor	Distance triangle
R	3 [mm] /scale_factor	Radius inlet/outlet
scale_factor	1	Geometry scale down factor
u0	1e-3[m/s]	Flow Speed

**Table 4: Geometry parameters of cell1 2D model.**

The cell is modeled with fluid properties, density  $\rho$  and dynamic viscosity  $\mu$  from the material. A wall with no slip (velocity  $u=0$ ) boundary condition on all edges of the geometry except on the tips between the points on the left and right as illustrated by the blue lines in Figure 21. The inlet is on the left side with a normal inlet velocity of  $u_0$ , the outlet is on the right side with a boundary condition of pressure  $p=0$ .

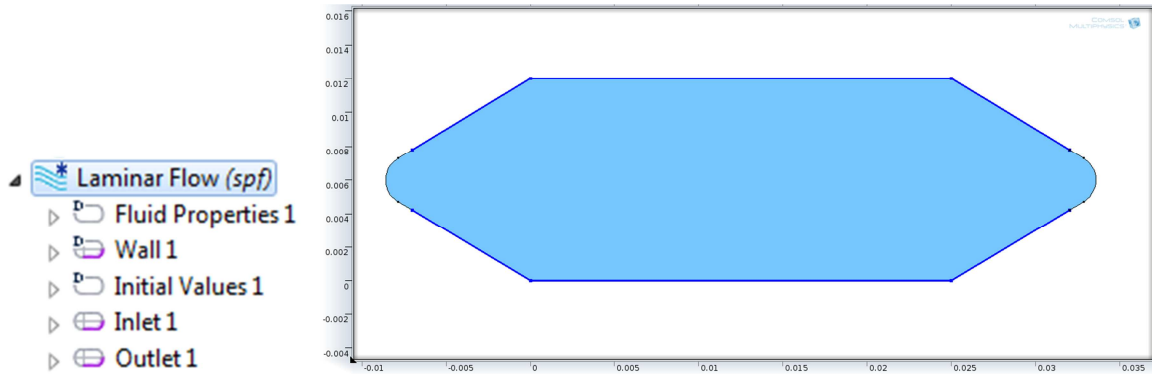


Figure 21: Cell1 fluid dynamic boundary conditions; on the left the model builder elements and on the right the visual presentation of the boundaries are shown.

### 2.8.1.2. Cell2

Cell2 is built with a rectangle of width  $W$  and height  $H$  as a basis. Then the top left and bottom right corners are cut out with triangles to create one defined water area, shown as red in Figure 22. As a next step the two triangles are created again as defined PDMS area. Then all corners are filleted and the inlet/outlet and PZT coupling edges are defined with points.

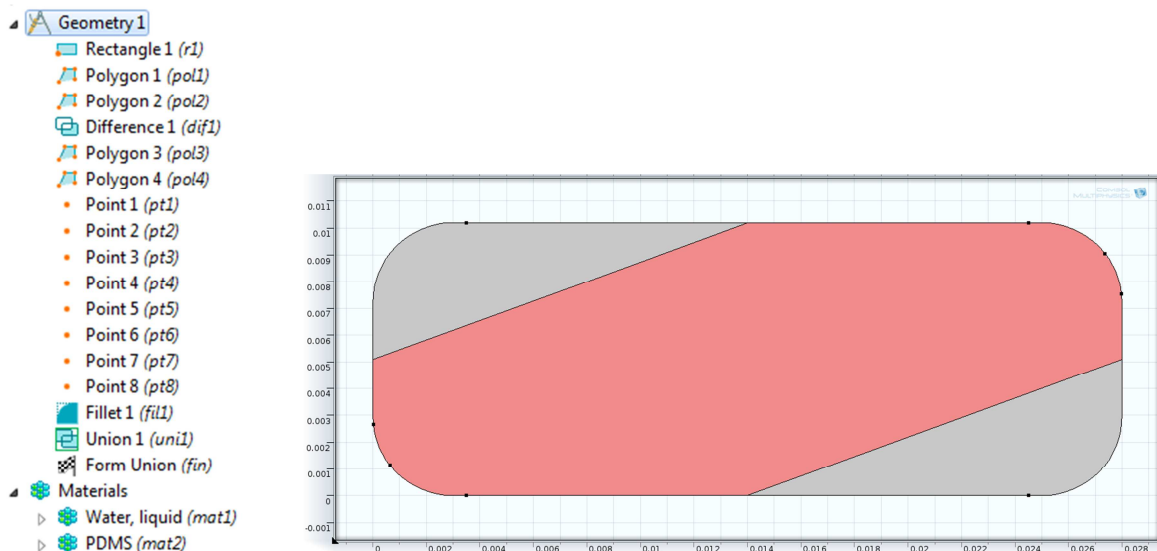
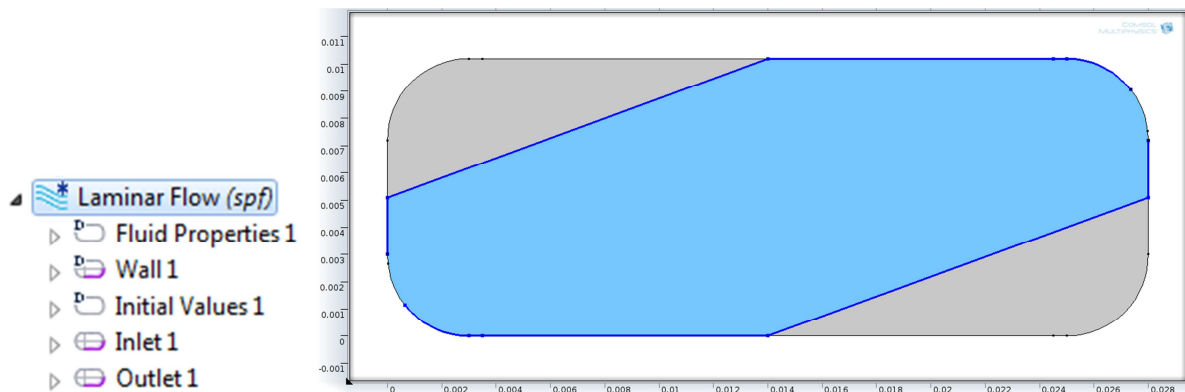


Figure 22: Cell2 COMSOL geometry; on the left every single part and material and on the right the resulting geometry is illustrated.

Name	Expression	Description
W	28 [mm]	Width rectangle
H	10.2 [mm]	Height rectangle
D	1.5 [mm]	Drill diameter
R	3 [mm]	Fillet radius
wall	3.2 [mm]	Drill middle to opposite wall
hole_mid	11.5 [mm]	Complete height
y1	$H+wall-hole\_mid+D/2$	Point 1 y coordinate
y2	$H+wall-hole\_mid-D/2$	Point 2 y coordinate
y3	$hole\_mid-wall+D/2$	Point 3 y coordinate
y4	$hole\_mid-wall-D/2$	Point 4 y coordinate
x1	$R-\sqrt{R^2-(R-y1)^2}$	Point 1 x coordinate
x2	$R-\sqrt{R^2-(R-y2)^2}$	Point 2 x coordinate
x3	$W-R+\sqrt{R^2-(y3-H+R)^2}$	Point 3 x coordinate
x4	$W-R+\sqrt{R^2-(y4-H+R)^2}$	Point 4 x coordinate
u0	1e-3[m/s]	Flow Speed

**Table 5: Geometry parameters of cell2 2D model.**

The cell is modeled with fluid properties, density  $\rho$  and dynamic viscosity  $\mu$  from the material. A wall with no slip (velocity  $u=0$ ) boundary condition on all edges of the water area except on the drill points left bottom and top right as shown by the blue lines in Figure 23. The inlet is on the left side with a normal inlet velocity of  $u_0$ , the outlet is on the right side with a boundary condition of pressure  $p=0$ .



**Figure 23: Cell2 fluid dynamic boundary conditions; on the left the model builder elements and on the right the visual presentation of the boundaries.**

## 2.8.2. Acoustic Field

The acoustic field was calculated for cell1 in a three dimensional model and for both cells in two dimensional geometries.

### 2.8.2.1. 3D cell1

Cell1 is built with a block of width  $W$ , height  $H$  and depth  $T$  as a basis. Then the inner water volume was built with a hexahedron which was copied and mirrored to the downside and combined to a union of water volume. The 3D Model is illustrated in Figure 24.

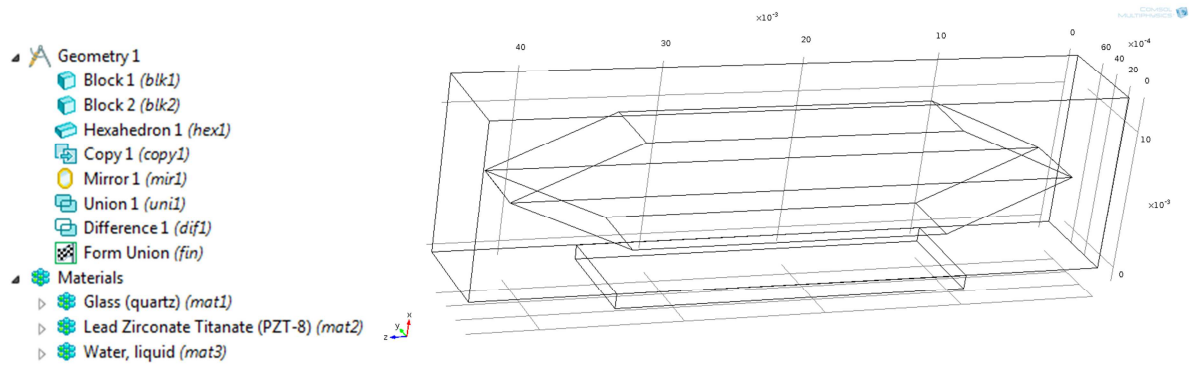


**Figure 24: Cell1 3D COMSOL geometry; on the left every single part and material and on the right the resulting geometry.**

Name	Expression	Description
H	45 [mm]	Cell height
B	12.5 [mm]	Cell width
T	7.5 [mm]	Cell depth
pzt_T	1 [mm]	PZT depth
pzt_H	25 [mm]	PZT height
pzt_B	T	PZT width
wall	1.25 [mm]	Wall thickness
glass_speed	3962 [m/s]	Speed of sound in glass
a	1.5e6[m/s^2]	Normal acceleration of transducer

**Table 6: Geometry parameters of cell1 3D model.**

The cell is modeled with a stress charge form of piezoelectric material, where the matrices were input from the PIC181 datasheet of Pi ceramics. Since it was only calculated using Eigen frequencies, the only boundary condition for the PZT is a fixed constraint to the glass volume as seen in Figure 25. The pressure acoustic model is a linear elastic one with the speed of sound  $c$  and density  $\rho$  from the material. The outer boundary of the glass is a hard wall and the PZT is coupled into the volume with a normal inward acceleration  $a$  at the same surface as the fixed constraint.

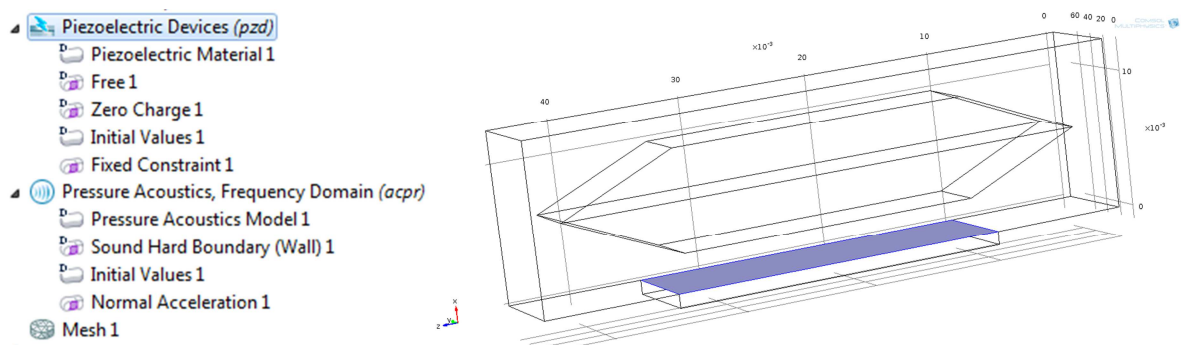


**Figure 25: Cell1 3D boundary conditions; on the left the model builder elements and on the right the visual presentation of the boundaries.**

### 2.8.2.2. 2D cell1

For a description of the geometry, see fluid dynamics part (2.8.1.1).

The pressure acoustic model is a linear elastic one with the speed of sound  $c$  and density  $\rho$  from the material. The outer boundary as seen in Figure 26 is a hard wall and the PZT is coupled into the volume with a normal inward acceleration  $a$  at the lower edge. Here the option with only one active PZT at the bottom is shown, it was also possible to use the top edge for simulating a second PZT powered parallel to the first.

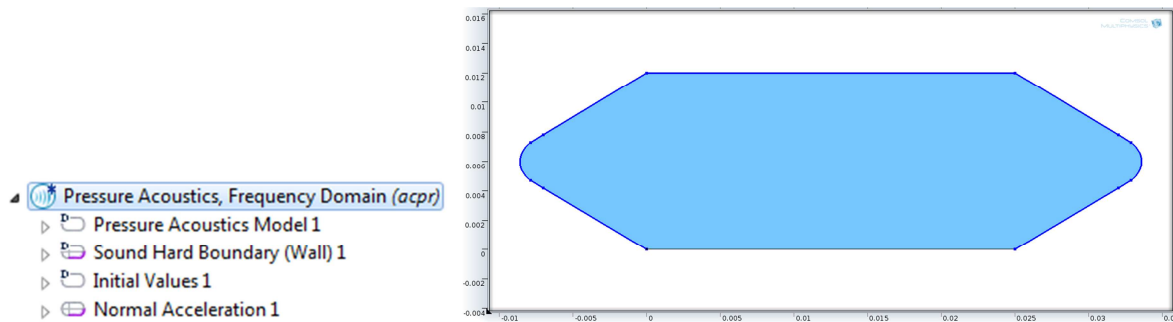


Figure 26: Cell1 2D boundary conditions; on the left the model builder elements and on the right the visual presentation of the boundaries.

### 2.8.2.3. 2D cell2

For a description of the geometry, see fluid dynamics part (2.8.1.2).

The pressure acoustic model is a linear elastic one with the speed of sound  $c$  and density  $\rho$  from the material. The outer boundary as seen in Figure 27 is a hard wall and the PZT is coupled into the volume with a normal inward acceleration  $a$  at the lower edge. Here the option with only one active PZT at the bottom is shown, it was also possible to use the top edge for simulating a second PZT powered parallel to the first.

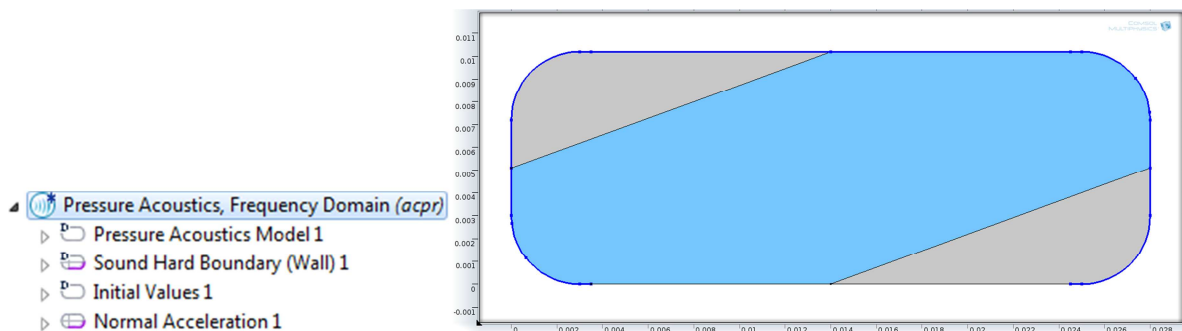


Figure 27: Cell2 2D boundary conditions; on the left the model builder elements and on the right the visual presentation of the boundaries.

## 2.8.3. Particle Manipulation

For particle manipulation the velocity field was solved in a stationary study and the result linked to the acoustic field frequency domain study over the “values of dependent variables – initial values of variables solved for/values of variables not solved for” fields. The same link was used to a time dependent study for the particle module and the forces need to be linked to the field variables

(density, velocity, dynamic viscosity  $\mu$ , pressure  $p$ ) as seen in Figure 28.

The boundary geometry is the same as in the fluid dynamic cases for the wall and inlet/outlet. The boundary condition for the wall and outlet was “freeze” so that a particle which reaches them is frozen in place with the velocity and direction information at the time of collision. For most studies a “release” was used for filling the whole volume with particles with an initial position based on the mesh. Otherwise the inlet was used with an initial position of uniform distribution and time dependent inflow of particles.

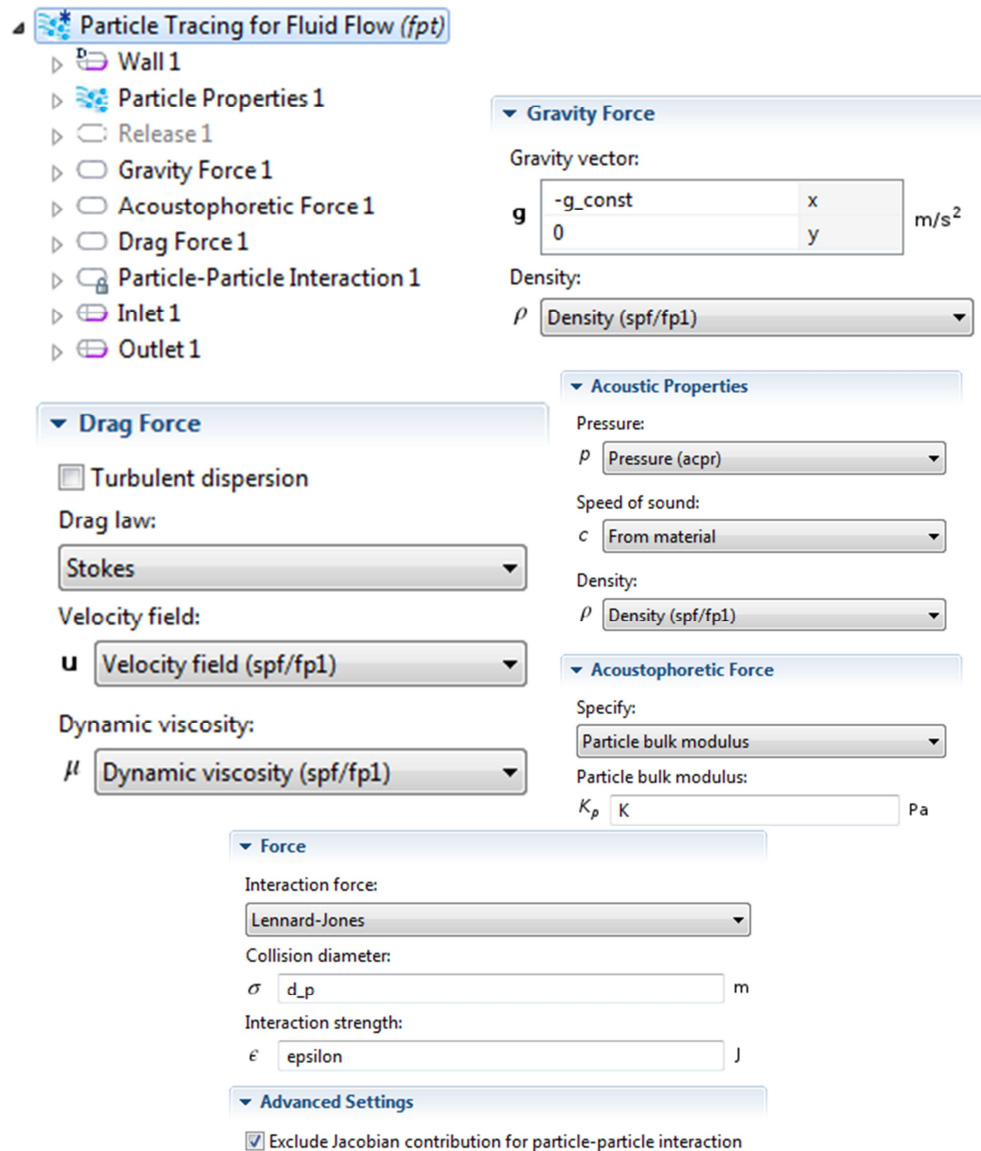


Figure 28: Particle manipulation forces configuration.

Name	Expression	Description
d_p	1 [ $\mu\text{m}$ ]	Particle diameter
rho_p	1300 [ $\text{kg}/\text{m}^3$ ]	Particle density
K	2.2E9 [Pa]	Particle Bulk Modulus
epsilon	1 [eV]	Particle Interaction Force
potenz	3	Lenard-Jones potential power

Table 7: Particle manipulation parameters.



The particle – particle interaction was later added to simulate agglomeration of the particles.

It is based on a Lenard Jones Potential but was edited from the standard COMSOL equation, because of limitations in mesh accuracy in addition to very small particle size it happened that agglomerates exploded in the simulation. Therefore the potential was altered to a less steep curve for more tolerance to inaccuracies in the calculation.

The interaction strength of the particle-particle interaction is based on London & van der Waals force with the Hamaker constant [12], based on which an interaction strength  $\epsilon=1\text{eV}$  was chosen.

The particle diameter for most simulations was chosen as  $\sigma=1\mu\text{m}$ .

Figure 29 shows a comparison of the COMSOL Potential V6 to the used V3 potential.

$$V_3 = 4\epsilon\left[\left(\frac{\sigma}{r}\right)^9 - \left(\frac{\sigma}{r}\right)^3\right] \quad \text{Equation 26}$$

$$V_6 = 4\epsilon\left[\left(\frac{\sigma}{r}\right)^{12} - \left(\frac{\sigma}{r}\right)^6\right] \quad \text{Equation 27}$$

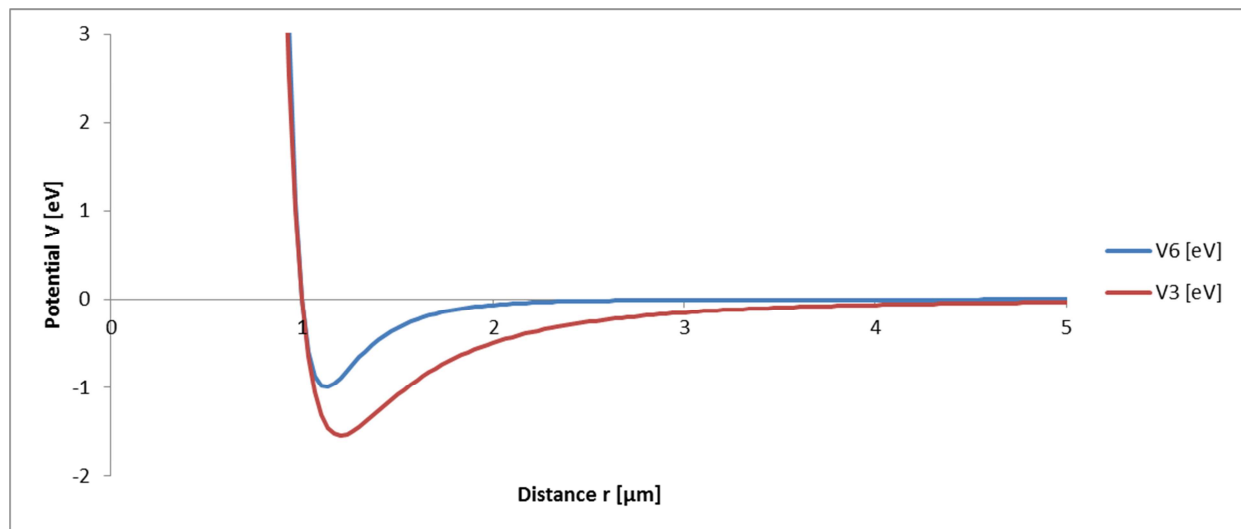


**Figure 29: Lenard Jones potentials with different exponents.**

The increase in attraction strength by a factor of 1.5 at the deepest point in Figure 29 is acceptable considering the inaccuracy in the Hamaker constant. The increase in attraction distance from two times the particle diameter to four times the particle diameter is also acceptable due to the stronger acoustic force in the simulation volume and the steep decrease in attraction strength for these distances. All in all the weaker Lenard Jones potential is only a mathematical model trying to approximate reality accurately enough which is viable for this simulation.

## 3. Results and discussion

### 3.1. Admittance measurements

#### 3.1.1. Choosing the PZTs

There were 10 Pi Ceramics PIC181 25x25x1mm PZTs available from previous projects. To choose which PZT to use we measured the spectra of the lower Resonance Peak at 2 MHz because at that time a frequency generator to power the 6 MHz resonance was not available. The spectra are shown in Figure 30.

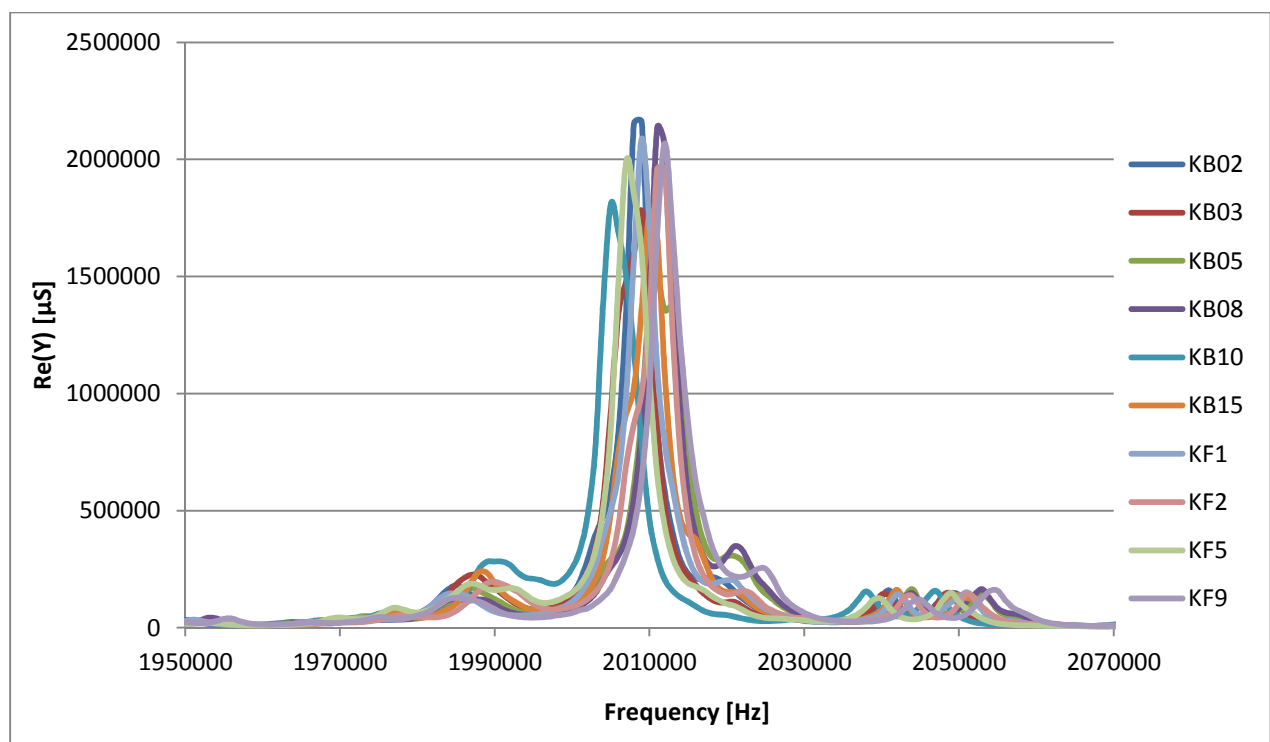


**Figure 30: Conductance spectrum of all available PZTs.**

A ranking of the PZT pieces was established by calculating the sum of the conductance between 2.00 and 2.03 MHz to determine which one could deliver the best performance as seen in Figure 31.

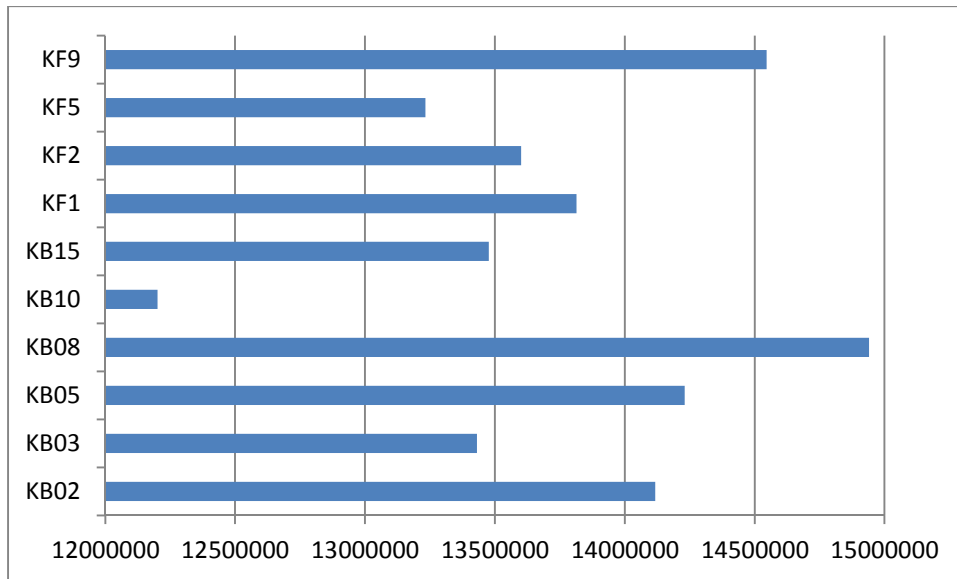


**Figure 31: Performance ranking of PZTs.**

We decided to use KB03 and KB05 from the middle field first for testing and experimenting and saved the best for later. In the end KB08 was used for Cell2.

### 3.1.2. Preparing the PZTs

After breaking the PZTs into pieces by scratching the electrode with a glass cutter and breaking over an edge, they got new names as seen in Table 8 and we measured how their spectra changed.

New Name	Old Name
P1	KB05
P2	KB05
P3	KB03
P4	KB03
P5	KF1
P6	KF1
P7	KF2
P8	KF2
P9	KB15
P10	KB15
P11	KB08
P12	KB08

**Table 8: Naming convention of PZTs.**

To show how drastically different results breaking can have Figure 32 includes the spectra of the first 5 pieces.

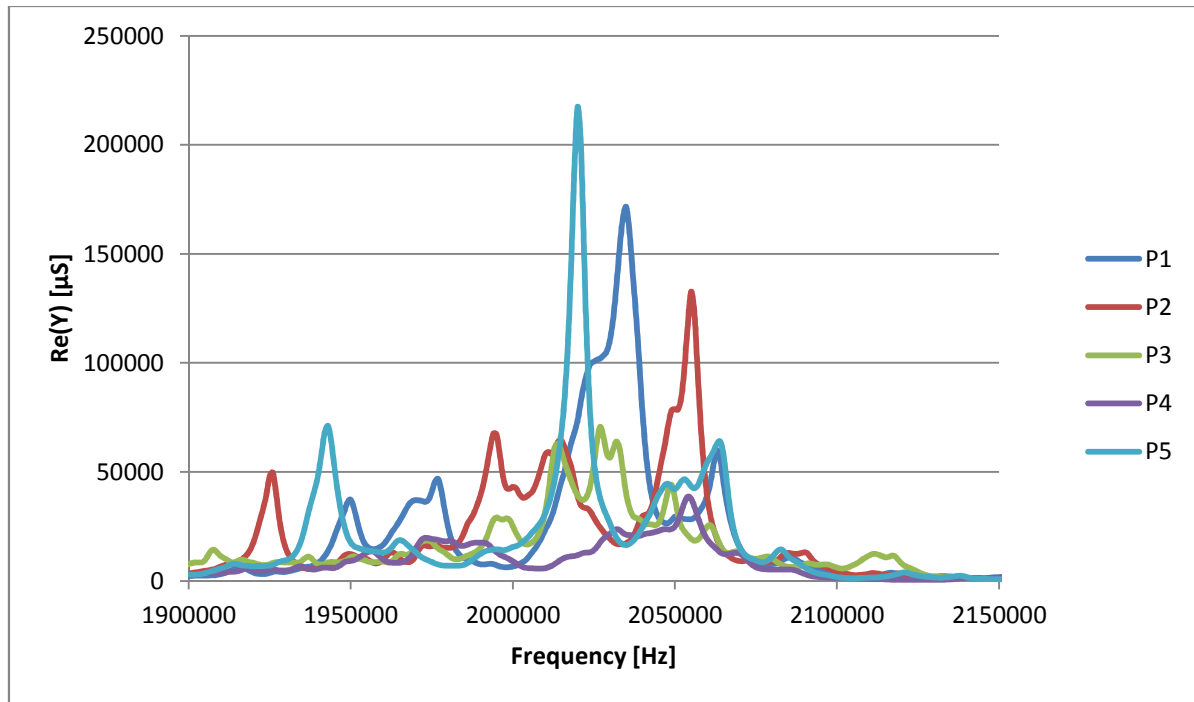


**Figure 32: Spectrum changes depending on how nicely the PZT broke.**

For the most experiments P1 was glued to cell1 so for a detailed look the focus will from now on be on P1. At the first try to build cell1 P1 was first glued on it with super glue and then wires were soldered on it, with the result that the heat from soldering weakened the bonding. Consequently the spectrum from a water filled cell did not show any additional water peaks (Figure 36). Due to that we disassembled it using acetone to dissolve the super glue and changed the working steps to first soldering then gluing.

In Figure 33 the whole spectrum for KB05, raw P1 and soldered P1 is illustrated. Figure 34 shows the 1.8 – 2.4 MHz frequency range and Figure 35 the 6.4-7 MHz frequency range with the additional spectra of the whole assembly filled with air and water.

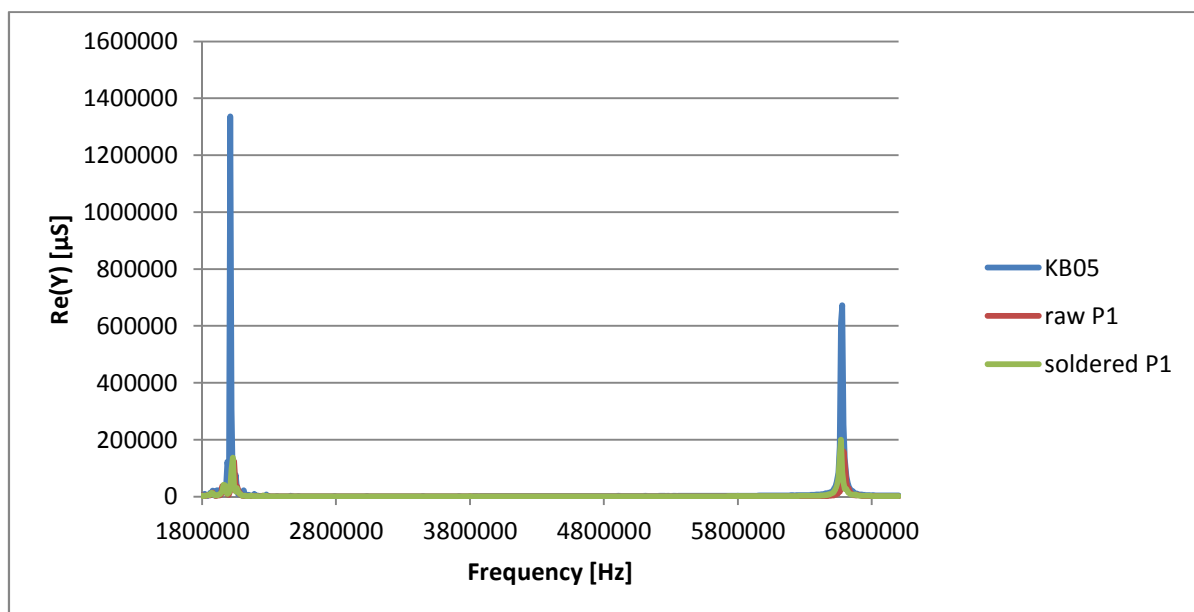


**Figure 33: Spectrum changes during P1 preparation, whole spectrum.**

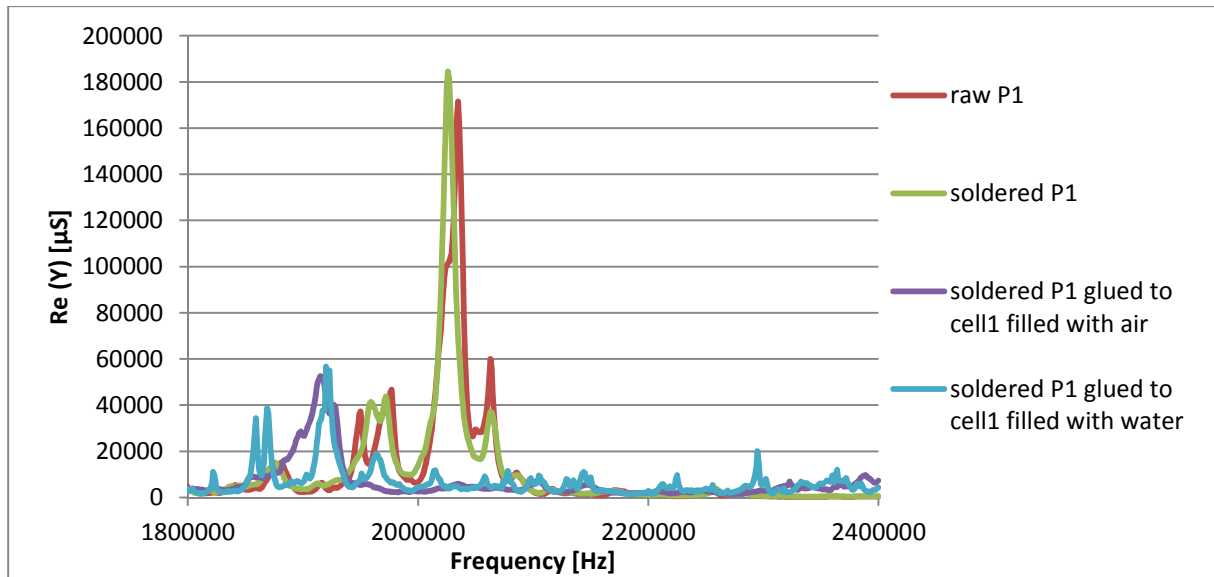


**Figure 34: Spectrum changes during P1 preparation, lower resonances.**

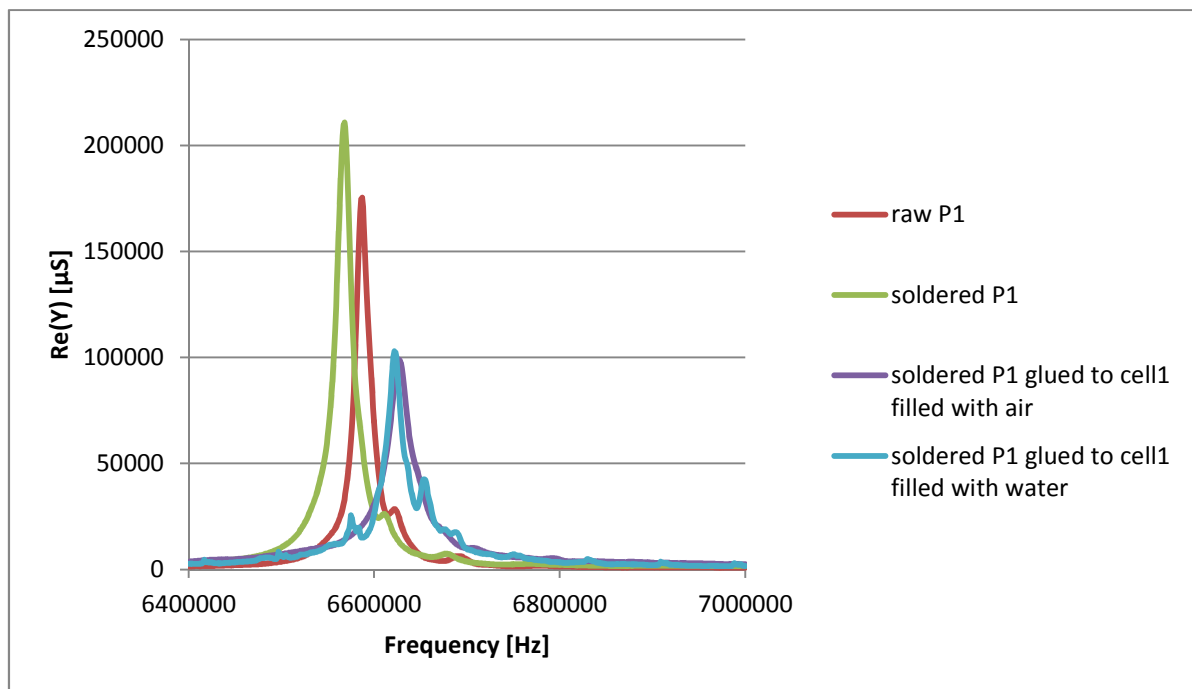


**Figure 35: Spectrum changes during P1 preparation, higher resonances.**

For comparison Figure 36 shows the first gluing with a weak coupling of the PZT into the water volume and Figure 37 shows the second gluing with easily visible water resonances additional to the ceramic peak which indicates a better coupling.

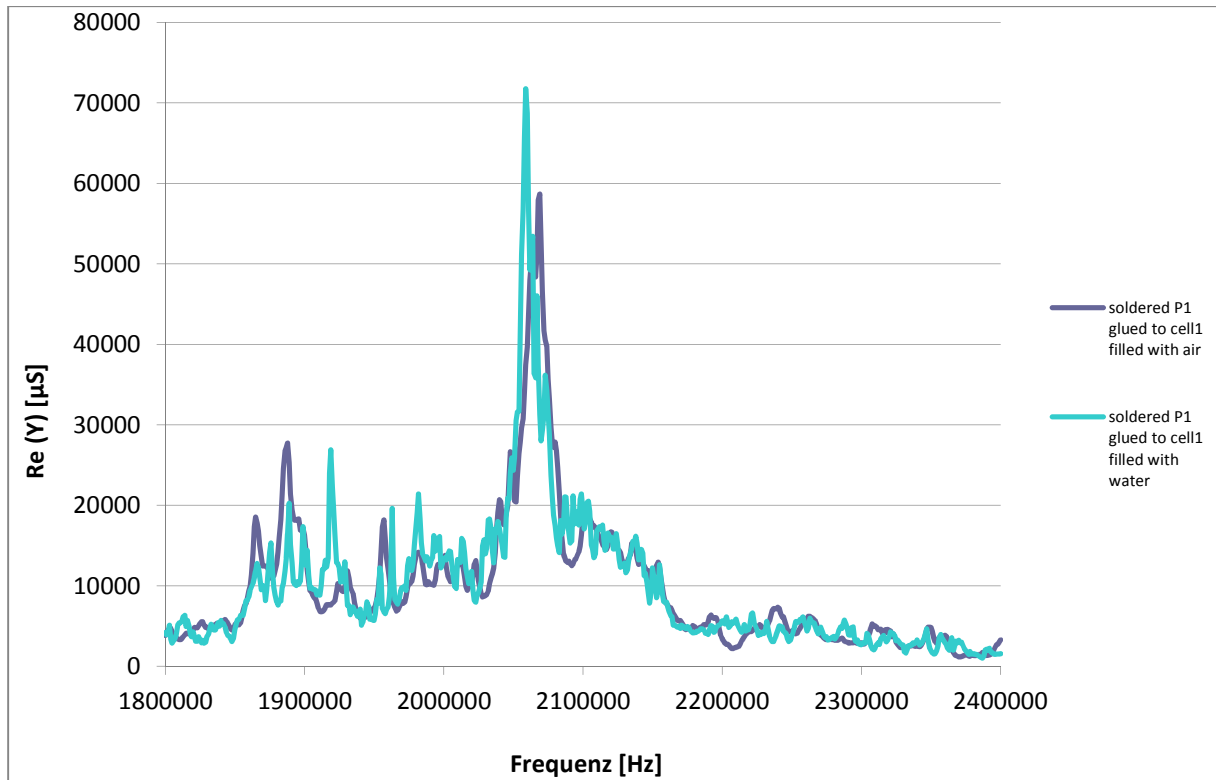


Figure 36: Spectrum changes during P1 preparation, first gluing.

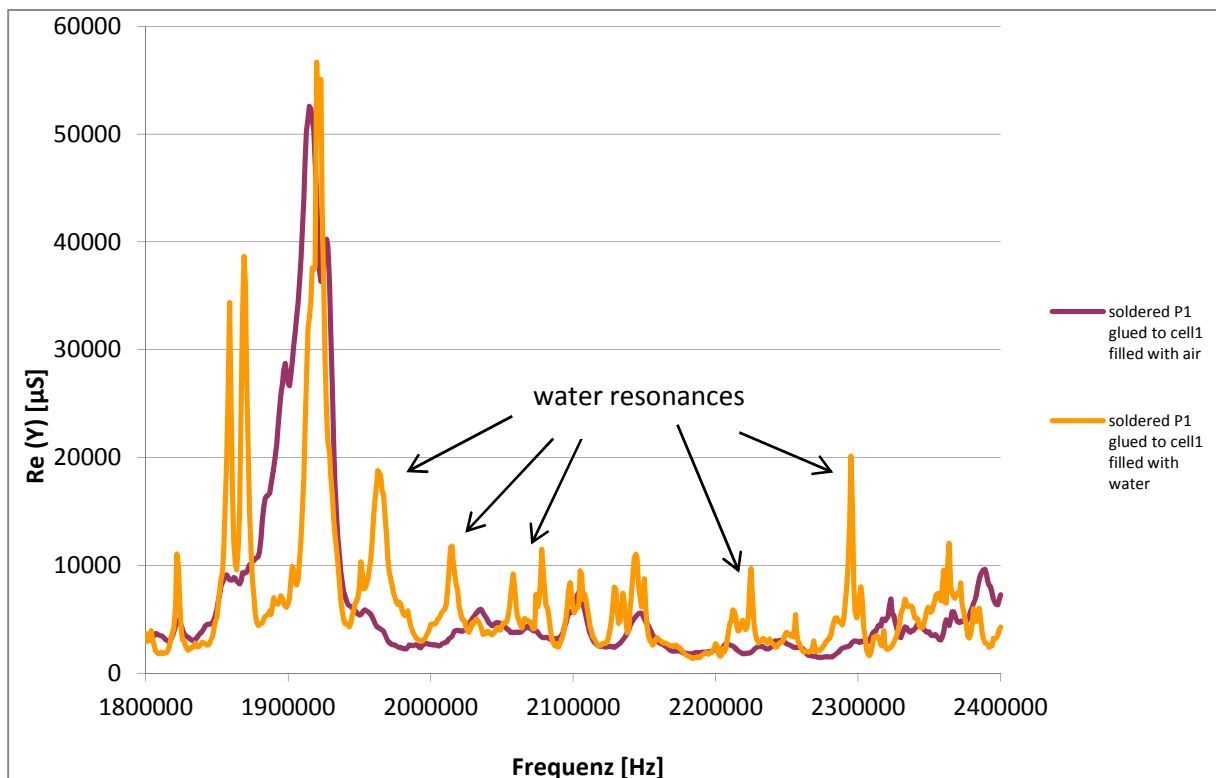
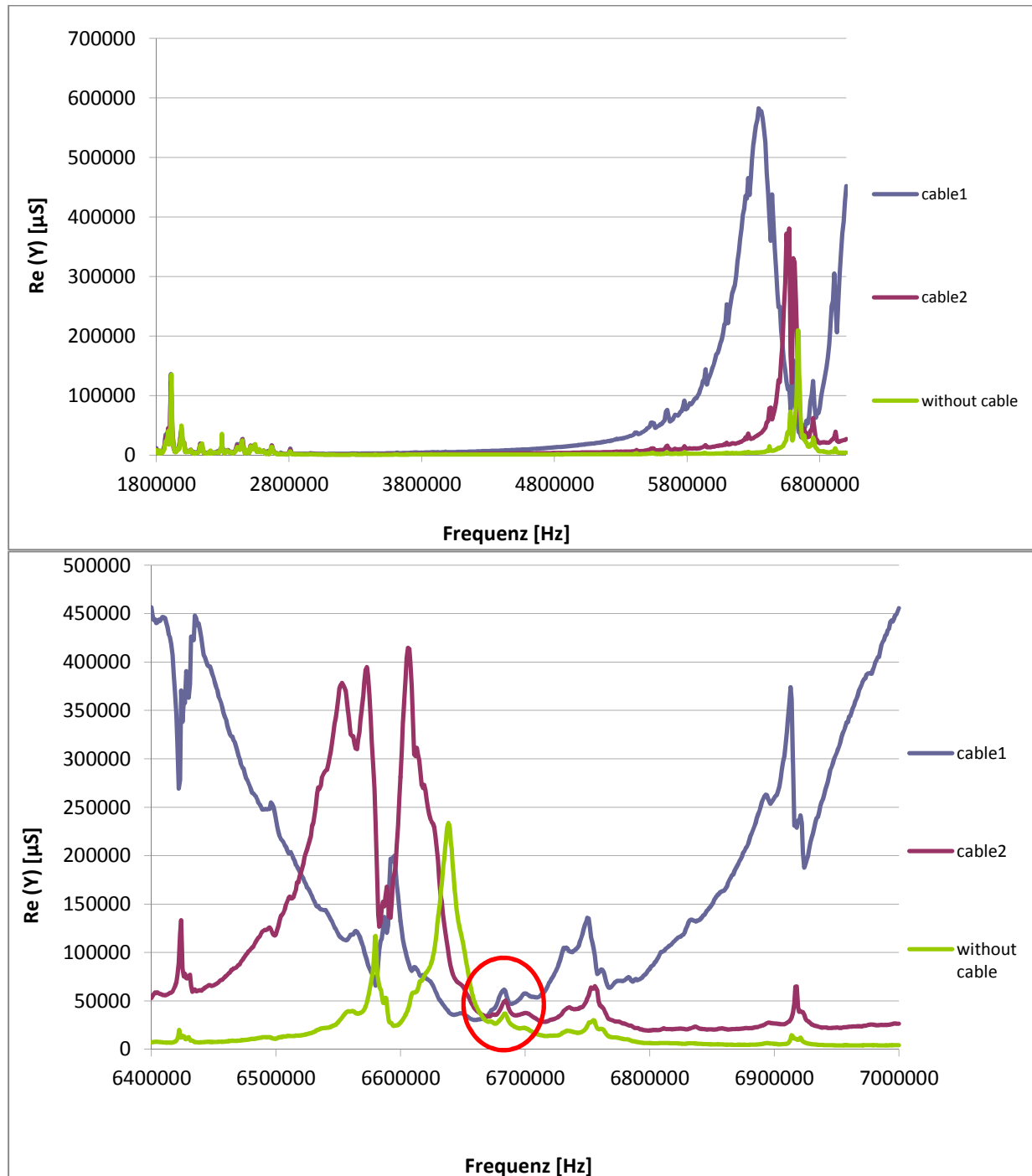


Figure 37: Spectrum changes during P1 preparation, second gluing.

After the delivery of the new frequency generator, it was discovered that powering the 6 MHz resonances wasn't trivial. So due to troubles of powering the higher resonance at 6 MHz a shorter cable was needed due its low-pass characteristic.

Our first cable is approximately 1 m long and by halving the length to 0.5 m we expected to sufficiently increase the cut off frequency of the low pass characteristic of the RG58 coaxial cable with approximately 100 pF/m.

The measurements of the PZT spectrum in Figure 38 showed that it was indeed an improvement.



**Figure 38: Spectrum of cable comparison.**

From the admittance spectra it was concluded that cable2 was sufficient and it was experimentally possible to power a 6 MHz frequency which was not possible with cable1.

When trying to sweep over more frequencies we noticed we were only able to drive the little peak at 6.666 MHz (highlighted by the red circle in Figure 38) with cable2, which correlates with the single peak in the impedance spectrum at exactly that frequency. This could indicate that at the higher resonances a sufficient impedance match is necessary to power a frequency.

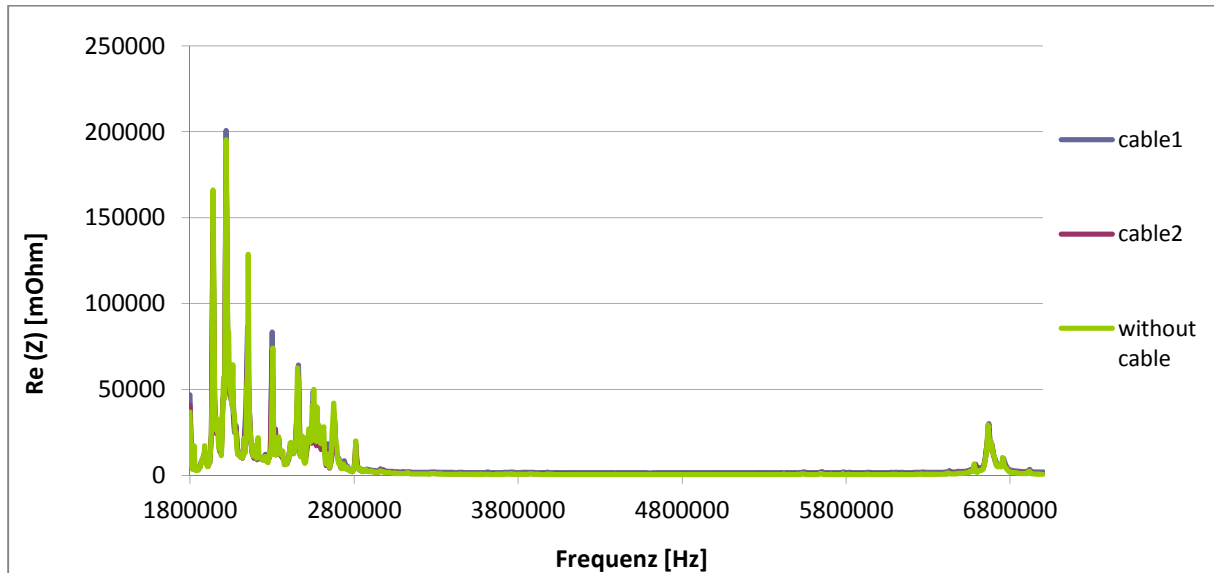


**Figure 39: Impedance spectrum for cable comparison.**

The vibrometer PZT samples were measured in a different frequency range because the vibrometer has a low pass filter with a cutoff frequency of 1.5 MHz. Therefore it was decided to take a closer look at the 100-500 kHz area which we use to clean our cells.

Figure 40 and Figure 41 illustrate the comparison of the PZTs before gluing (while already soldered) and after the gluing. Luckily enough the finalized spectra of the two are very similar which makes them easier comparable at the vibrometer.



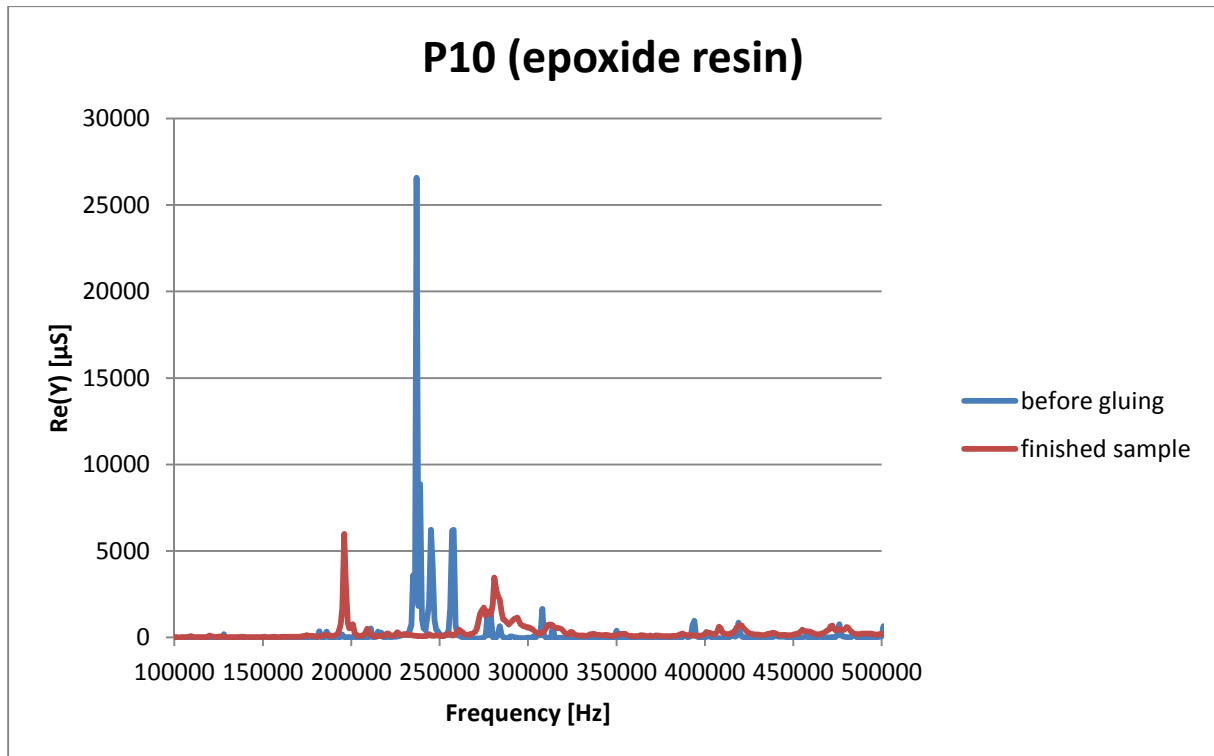


Figure 40: Spectrum of P10 comparison.

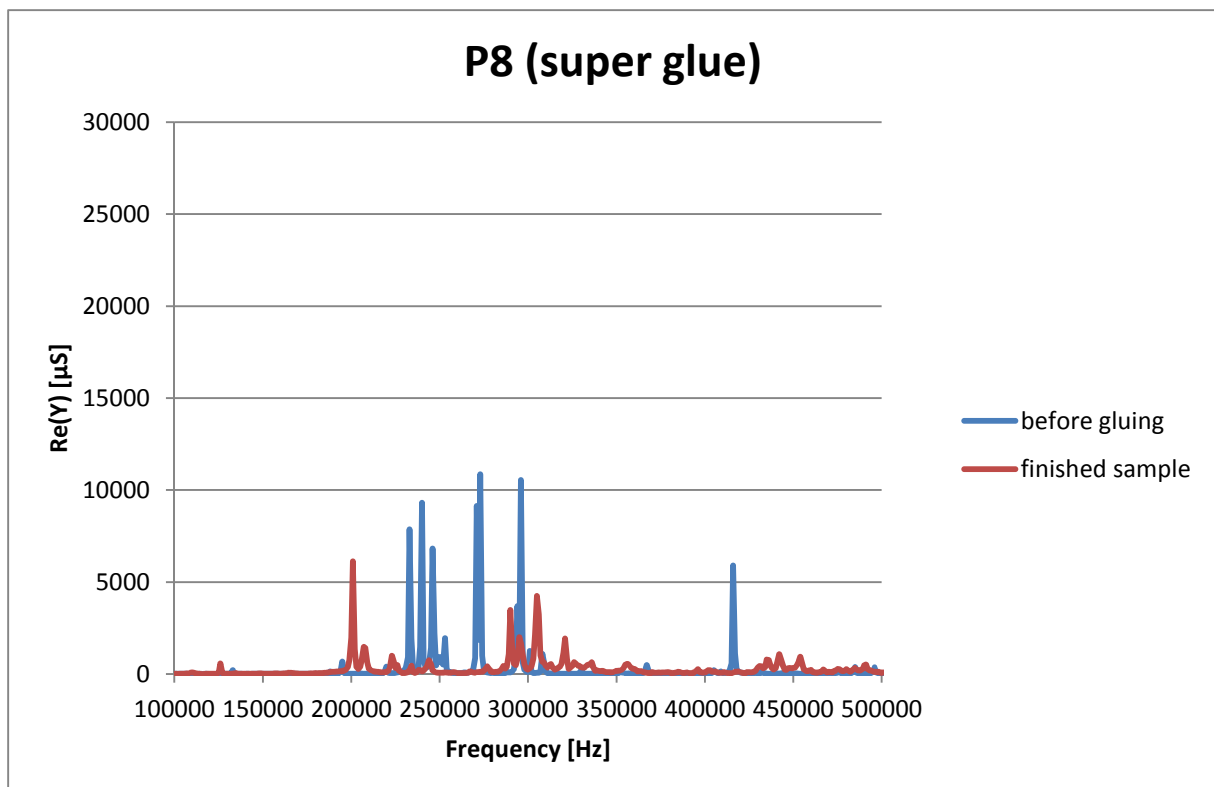


Figure 41: Spectrum of P9 comparison.

### 3.2. Vibrometer measurements

Two samples were measured as explained in the method description. They were two aluminum bases and on them glued with two different glues the above described PZTs P8 (super glue-Loctite Superkleber PowerGel) and P10 (epoxide resin-Duralco 4700 HT).

The data was written in text files and visualized with python scripts using the matplotlib library.

Waterfall graphs were created to display the amplitude spread over the length of the PZT and the frequency spectrum for all 4 surfaces and additionally it was tried to summarize it in a 2D color chart with the previously measured admittance spectrum edited in on the right side. (Figure 44 and Figure 47)

First, the measurements of the epoxide resin sample are presented as waterfalls in Figure 42 and Figure 43.

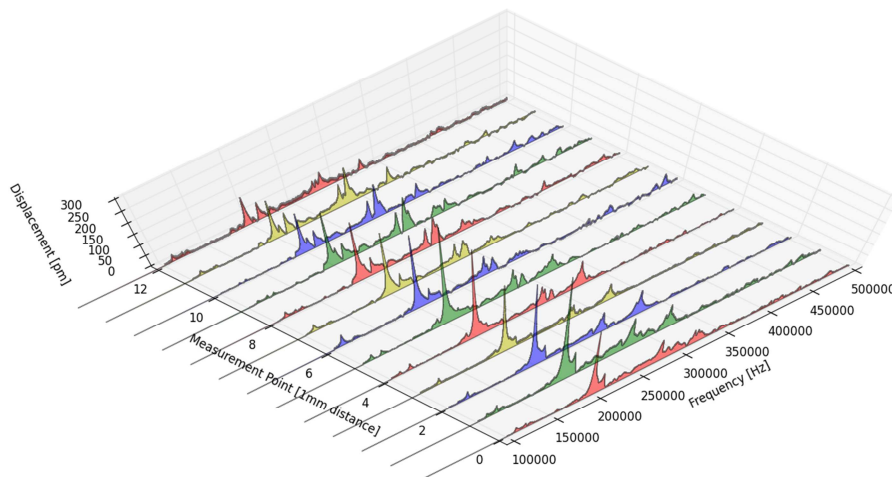


Figure 42: Waterfall graph of epoxide resin PZT side.

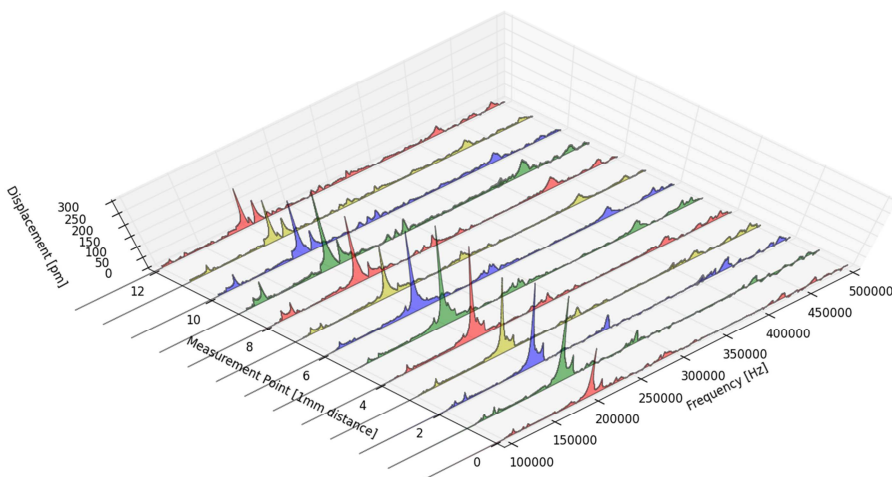
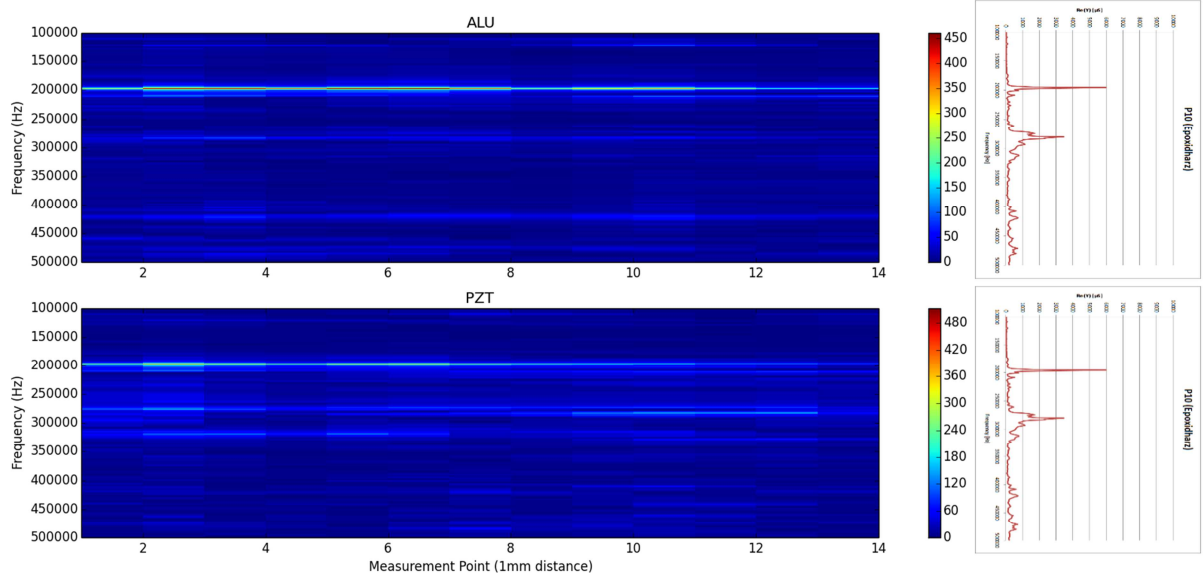


Figure 43: Waterfall graph of epoxide resin aluminum side.

Comparing Figure 42 and Figure 43 it is visible that the 200 kHz resonance manages to go nearly undampened through the glue and aluminum and become wider over the length. The 300 kHz is nearly extinguished through the glue and aluminum volume.

For a different look at the obtained data a 2D color chart was plotted with the displacement over the rainbow colors in picometer (Figure 44). To compare the frequency distribution with the previously measured admittance spectrum it was edited in on the right side.



**Figure 44: Color chart comparison PZT to ALU side with epoxide resin glue. Additionally the admittance spectrum of the PZT was copied to the right side.**

Here it is again visible that the 200 kHz resonance goes nearly undampened through the glue and aluminum volume with a peak of 480 pm PZT side to 450 pm aluminum side and becomes wider on the top right. Also the 300 kHz resonance is basically extinguished and the frequency distribution fits very nicely with the admittance spectrum.

Secondly, the measurements of the super glue sample are presented as waterfalls in Figure 45 and Figure 46.

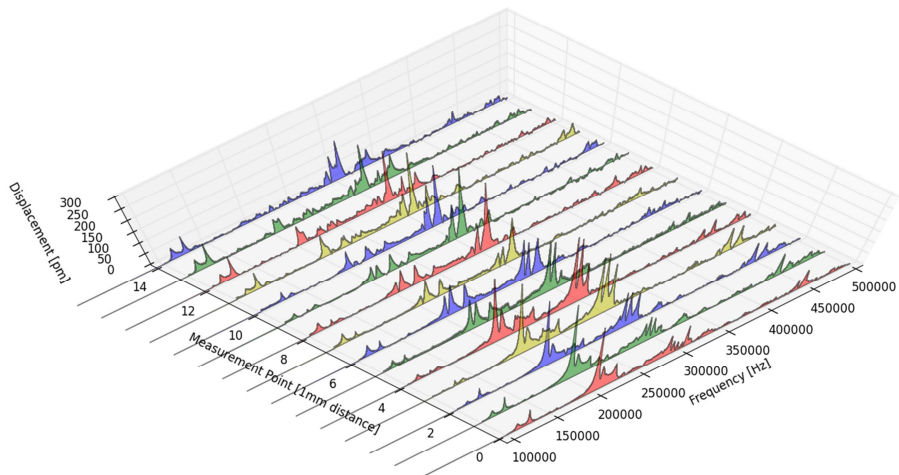


**Figure 45: Waterfall graph of super glue PZT side.**

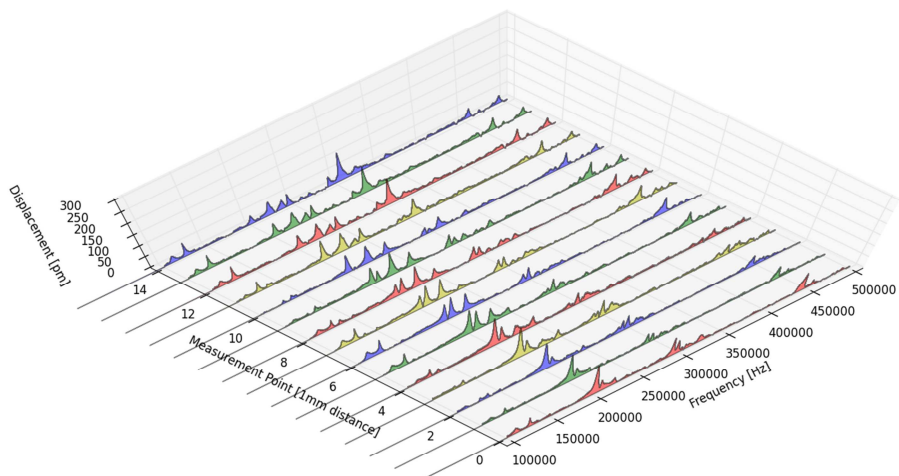


**Figure 46: Waterfall graph of super glue aluminum side.**

Comparing Figure 45 and Figure 46 it is visible that through the super glue the whole spectrum is significantly dampened. Again the 300 kHz resonance is stronger dampened than the 200 kHz resonance and the spatial distribution got wider over the PZT length.

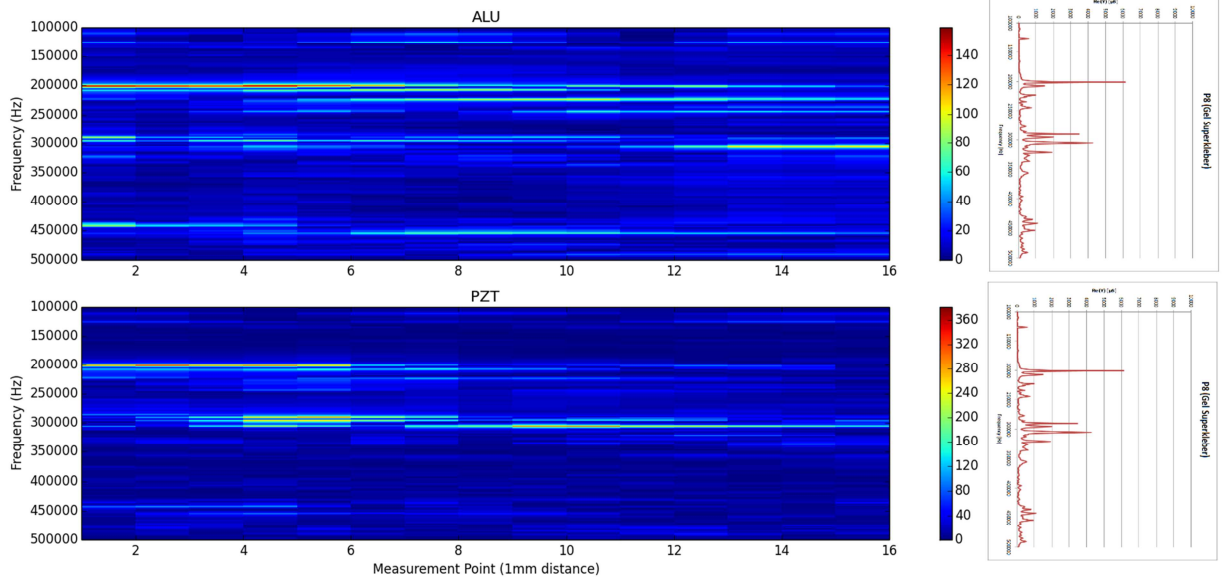
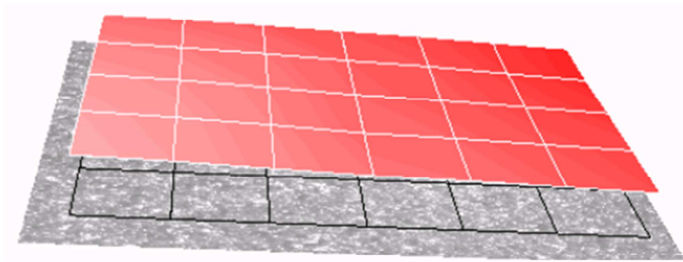


**Figure 47: Color chart comparison PZT to ALU side with commercial super glue. Additionally the admittance spectrum of the PZT was copied to the right side.**

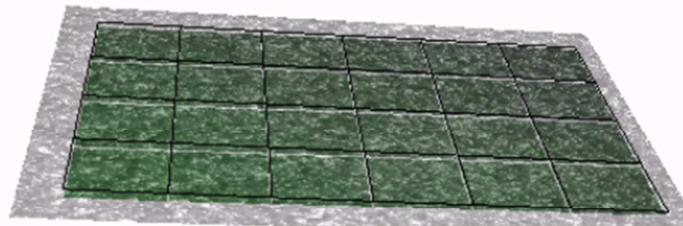
Looking at the color chart the widening and correlation with the admittance spectrum is nicely visible (Figure 47). And considering the color scale the dampening from a peak on the PZT side with 360 pm to a maximum of 150 pm on the aluminum side shows a significantly stronger dampening than with the epoxide resin. Nevertheless we decided to use the super glue over the epoxide resin despite the better coupling for our experiments due to the big advantage of being able to dissolve the glue without destroying any parts of the assembly.

Hereafter the resonance modes of 200 kHz and 300 kHz are presented as screenshots from vibration mode videos.

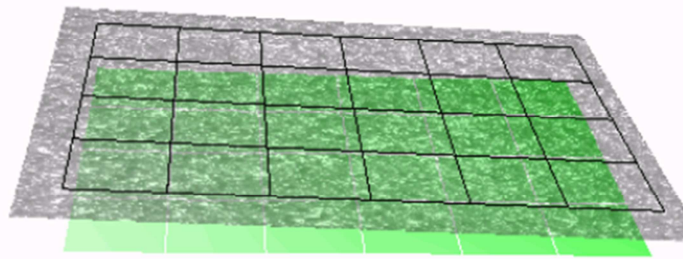
PZT side superglue 201 kHz



t1 – maximum pos. displacement



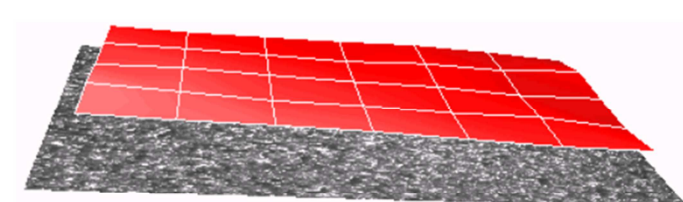
t2 – equilibrium passthrough



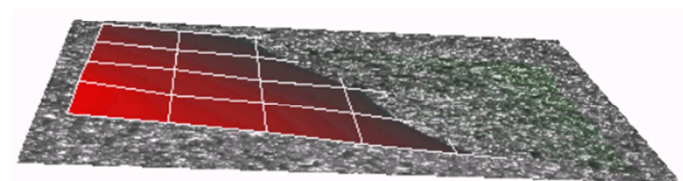
t3 – maximum neg. displacement

**Figure 48: Resonance mode of super glue PZT side 201 kHz frequency. Nearly optimal longitudinal wave as expected of a bulk resonator like PZT.**

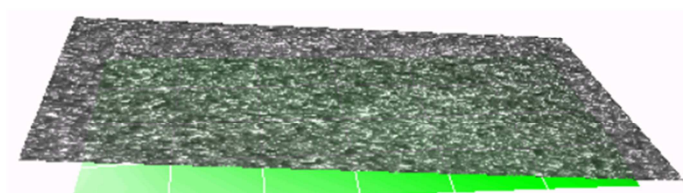
PZT side superglue 305 kHz



t1 – maximum pos. displacement



t2 – equilibrium passthrough



t3 – maximum neg. displacement

**Figure 49: Resonance mode of super glue PZT side 305 kHz frequency. It is visible that it has a transversal wave component due to the uneven pass-through the equilibrium plate.**

As seen in Figure 48 and Figure 49 above which are screenshots at the maximum, minimum and middle of a video displaying the resonance mode it is visible that the 200 kHz is a very nice longitudinal movement whereas the 300 kHz has a transversal component. The transversal wave is best distinguishable at t2 with an uneven pass-through the equilibrium plate and through comparison of the right edge at t1 and t3 as it accelerates faster towards the equilibrium and always passes through first.

### 3.3. Ink experiments

The ink experiments done by Clemens Ditterstorfer, Felix Horak and me showed a very good flow through characteristic, with little dead volume in proximity to the wall and good conformity with the simulation.

From the respective three photo series, 3 characteristic pictures are shown for the flow through of the ink, the first one at t1 which shows a filling profile, at t2 which shows the steady state, at t3 which shows the emptying profile.

In Figure 50 the pump setting was on rabbit, therefore the flow speed was faster and the profile was narrower and faster through the cell. This correlates to the simulation with a higher inlet velocity (see next chapter Figure 54).

Inlet at the bottom; outlet at the top:

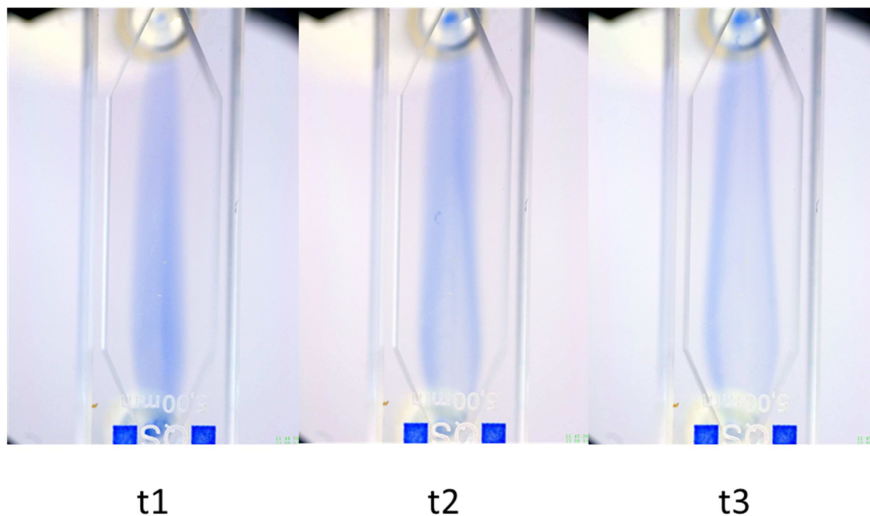


**Figure 50: Ink experiment for fluid characteristic, inlet bottom, outlet top, pump setting rabbit.**

In Figure 51 and Figure 52 the pump setting was on turtle, therefore the flow speed was slower and the profile was wider and slower through the cell. This correlates with the simulation with a lower inlet velocity (see next chapter Figure 53).

Inlet at the bottom; outlet at the top:

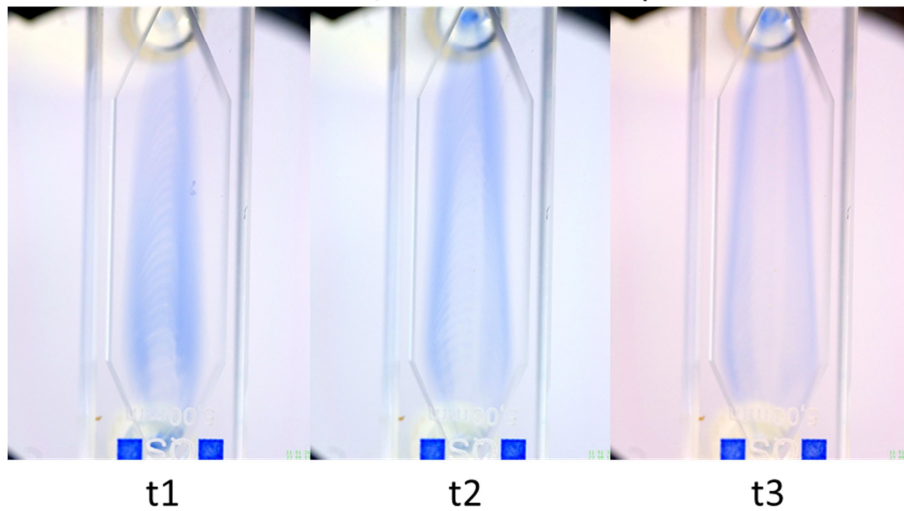


**Figure 51: Ink experiment for fluid characteristic, inlet bottom, outlet top, pump setting turtle.**

In the left picture of Figure 51 the effect of the peristaltic pump is visible through ripples in the ink. The reason is that the flow of a peristaltic pump is not constant, but rather has periodic stops or even backflow for short timeframes.

Inlet at the top; outlet at the bottom:

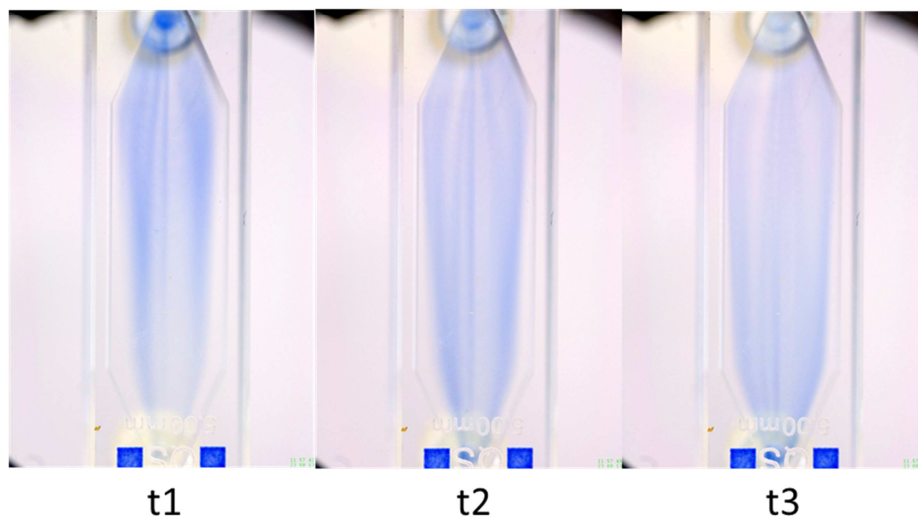


**Figure 52: Ink experiment for fluid characteristic, inlet top, outlet bottom, pump setting turtle.**

There doesn't seem to be any significant difference in a flow with or against gravity for ink experiments. For a particle suspension, however, the gravity might have a stronger influence due to the higher mass of the particles.



### 3.4. Simulation results

#### 3.4.1. Fluid dynamics

The stationary velocity field at a volume flow of approximately 1mL/min in a two dimensional geometry in comparison to the ink experiments results in the following profiles. The inlet speed was estimated with the inlet tube diameter of 0.13 mm to be:

$$v_{in} = \frac{\dot{V}}{A} = \frac{1,67 * 10^{-8} m^3/s}{(0,13mm)^2 * \pi/4} \sim 1 mm/s \tag{Equation 28}$$

Additionally, a profile at  $v_{in}=10mm/s$  was calculated due to underestimation of the inlet geometry and for particle simulation it was advantageous to speed up the process of moving the particles from the inlet into the pressure field.

My colleague Geza proved in his work, that peristaltic pumps are not suitable for ultrasonic resonators due to their periodic pauses/backflows in the flow profile. All my simulations were done assuming the use of syringe pumps which have a constant flow profile  $u_{in}=\text{const}$ .

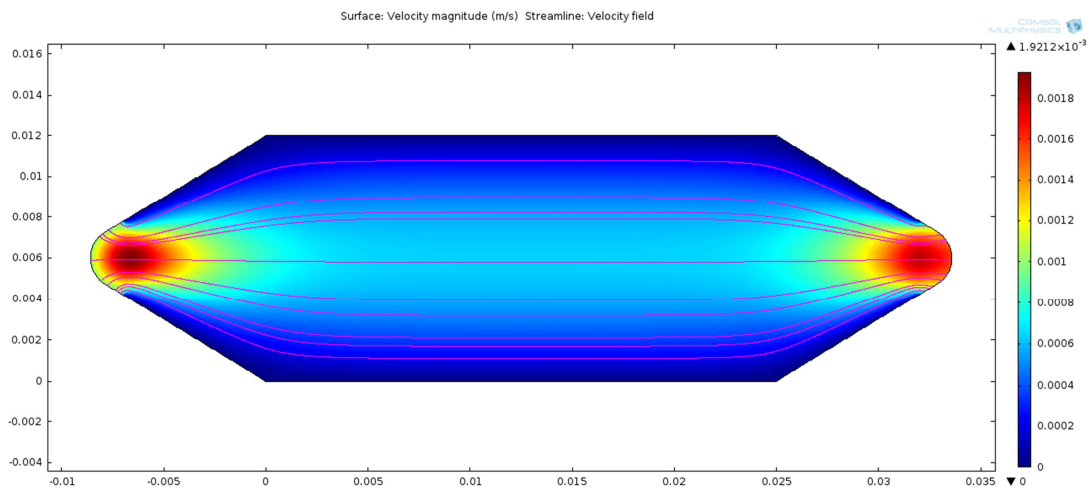


Figure 53: 2D velocity field simulation for cell1 with  $v_{in}=1mm/s$ .

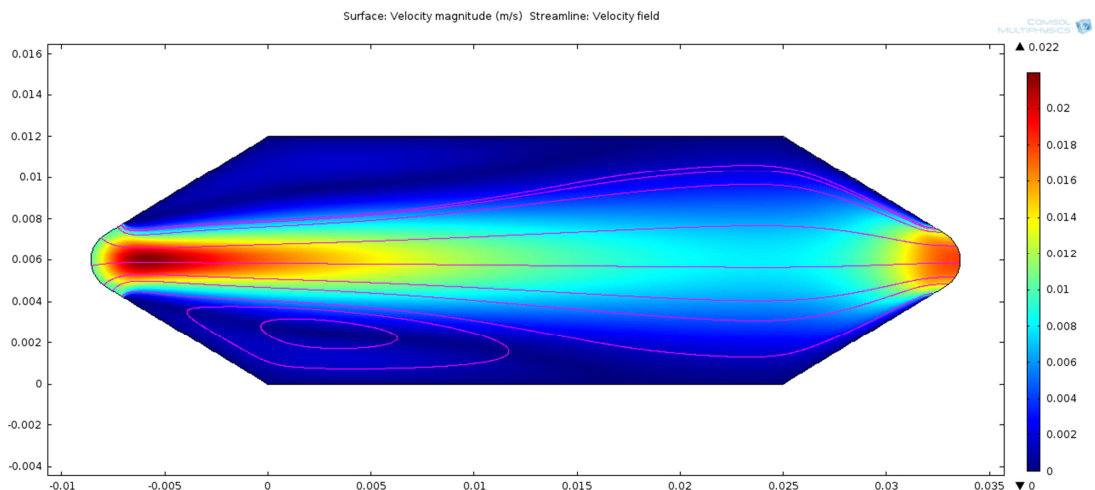


Figure 54: 2D velocity field simulation for cell1 with  $v_{in}=10mm/s$ .

The profiles in Figure 53 and Figure 54 are in good agreement with the ink experiment results.

The results for cell2 are similar with regards to fluid characteristics when the PDMS is included (Figure 55 top), without there is a lot of dead volume in the non inlet/outlet corners (Figure 55 bottom).

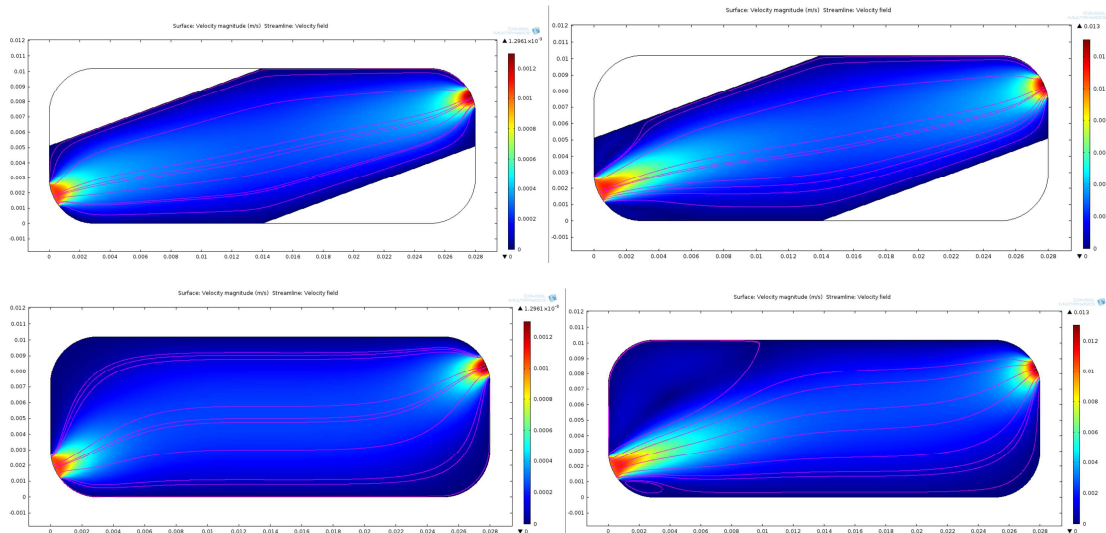


Figure 55: 2D velocity field simulation for cell2 with  $v_{in}=1\text{mm/s}$  on the left and  $v_{in}=10\text{mm/s}$  on the right, the upper row is with PDMS whereas the lower row without.

### 3.4.2. Acoustic characteristics

The 3D Simulation of cell1 with the PZT PIC181 material data, a quartz glass and a water volume without inlet and outlet was simulated for eigenfrequencies and displacement of the PZT for the 201 and 305 kHz resonances. Higher frequencies were not viable in this geometry, since the solver will find eigenfrequencies every few Hertz around 2 MHz which are not usable resonances for particle manipulation. Therefore the resonance frequencies of the vibrometer experiments were simulated: the 201kHz resonance in Figure 56 and two frequencies were found for the 305kHz resonance in Figure 57. The 300kHz resonances also demonstrate how vastly different the acoustic field can be with only a little change in frequency.

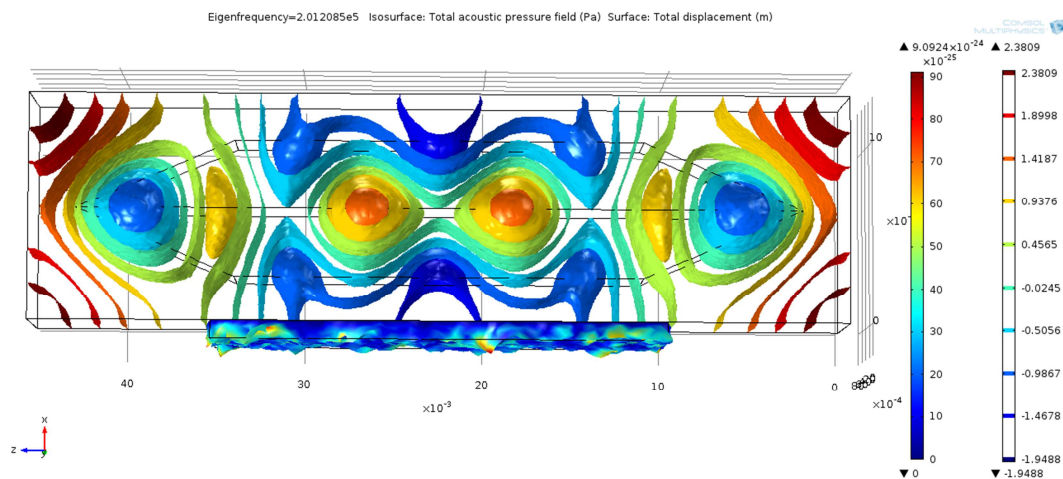
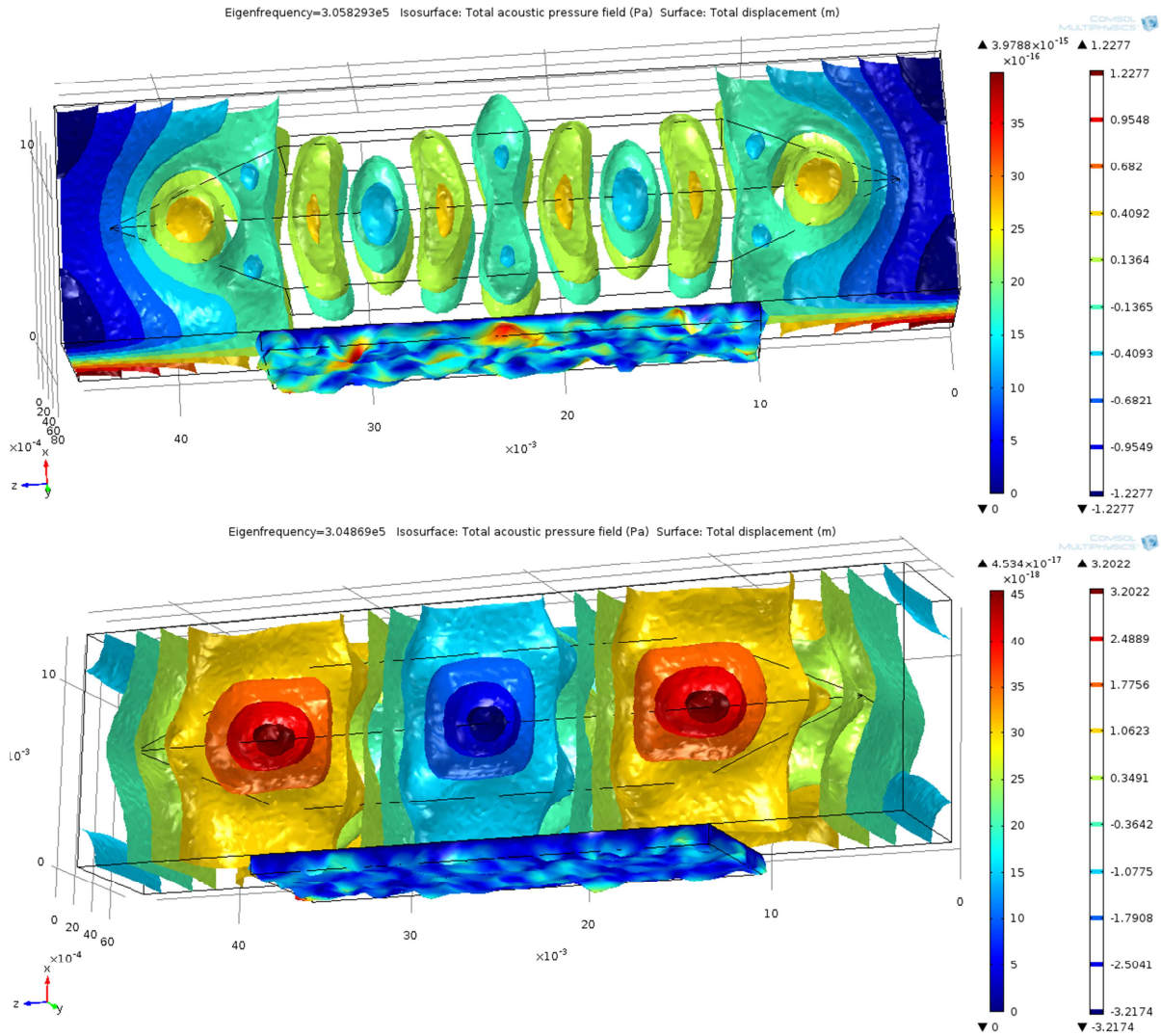
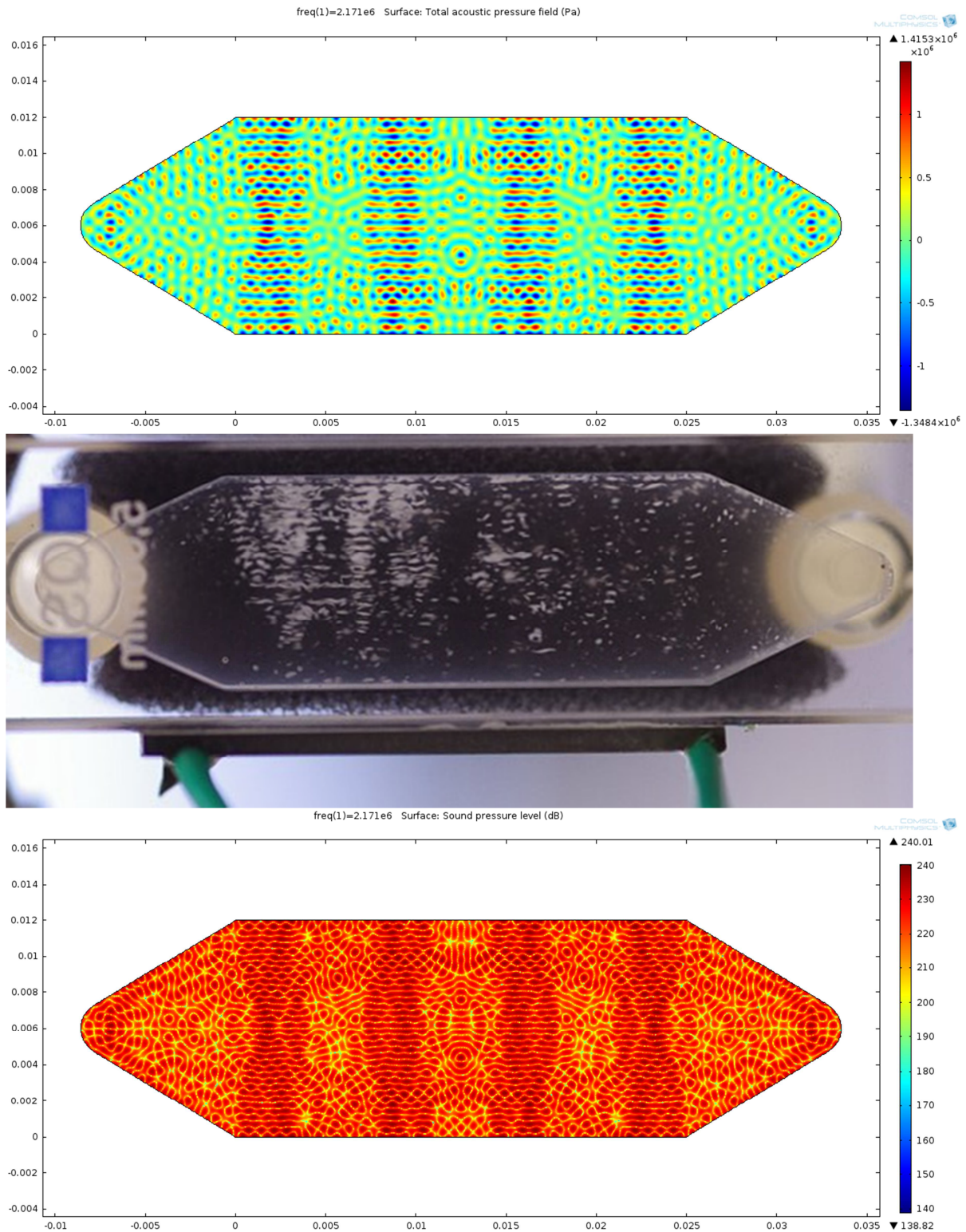


Figure 56: 3D simulation of cell1 acoustic field at 201 kHz.



**Figure 57: 3D simulation of cell1 acoustic field at 305 kHz. The upper picture displays an eigenfrequency resonance at 305.8kHz, the lower one at 304.9kHz.**

All further simulations were done in two dimensions to reduce the processing time and to be able to add particles in an easier displayable way for better understanding of our cell.



**Figure 58: 2D simulation of cell1 acoustic field at 2.171 MHz, upper picture displayed with total acoustic pressure in Pa, middle a picture of the real set-up in comparison and lower picture with sound pressure level in dB.**

In Figure 58 the acoustic field is shown in a 2D view at 2.171 MHz. The simulation was done for the total acoustic pressure field (top) and for the sound pressure level (bottom). Both can be compared to the reality of the experiment (middle) at the same frequency powered by one PZT at the bottom.

In the photograph of the cell it is visible that the field is stronger at the reflector, there are, however, too few particles for a thorough comparison.

In Figure 59 the cell is compared in the same way as above with the simulation and the reality but for the 6.666 MHz there were two PZTs at the top and bottom electrically parallel which created the acoustic field. This time a lot of particles were used but due to the fineness of the higher resonance field and the third dimension depth it's also not easily comparable but appears to be similar.

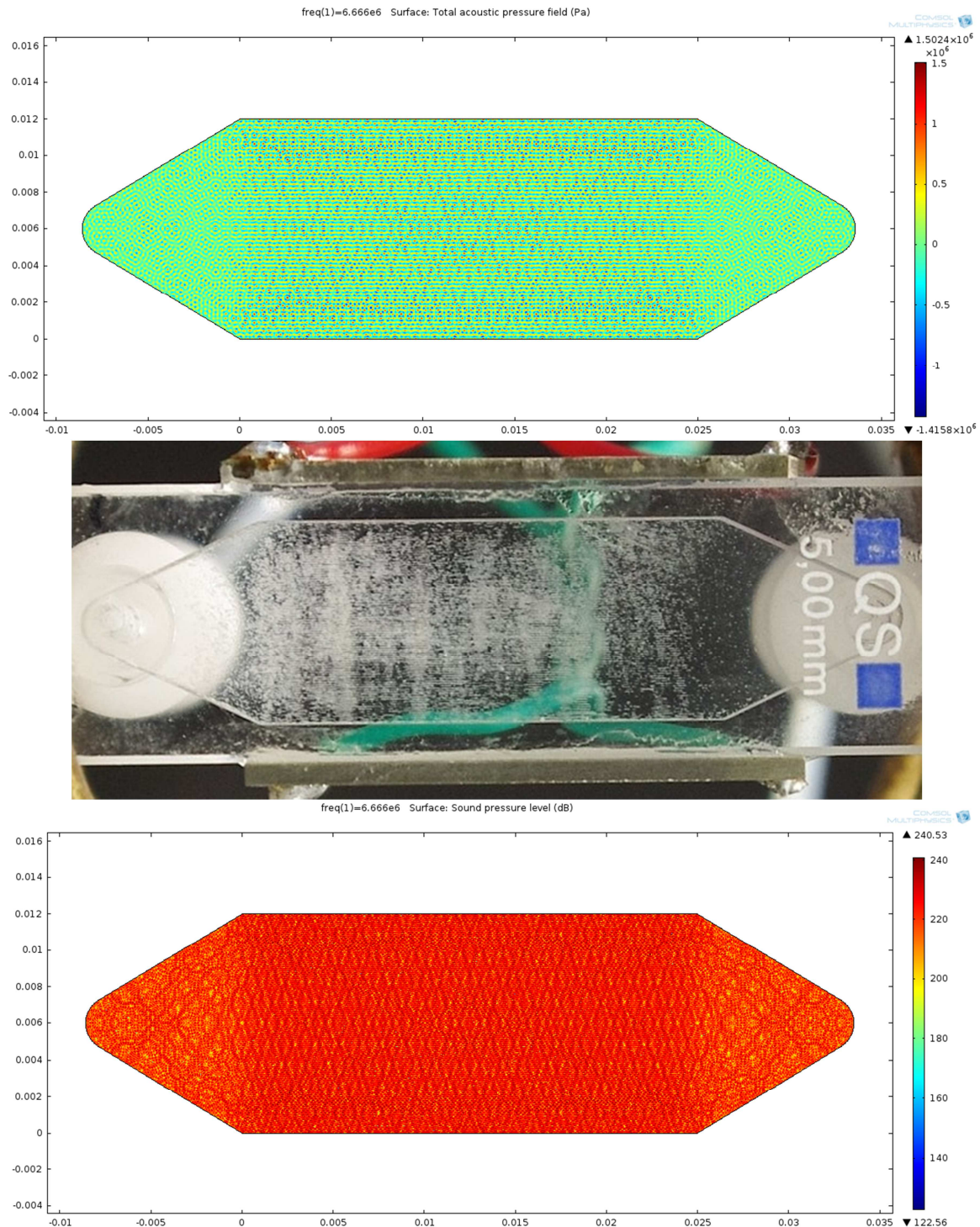


**Figure 59: 2D simulation of cell1 acoustic field at 6.666 MHz, upper picture displayed with total acoustic pressure in Pa, middle a picture of the real set-up in comparison and lower picture with sound pressure level in dB.**

In Figure 60 the acoustic field of cell2 was simulated and the effects of PDMS were investigated. The idea was to use a material with the same density and speed of sound as water for optimal acoustic planes. The top picture was calculated using the same density and speed of sound for the wedges in the top left and bottom right corners. However PDMS does have a different speed of sound than water which was used to calculate the bottom picture. Due to the not ideal acoustic impedance match the planes get disturbed and the difference in the speed of sound is nicely visible in PDMS by the different spatial distribution distance of the maxima and minima of the acoustic field.

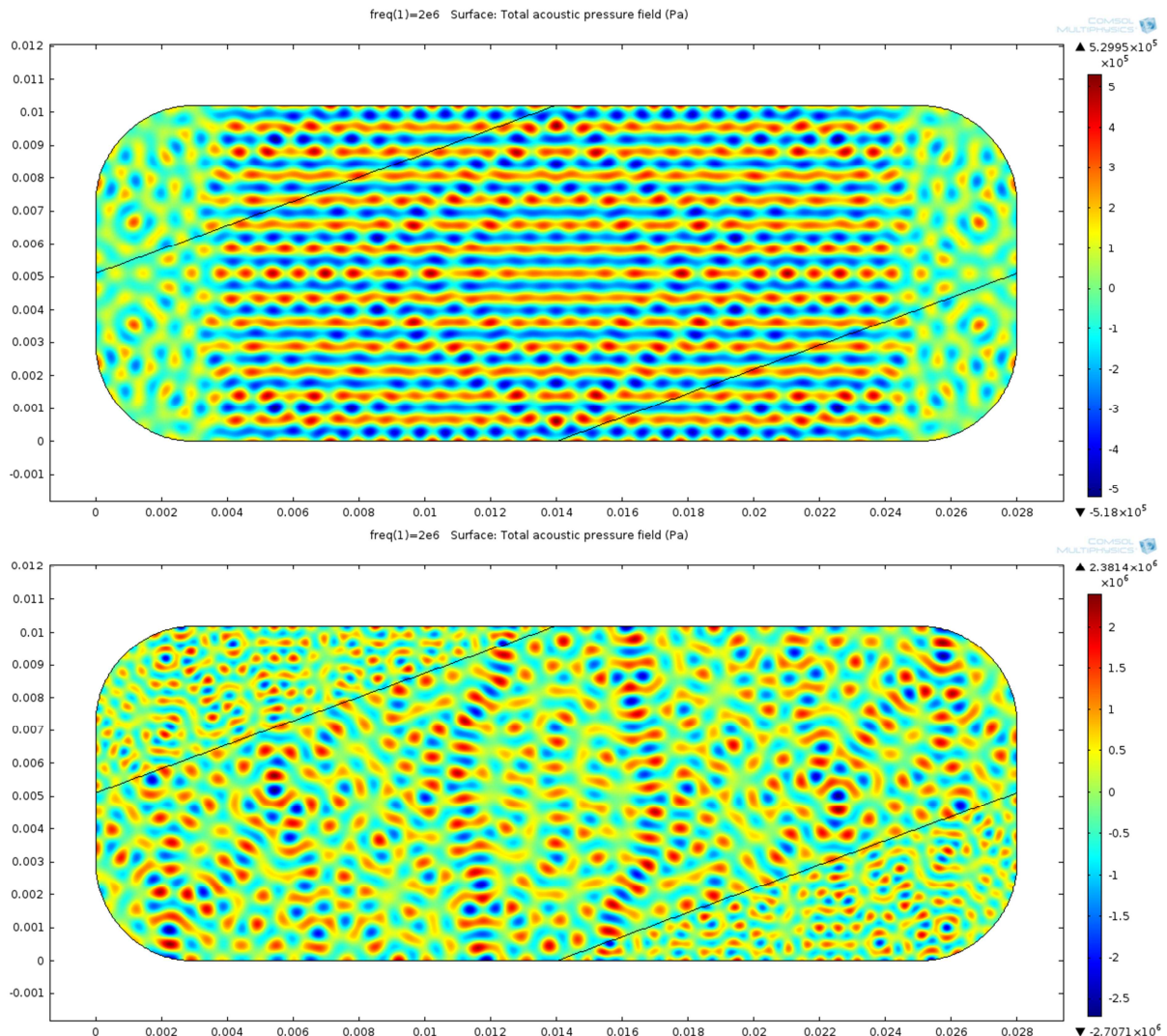


**Figure 60: 2D simulation of cell2 acoustic field at 2 MHz with and without PDMS, upper picture is acoustic field without PDMS and lower picture is acoustic field with PDMS.**

### 3.4.3. Particle manipulation

For simulations usually it was chosen to fill the volume with particles like in the 0.5-2-2.5 experiments, which means particles are distributed on the mesh at time 0 and are continuously added from the inlet.

In Figure 61 3  $\mu\text{m}$  particles are shown in a ten times smaller geometry with initial filling of 1000 particles and additionally an inlet with a speed of 1mm/s of 20 particles in uniform distribution every 0.01sek for 0.5sek. From the movie three pictures are shown with magenta streamlines of the

velocity field, acoustic field represented in rainbow colors and particles in grayscale depending on their speed with three times bigger radius for better visibility.

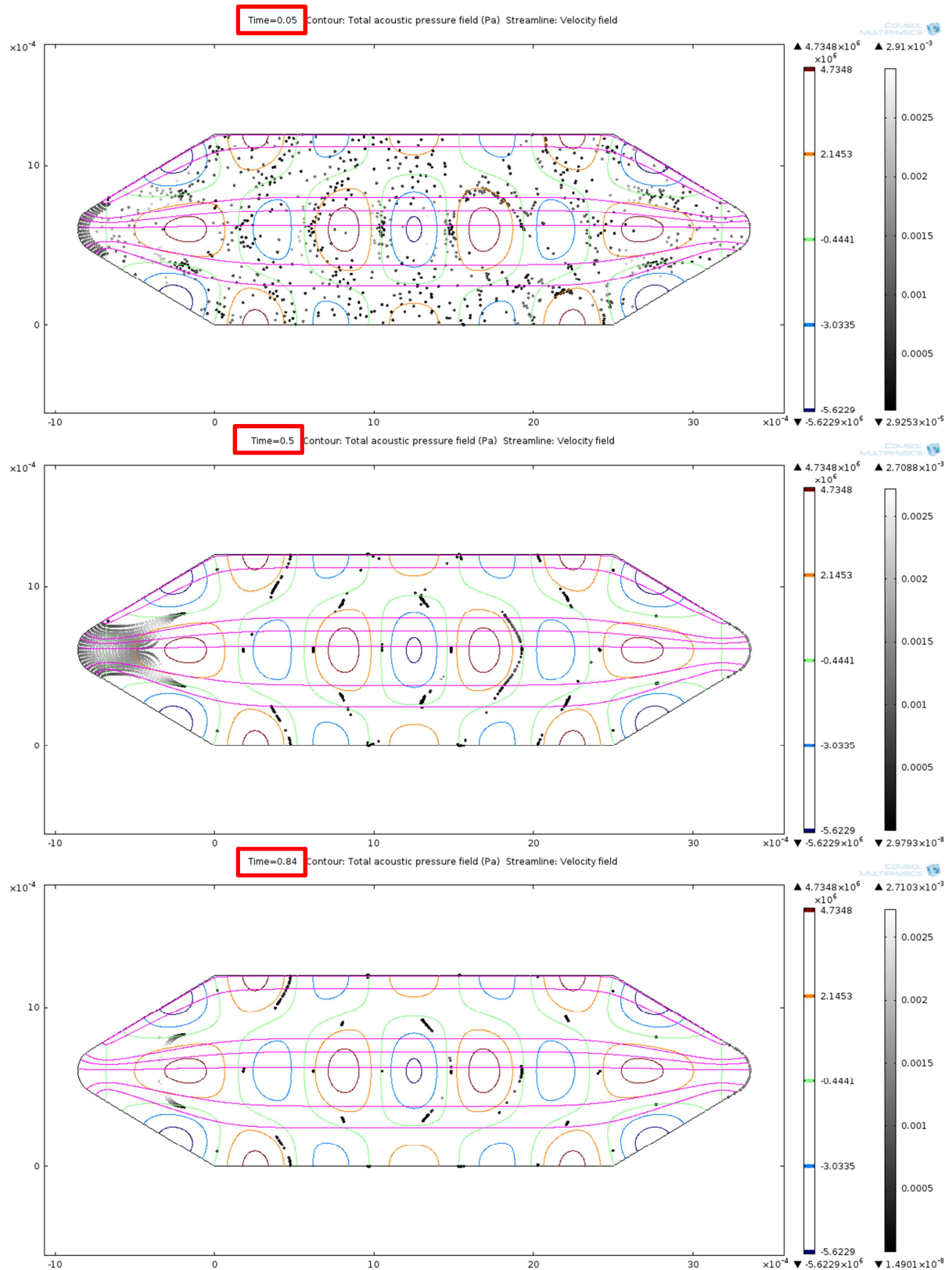


**Figure 61: 3µm particles reacting to the acoustic and velocity field.**

The picture series in Figure 61 is without particle interaction so after some time the particles trapped in the cell will completely overlap at the strongest point in the acoustic nodal planes, which are

usually near the green lines. The simulation with  $3\mu\text{m}$  particles has retention of 100%. It has to be noted, that due to the geometry shrinking and the strong influence from the reflections at the tips on the side the acoustic field looks differently than to the real geometry (here only 2 pressure nodes!). It appears to have now additional perpendicular planes to the propagation direction of the PZT. But for the purpose of these simulations of particles - field interaction it's of less importance because the particles are small enough compared to the acoustic field and always react the same as long as a pressure distribution exists.

In Figure 62  $2\mu\text{m}$  particles are shown in a ten times smaller geometry with initial filling of 1000 particles and additionally an inlet with a speed of  $1\text{mm/s}$  of 20 particles in uniform distribution every 0.01sek for 0.5sek. From the movie three pictures are shown with magenta streamlines of the velocity field, acoustic field represented in rainbow colors and particles in grayscale depending on their speed with three times bigger radius for better visibility.



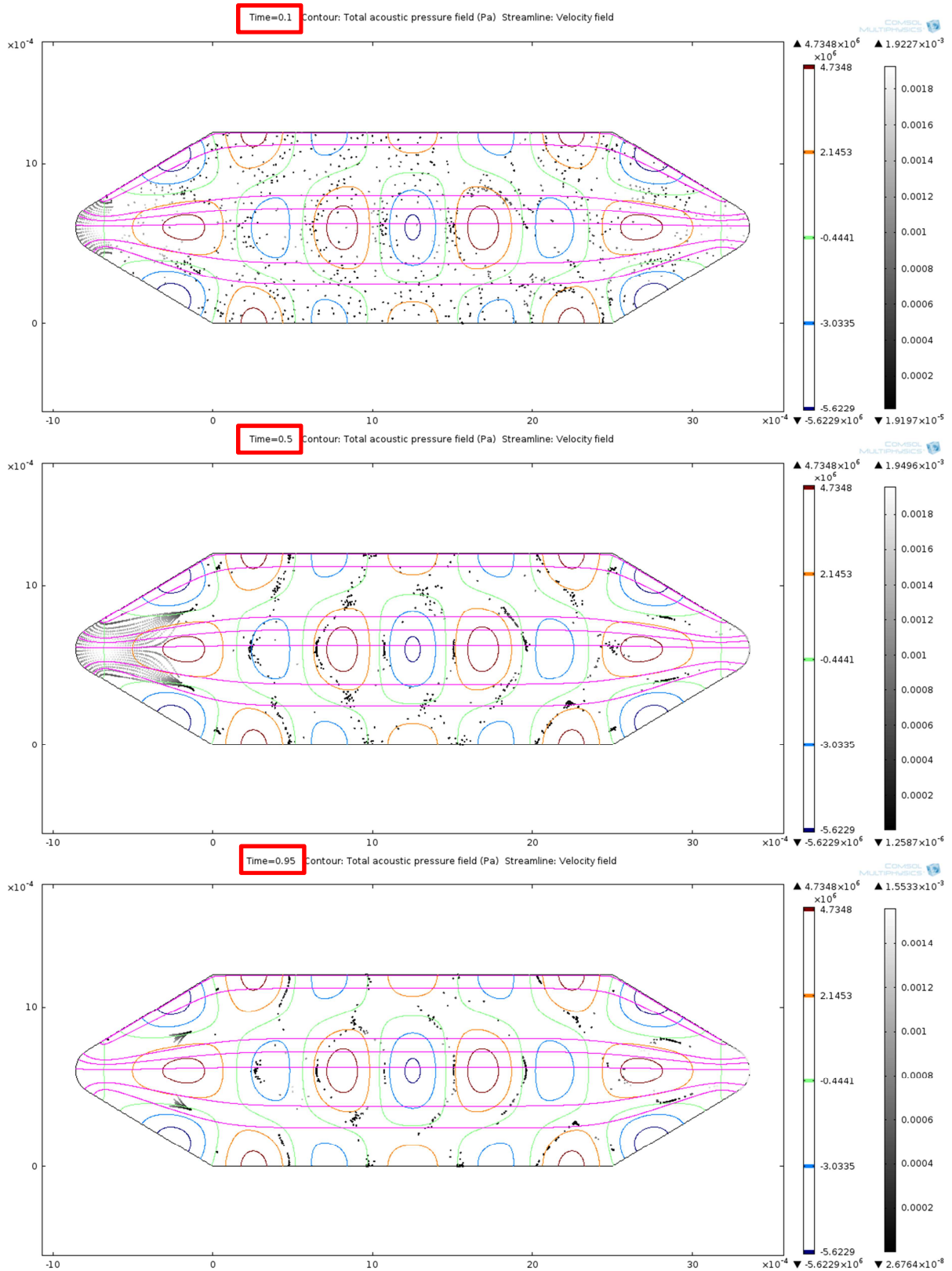


**Figure 62: 2µm particles reacting to the acoustic and velocity field.**

The simulation with 2µm particles has retention of 100% but it is already noticeable slower reaction in time and weaker strength in the spatial distribution visible by a bigger spread of the particles. It is also nicely visible that all inlet particles get stuck and overlap at the first possibility in the nodal plane.

In Figure 63 1  $\mu\text{m}$  particles are shown with the same simulation parameters and graphical displays as the previous two particle simulations.

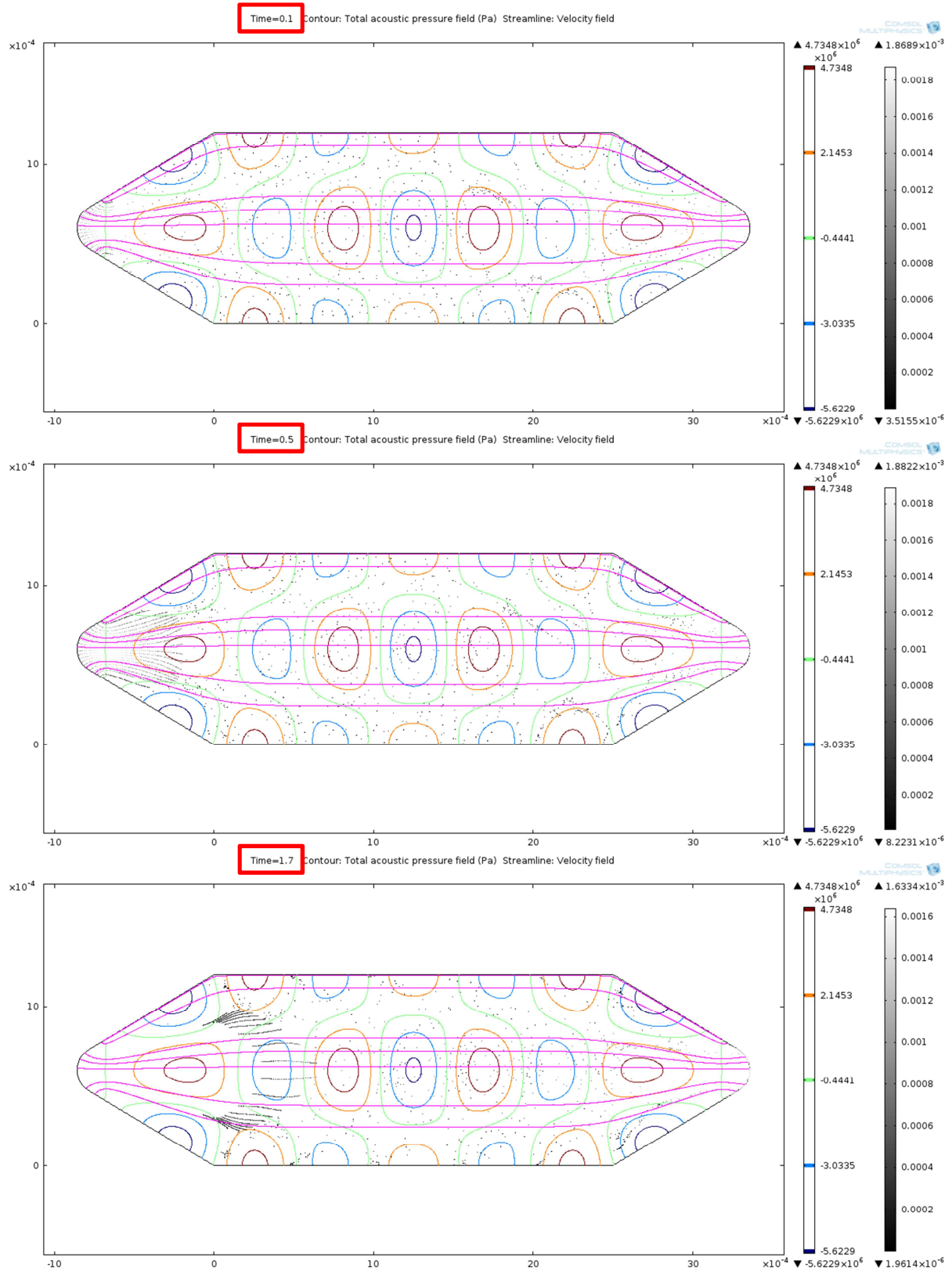


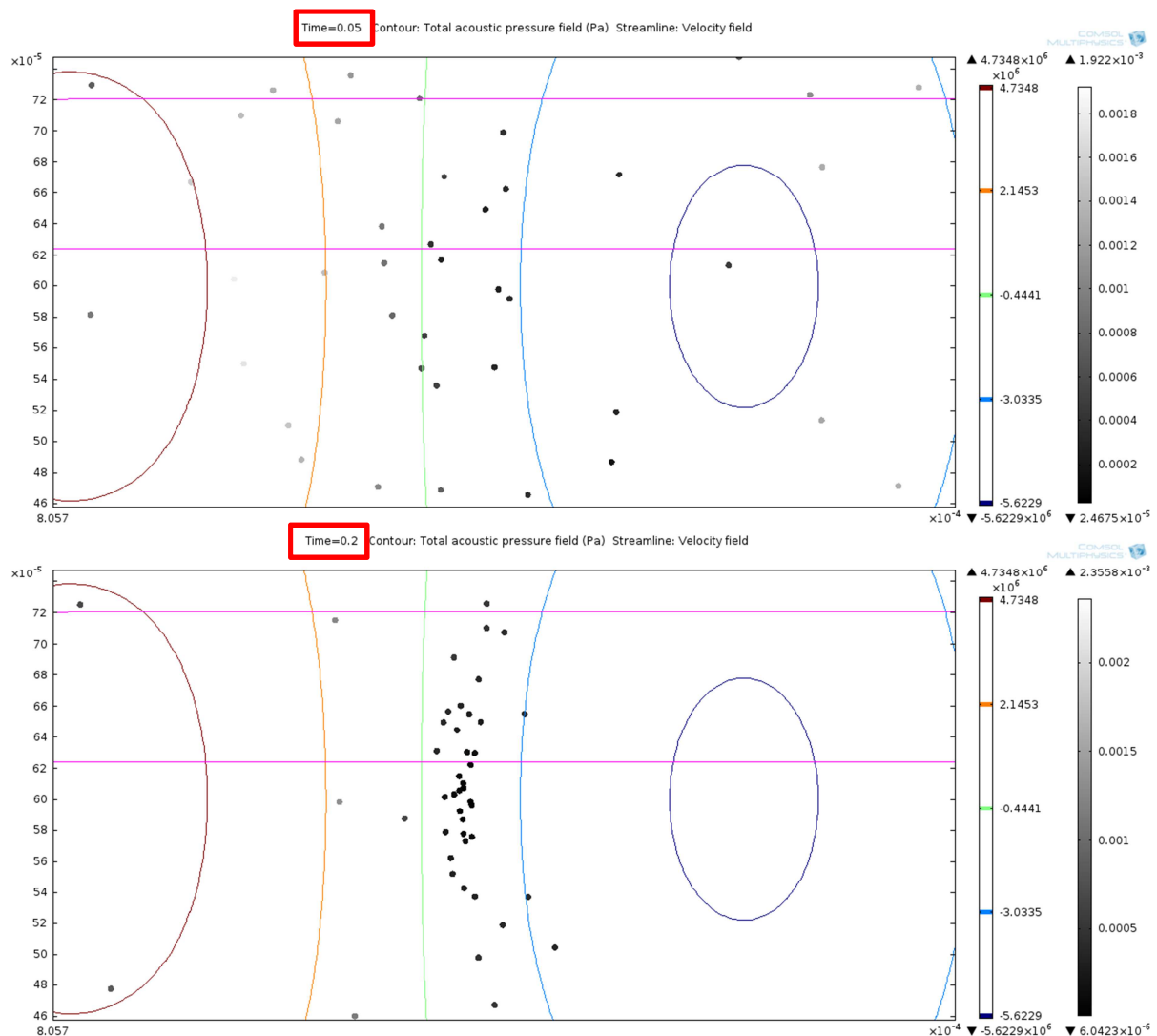
**Figure 63: 1 $\mu\text{m}$  particles reacting to the acoustic and velocity field.**

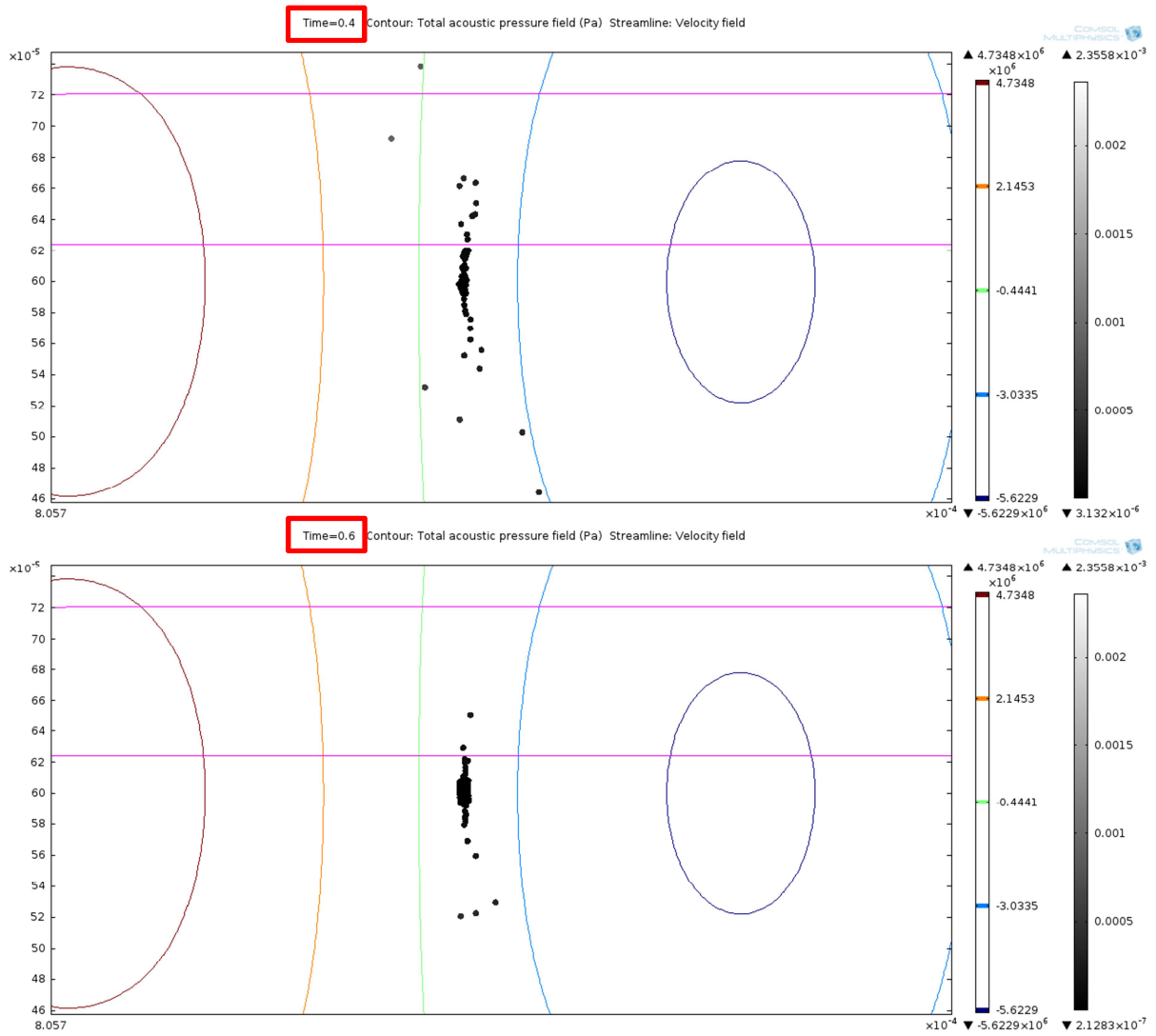
1  $\mu\text{m}$  particles are not really reacting with the acoustic field anymore in the simulation and the retention reaches around 10% at the top and bottom of the cell. This is due to the mesh size and the

acoustic force getting weaker, in reality the particles create agglomerates and become visible thanks to that. Because in general it's not possible to see the particles with the eye, only an opaqueness of the liquid is visible. As shown in chapter 2.1 our single particles are mostly smaller than  $1\mu\text{m}$  but if two or three agglomerate by coincidence or due to getting pushed together by the acoustic field their interaction with the field increases and the retention increases as well.

So the next step for the simulation was to include particle-particle interaction to simulate the agglomeration since we believe it has a huge impact on the retention of smaller particles.

The particle interaction was simulated with  $2\mu\text{m}$  particles and a zoomed in picture of a middle nodal plane is shown in Figure 64. One can see that agglomerates build up quickly at the focal points of the acoustic field and then stretch along the nodal plane when new particles get caught. The agglomerate arranges itself in a very dense packing of a few particle width and seemingly unlimited particle length along the nodal plane.





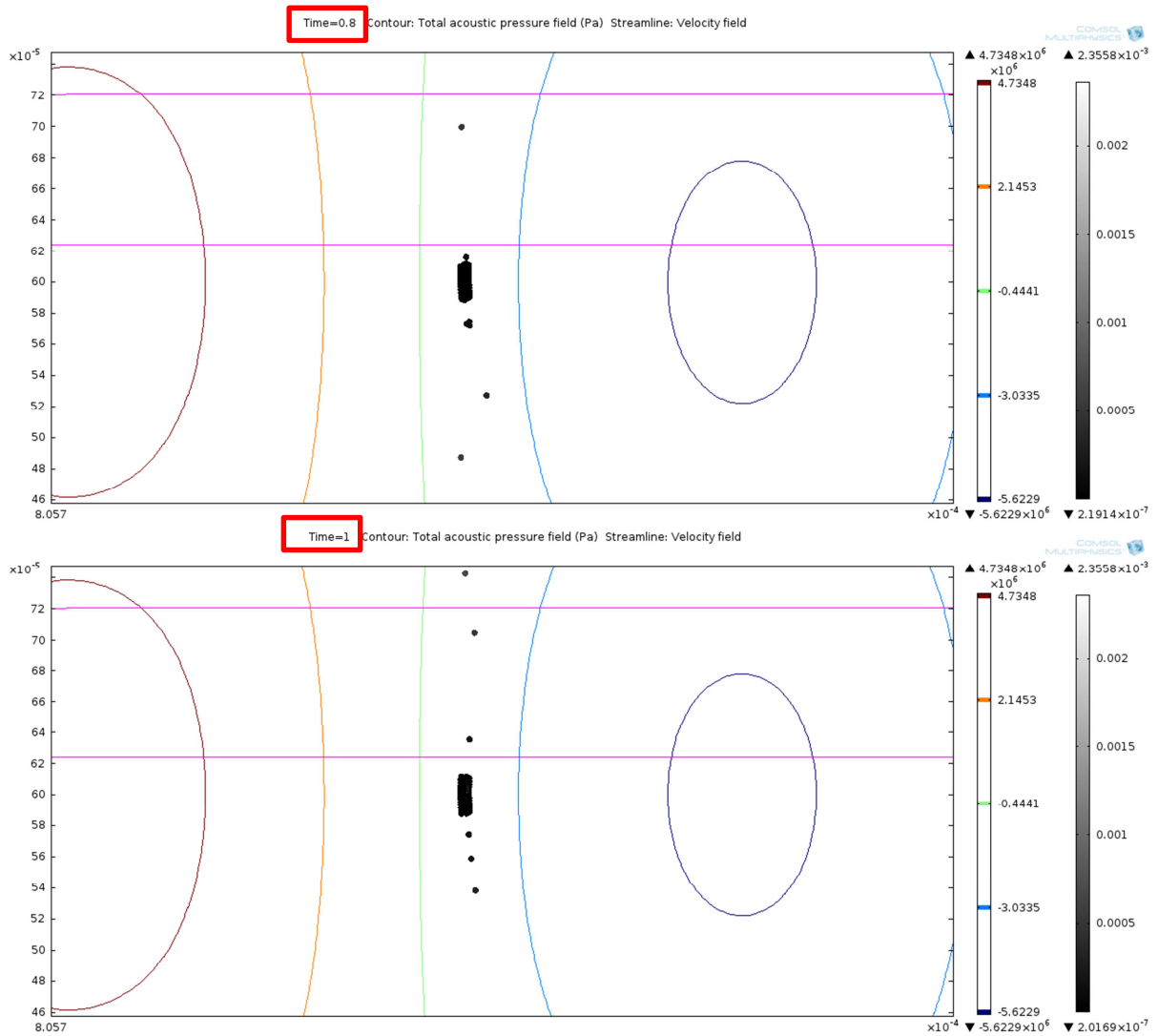


**Figure 64: 2µm particles with particle-particle interaction, development of an agglomerate.**

In Figure 65 the path lines are displayed to show where the particles came from and how some went against the fluid flow direction and on curved paths.

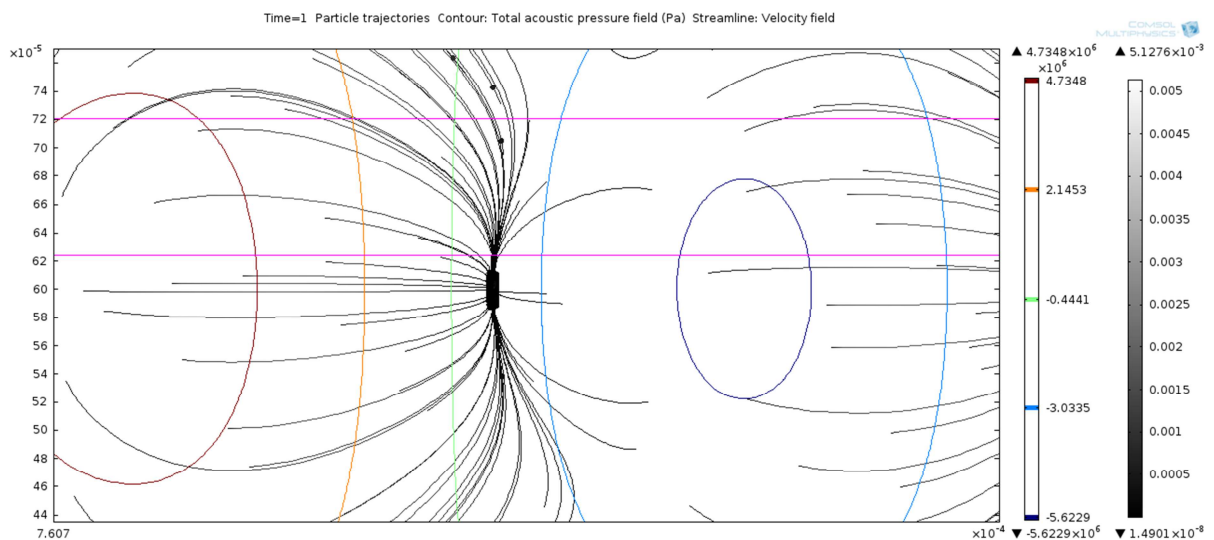


**Figure 65: 2µm particles with particle-particle interaction path lines.**

In Figure 66 a more detailed zoom was done on the agglomerate, to improve visibility of the single particles the displayed radius was halved. Therefore the single particles tend to overlap with  $\frac{1}{4}$  of their radius due to the weaker Lenard Jones potential and the strong acoustic radiation force. In the first picture a single particle joins the agglomerate from above and a 3-particles-agglomerate joins from below. In the next picture shortly after, a stress in the agglomerate is visible in the grayscale of particle speed which usually happens as a shockwave after absorbing new particles and which resulted in previous simulations in an explosion of the agglomerate. But for this simulation the particles “calm down” after a short time and are perfectly captured.

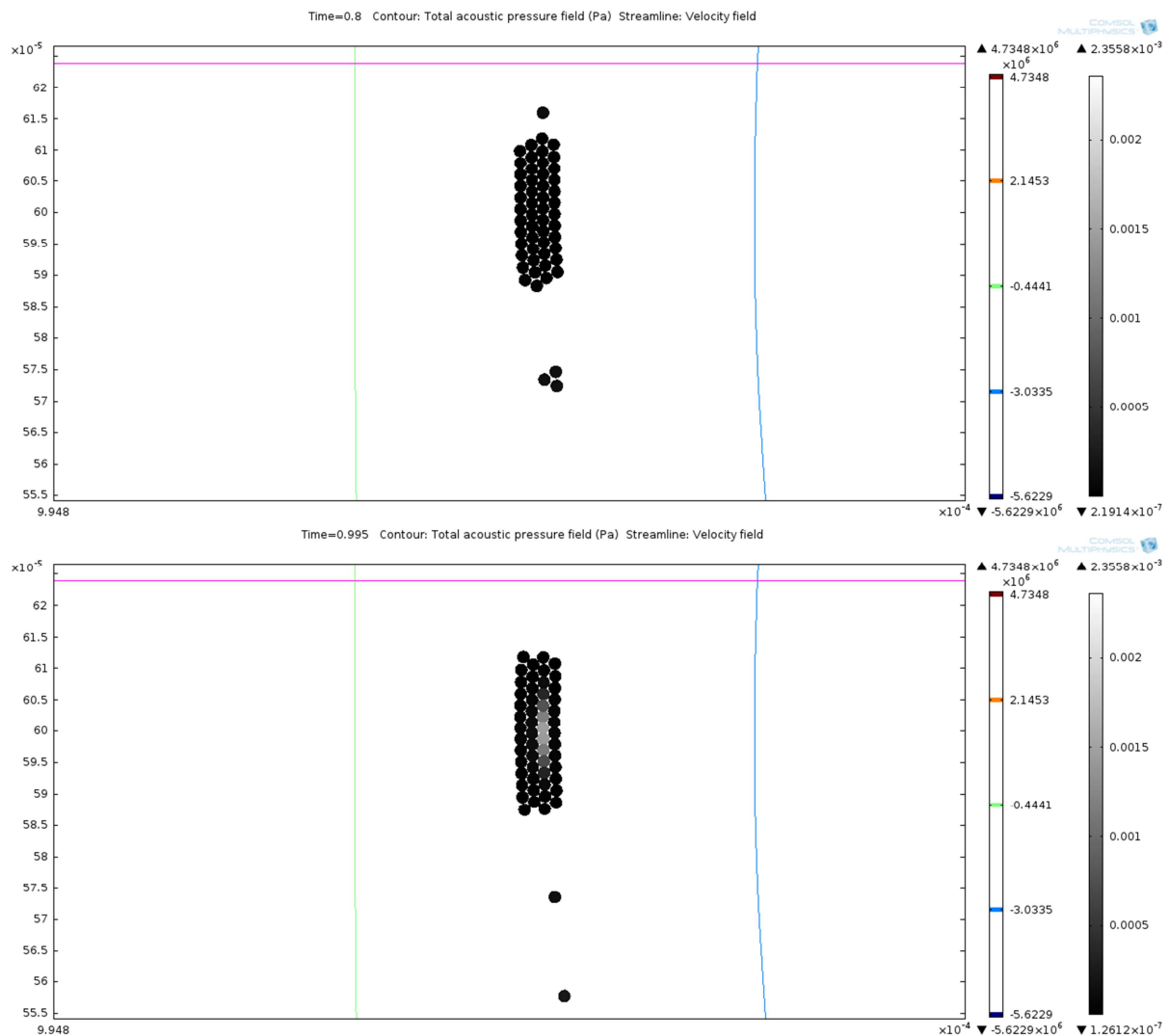


**Figure 66: 2  $\mu\text{m}$  particles with particle-particle interaction, with half radius for visibility due to overlapping. In the upper picture a 3-particle-agglomerate joins the big one from below and a single particle from above. On the lower picture is the final constellation at the end of the simulation where some stress in the agglomerate is visible through the grayscale.**

At the end of this chapter a short comparison with the reality also at 2 MHz with similar particle concentration will be shown in Figure 67, with red bordered a possible region of the simulation.



**Figure 67: Photograph of cell1 driven at 2 MHz. Agglomerates of MCM-41 particles are clearly visible.**

It is not too far away from the simulation, with agglomerate size and density and therefore a somehow reasonable modeling.

### 3.5. ICP-OES results

The inductively coupled plasma - optical emission spectrometry (ICP-OES) experiments were performed to quantify the actual retention of the cell as a proof of concept. The settings were as described in chapter 2.7. The particle concentration varied for the suspension feed with usually a few hundred  $\mu\text{L}$  per 40mL 1%  $\text{HNO}_3$ . It was always mixed high enough to have at least a 3000 count/s signal for the silicon 251.6 nm characteristic line. The other characteristic lines (the second silicon and three zircon lines) were kept for possible cases when the main line overflows due to oversaturation at the detector.

#### 3.5.1. Filling the cell

The first concern to clear was how long it takes the setup to replace the cell volume. For that we simply filled it with a distilled water/ $\text{HNO}_3$  blank, changed the feed to a particle suspension and got the following result how long it takes till the particle signal is stable.

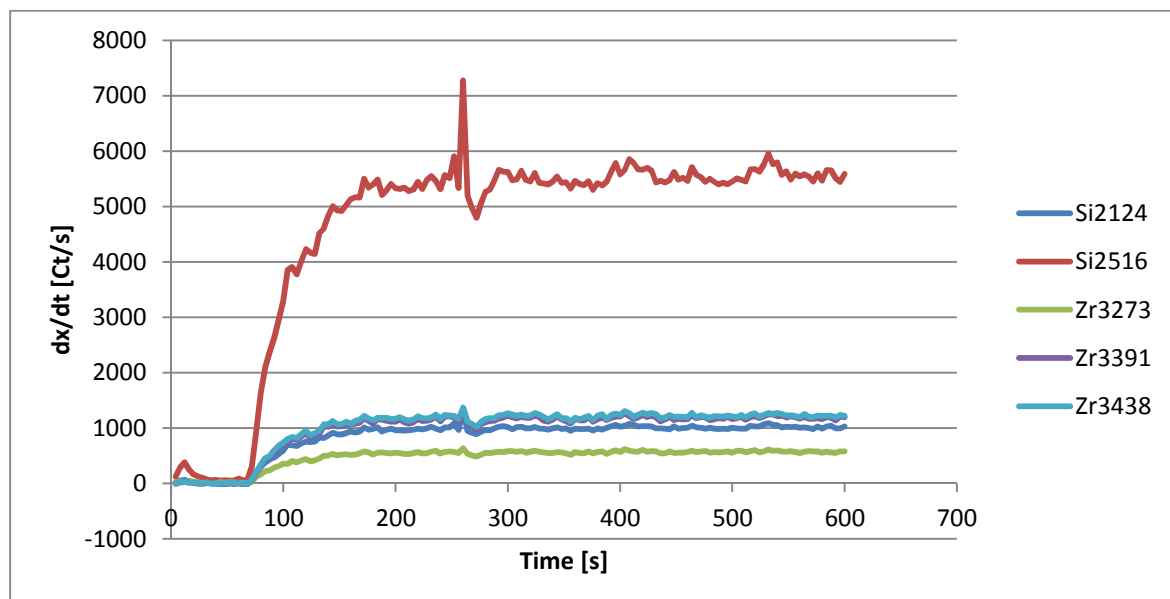


**Figure 68: ICP-OES readings over time at different elemental lines (Si 251.6 & 212.4 nm; Zr 327.3 & 339.1 & 343.8 nm) during filling of cell1 with a particle suspension.**

As seen in Figure 68, it takes around 60 seconds until the first particles give a signal and around 200 seconds to replace the volume of the cell and tubes with the particle suspension to get a stable signal at the ICP-OES. The peak at around 260 seconds could be an air bubble which is the worst enemy of all our experiments, or it could be a flow-through of a big particle agglomerate.

### 3.5.2. 0.5 – 2 – 2.5 measurement

The first comparison was how much the change in retention is, if the flow goes with or against gravity as shown in Figure 69 and Figure 71.

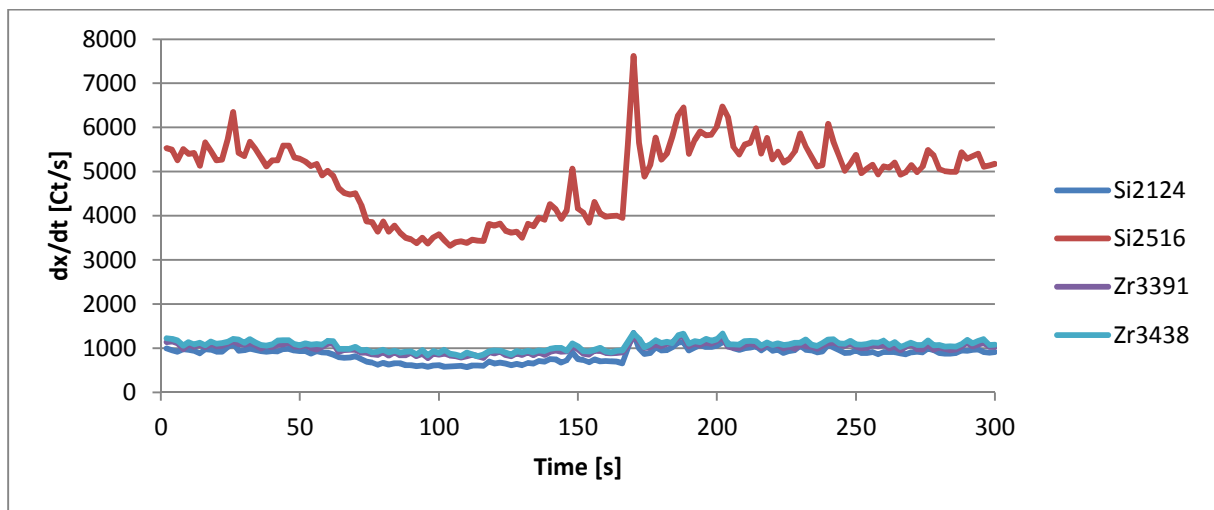


**Figure 69: Filtering with gravity, the retention is visible between 60 and 160 seconds.**

Filtering with gravity has the advantage that the cell doesn't need to be touched, but has slightly lower retention and is significantly worse to flush out agglomerates. Because there is the danger of particle agglomerates getting too big and settling at the bottom of the cell despite the water flow.

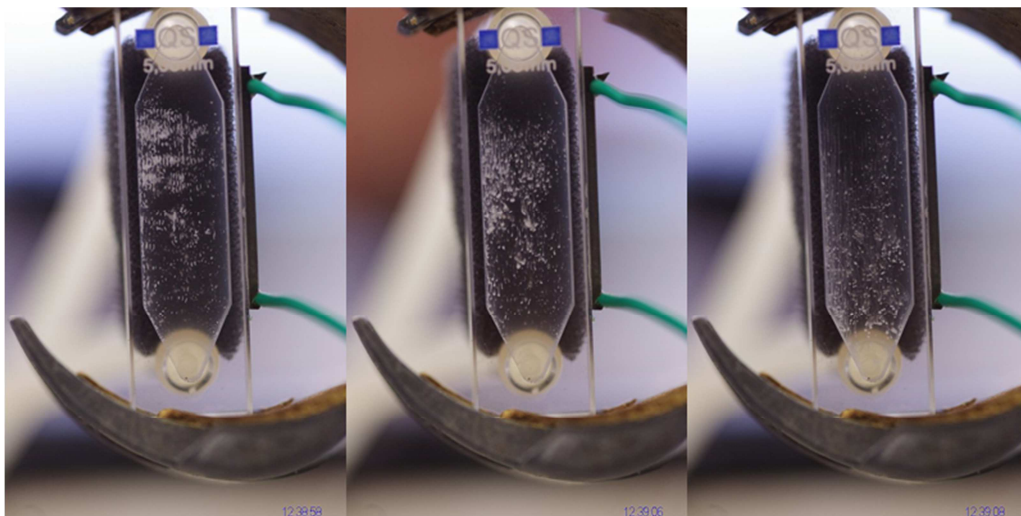


**Figure 70: Pictures of the effect when switching off the acoustic field.**



The other method was to setup the flow against gravity with turning the cell before turning off the acoustic field.

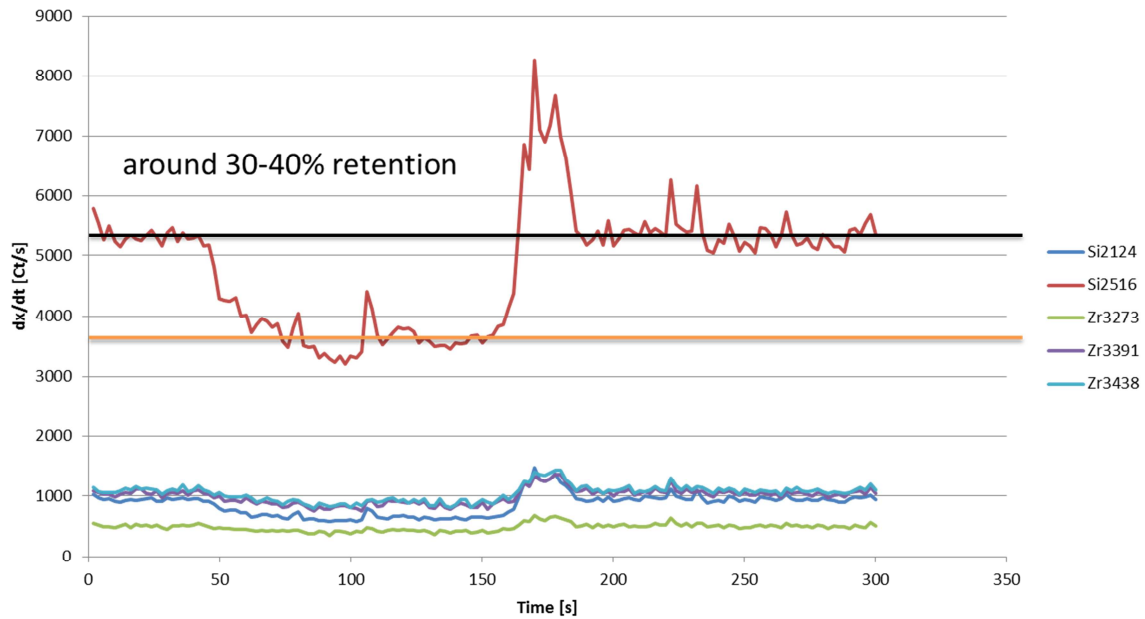


**Figure 71: Filtering against gravity, the black line is the estimated mean signal without the acoustic field, the orange line is the estimated mean signal with an active acoustic field.**

This has the advantage of better retention and a nice flush out characteristic (the peak at 160 seconds in Figure 71) after turning off the acoustic field, but needed additional handling to turn around the cell which was done by hand for the measurements here. An automatic process was developed to turn the cell around with a motor, more about that concept is written in the appendix.

The repeat of the experiment with a syringe pump after realizing how badly the peristaltic pump flow characteristic influences the acoustic particle manipulation is shown in Figure 72.

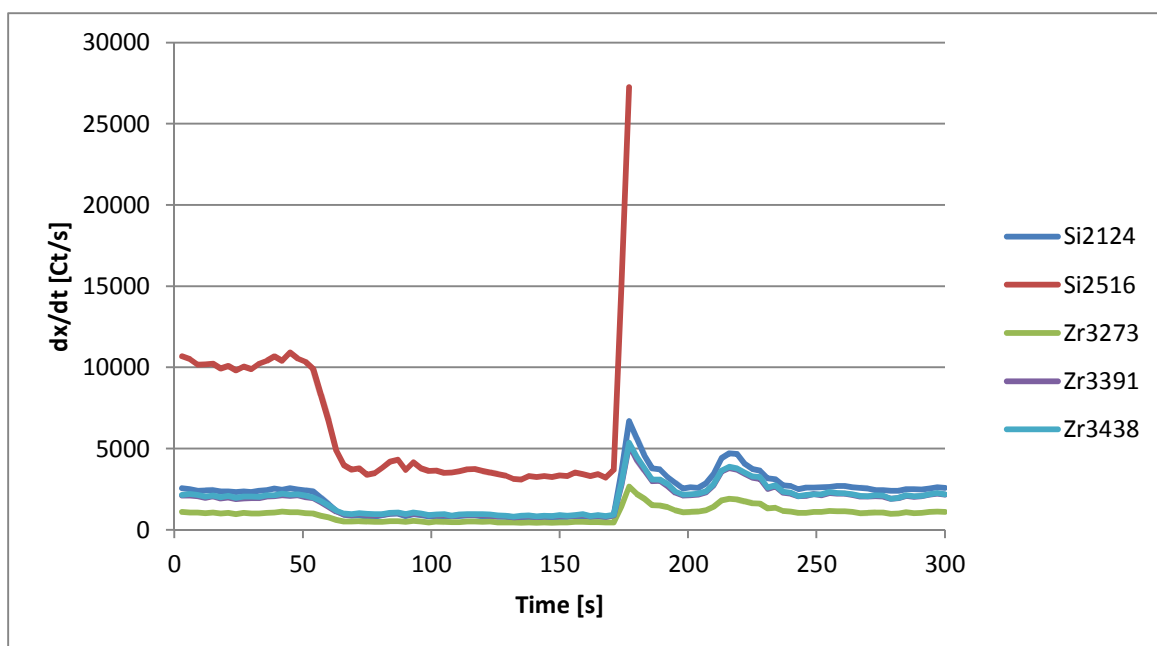


**Figure 72: Filtering against gravity with turnaround using a syringe pump.**

In this setup the retention reaches around 65% and the whole signal becomes smoother, even the flush out characteristic is getting better and saturating the main silicon line.

### 3.5.3. 5 – 9 – 1 measurement

The main reason for this measurement is to see how strongly particles are kept in the acoustic field and was only done with a peristaltic pump.

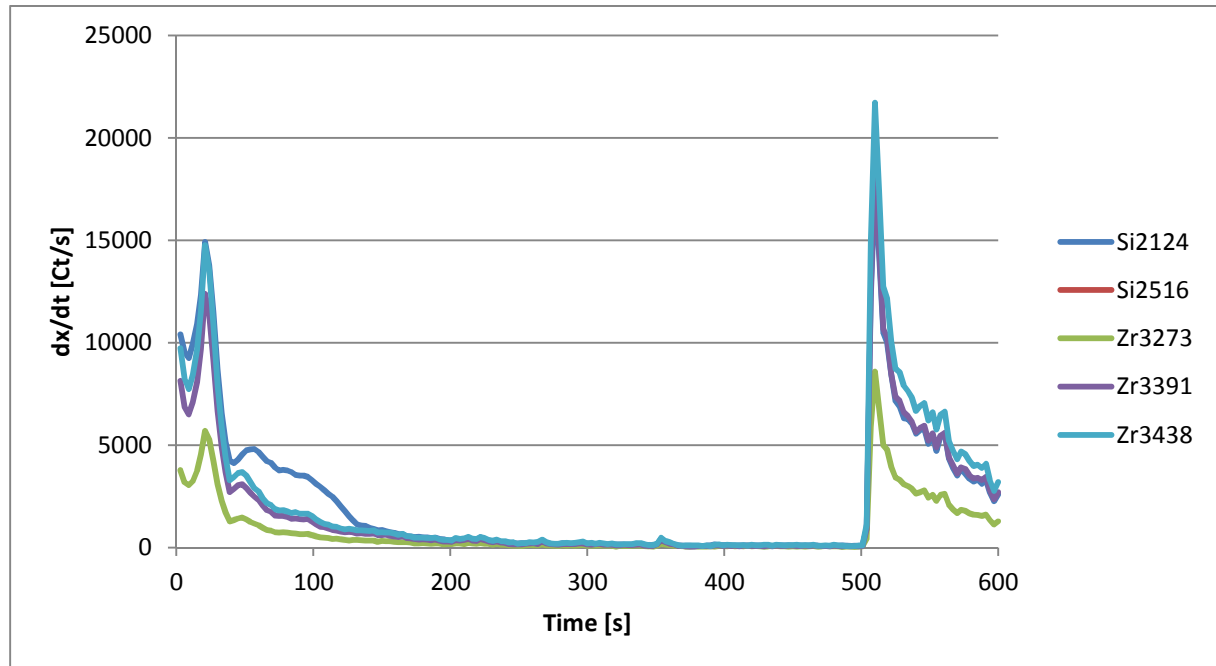


**Figure 73: Flushing out the suspension while particles are captured with an acoustic field at 6.66MHz.**

In Figure 73 it is visible that after the before measured 200 seconds the cell and tube volume is completely exchanged with the blank and the particle signal reaches basically zero and stays there due to the perfect capture of the particles still in the cell in the acoustic field. At 500 seconds the field is turned off and the captured particles are flushed out generating a nice enriched peak.

## 4. Conclusion

The simulation model of the cell seems to be reasonably accurate to help designing cell characteristics but not nearly good enough to predict the experimental results.

According to our experiments there are two possible ways of using the cell:

- 1) Loading the functionalized particles with analytes in the cell

The idea is to automatize the process of mixing the functionalized particles with analytes by first catching the particles in a fine acoustic field and load them with analytes by switching the inlet feed. This is possible with the current cell at the 6.666 MHz frequency due to a very fine acoustic field and a peristaltic pump and could be improved by using a syringe pump for better retention and less disturbances.

## 2) Enriching the loaded particles for measurement

The idea is to increase the signal strength of the ICP-OES by enriching the loaded particles over a certain timeframe to improve sensitivity of measurements.

This is hardly possible with the current cell due to insufficient retention, the syringe pump improved this application but the retention should still be improved.

All in all the goal of increasing reliability and reproducibility seems reachable by further developing this concept. Based on our knowledge it should be possible to replace some manual sample handling processes with an on-line ultrasonic resonator.

## 5. Outlook

There are many possible ways of trying to improve the cell.

On the fluid dynamic side a good flow characteristic with as little dead volume as possible and a constant flow speed seems essential and could be further improved through simulations and cell design. The acoustic impedance match with PDMS seems to be a good way for designing good fluid dynamics without losing acoustic advantages. A better material for the impedance match could be a material named Rho-c which is designed such that its impedance matches the impedance of water more closely.

On the acoustic side a better understanding of the amplitude displacement of the PZTs through further research with the vibrometer could lead to an improvement of the acoustic field by matching the PZT geometry. Also a better understanding of how to glue PZTs to the cell and which materials to use for the cell could optimize the strength of the acoustic field.

On the particle side it could be possible to increase their size through different synthesizing methods. As seen in the formulas and simulation the particle size is a very significant parameter for the retention.

The simulation could be improved by more accurate modeling especially by considering temperature effects which were basically ignored in our approach. Furthermore if one has more processing power it could be used to improve the mesh accuracy for better results.

The measurements processes could be completely automated for better usability, reproducibility and expressiveness.

## Acknowledgements

I want to express big thanks to Cosi & Felix for being an awesome project team and providing a cheerful and constructive work environment as well as their great commitment!

Another big thank you goes of course to my parents for enabling me to study.

Special thanks to my sister in law Niki and my brother Stefan for the LEGO parts and helping me in building the “automated cell turning machine”.

Thanks to my twin sister for her help in my eternal fight with languages and formatting skills in MS word.

## Bibliography

- [1] H. Bruus, “Acoustofluidics 1: Governing equations in microfluidics.,” *Lab Chip*, vol. 11, no. 22, pp. 3742–51, Nov. 2011.
- [2] M. Evander and J. Nilsson, “Acoustofluidics 20: Applications in acoustic trapping.,” *Lab Chip*, vol. 12, no. 22, pp. 4667–76, Oct. 2012.
- [3] M. Grosch, W. Burger, B. Handl, O. Doblhoff-dier, T. Gaida, and C. Schmatz, “Ultrasonic Separation of Suspended Particles - Part III : Application in Biotechnology,” vol. 84, pp. 815–822, 1998.
- [4] M. Brandstetter, “Ultrasonically enhanced in-line Attenuated Total Reflection (ATR) infrared absorption spectroscopy of suspensions,” Vienna University of Technology, 2009.
- [5] M. Groschl, “Ultrasonic Separation of Suspended Particles - Part I : Fundamentals,” no. October 1997, pp. 432–447, 1998.
- [6] M. Groschl, “Ultrasonic Separation of Suspended Particles - Part II: Design and Operation of Separation Devices,” pp. 632–642, 1998.
- [7] L. V. King, “On the Acoustic Radiation Pressure on Spheres,” *Proc. R. Soc. A Math. Phys. Eng. Sci.*, vol. 147, no. 861, pp. 212–240, Nov. 1934.
- [8] Y. Yosioka and K. Kawasima, “Acoustic radiation pressure on a compressible sphere,” *Acustica*, no. 5, pp. 167–173, 1955.
- [9] M. Grün and I. Lauer, “The Synthesis of Micrometer- and Submicrometer-Size Spheres of Ordered Mesoporous Oxide MCM-41,” no. 3, pp. 254–257, 1997.
- [10] G. Bauer, M.-A. Neouze, and A. Limbeck, “Dispersed particle extraction--a new procedure for trace element enrichment from natural aqueous samples with subsequent ICP-OES analysis.,” *Talanta*, vol. 103, pp. 145–52, Jan. 2013.
- [11] I. Leibacher, S. Schatzer, and J. Dual, “Impedance matched channel walls in acoustofluidic systems.,” *Lab Chip*, vol. 14, no. 3, pp. 463–70, Feb. 2014.
- [12] N. Laboratorium and G. Eindhoven-holland, “THE LONDON--VAN DER WAALS ATTRACTION BETWEEN SPHERICAL PARTICLES by H. C. H A M A K E R,” no. 1, 1937.

## Appendix

The idea to make the against gravity approach reasonable and reproducible through automating the turning process came fast. The realization took some time but at the time of writing this it became useable.

The design of the apparatus to fixate the cell and make it turnable by a motor was a creative process and difficult task due to shortages in available LEGO pieces. However Niki, Stefan and me managed to put together the device visible in Figure 74 by working through a challenging and funny Saturday. The device has a rotatable fork in the front and a LEGO motor on a platform to turn it which can be controlled by 4 wires.

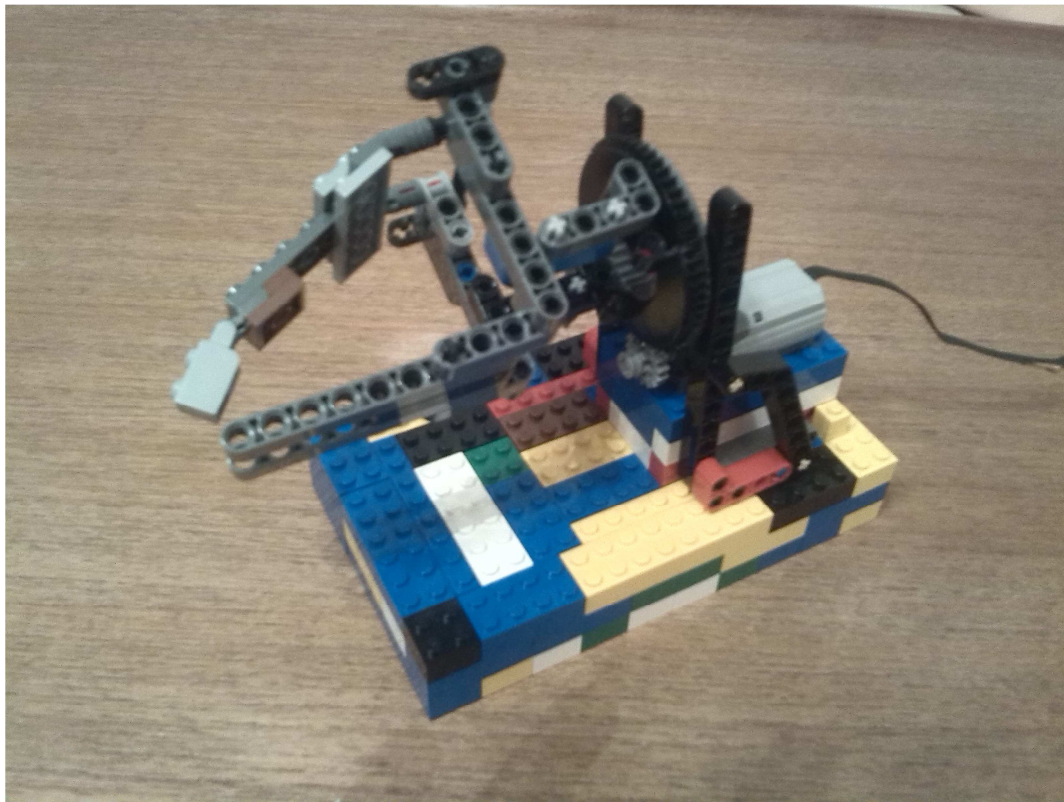


**Figure 74: LEGO construction with motor.**

In Figure 75 the Circuit diagram of the motor control is shown. It consists of a microcontroller (PIC16F627) for the central intelligence which was chosen because I still had it from a previous project. Additionally it has a L293D motor driver with included free-wheel diodes, a lightbarrier TCST2103 for signaling when to stop, one switch to signal the turning direction, one push button to signal the turning start and a 5V modulator MC7805ct to transform the 12V motor supply voltage into 5V supply for all logic components. As a failsafe method a potentiometer which is usually at 0 Ohm was included to lower the turning speed or even stop the motor from turning.

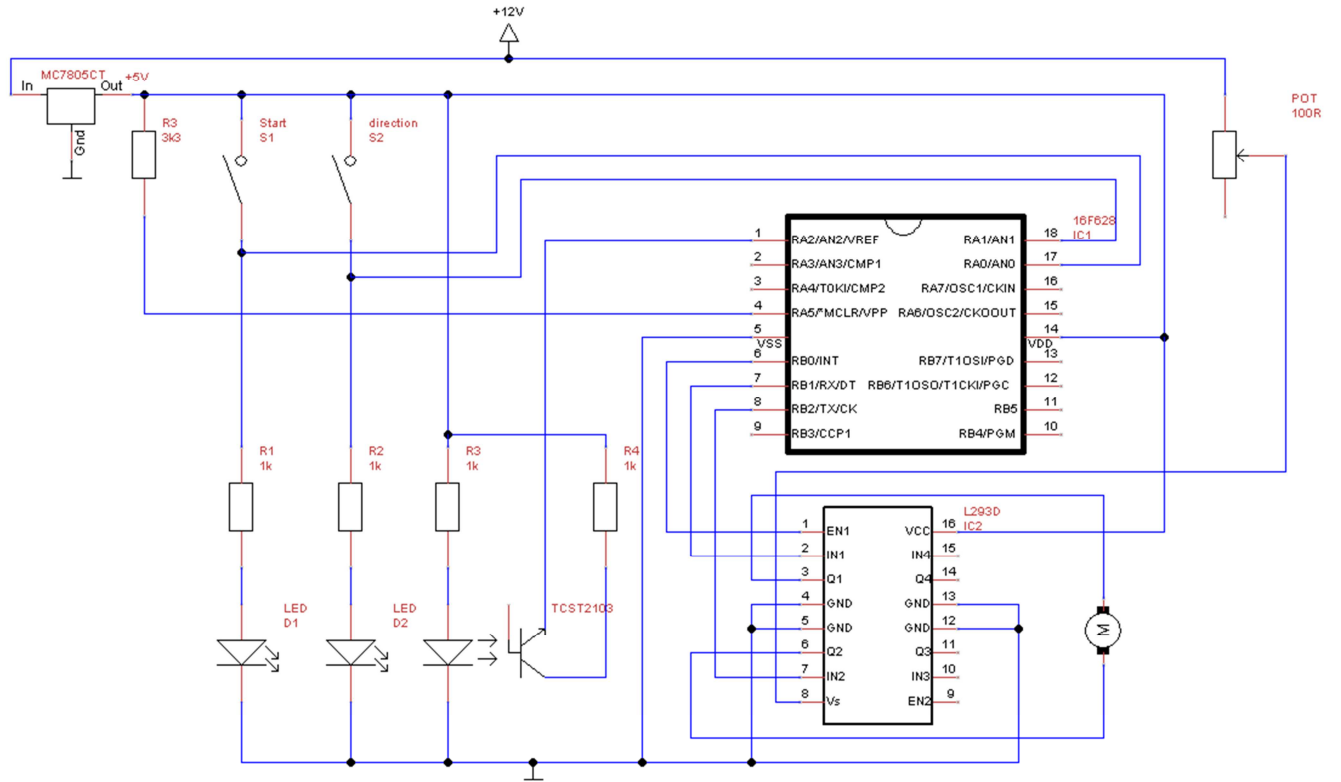


Figure 75: Motor circuit.

In Figure 76 the flow chart of the program code for the microcontroller is illustrated.

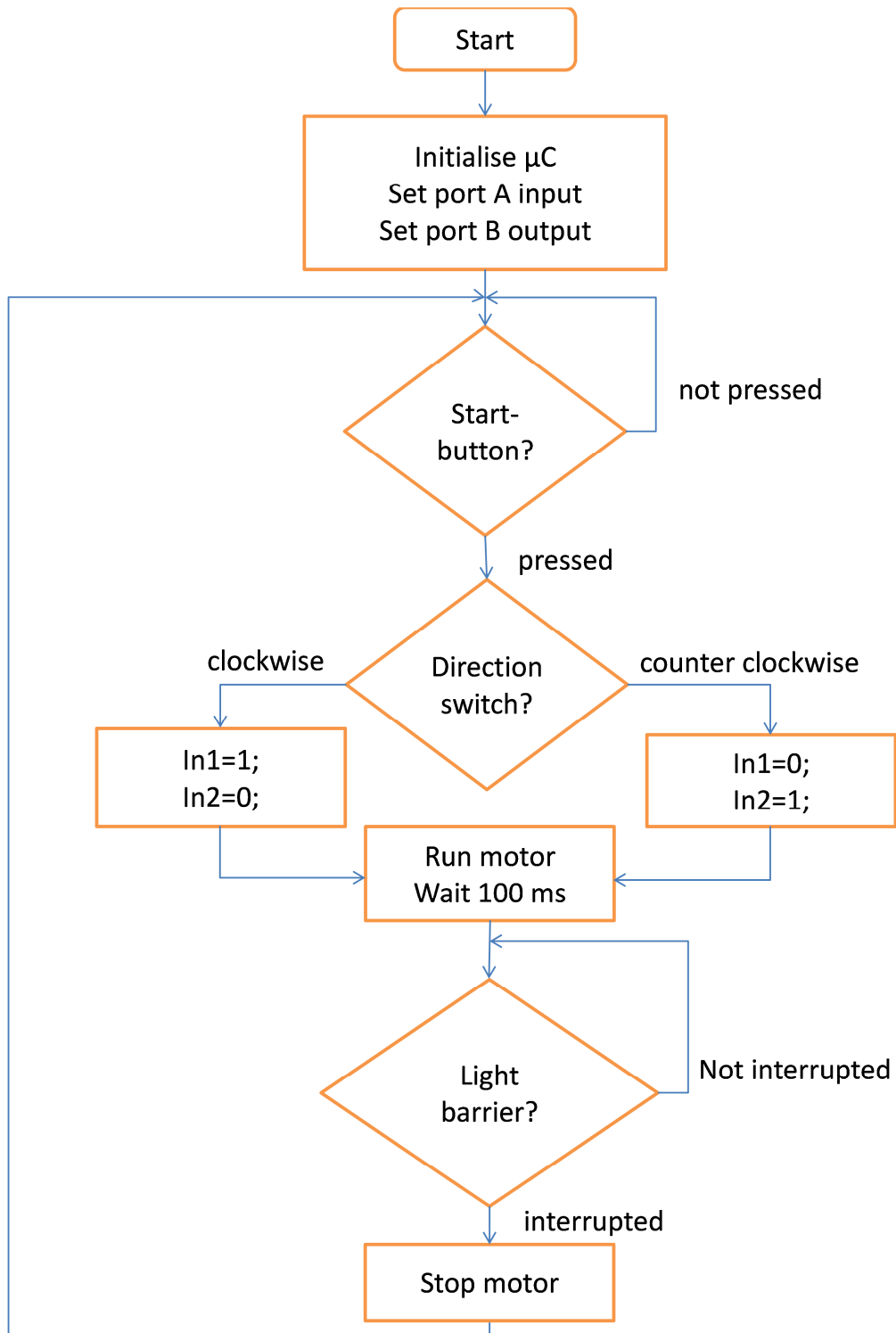
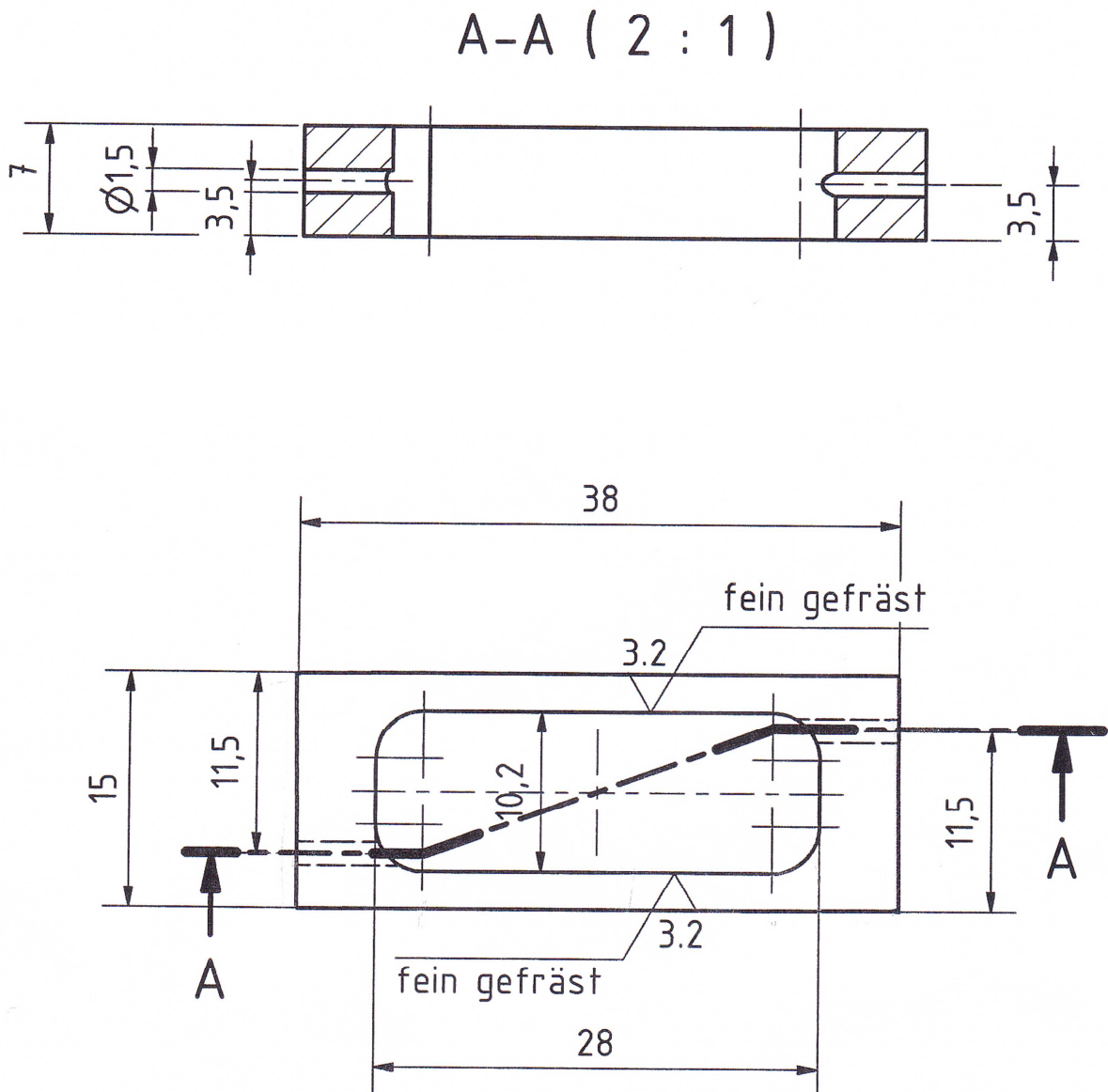


Figure 76: Flow chart of PIC16F627 program code.



**Figure 77: Cell2 design drawing.**

In the following pages there are attached PDF files of the PIC16F627 program code, the datasheet of the PZT PIC181 and a datasheet of the frequency generator SC 020, which is identically constructed as the purchased SC 010. The only difference is that the SC 010 has a lower but more precise power output.



```

/*
 * File:   main.c
 * Author: Lukas
 *
 * Created on 15. November 2013, 22:25
 */

#include <xc.h> // include standard header file
#include <htc.h>

// PIC16F627 Configuration Bit Settings
#pragma config FOSC = INTOSCIO // Oscillator Selection bits (INTRC
oscillator: I/O function on RA6/OSC2/CLKOUT pin, I/O function on
RA7/OSC1/CLKIN)
#pragma config WDTE = OFF // Watchdog Timer Enable bit (WDT disabled)
#pragma config PWRTE = ON // Power-up Timer Enable bit (PWRT enabled)
#pragma config MCLRE = ON // RA5/MCLR pin function select (RA5/MCLR
pin function is MCLR)
#pragma config BOREN = ON // Brown-out Reset Enable bit (BOD Reset
enabled)
#pragma config LVP = OFF // Low-Voltage Programming Enable bit
(RB4/PGM pin has digital I/O function, HV on MCLR must be used for
programming)
#pragma config CPD = OFF // Data Code Protection bit (Data memory
code protection off)
#pragma config CP = OFF // Code Protection bits (Program memory
code protection off)
//_BODEN_ON & _CP_OFF & _DATA_CP_OFF & _PWRTE_ON & _WDT_OFF & _LVP_OFF &
_MCLR_ON & _XT_OSC

// Definitions
#define _XTAL_FREQ 4000000 // this is used by the __delay_ms(xx) and
__delay_us(xx) functions

/* Testboard
;SW1 is triggering RA0
;SW2 is triggering RA1
;SW3 is triggering RA2
;SW4 is triggering RA3
*/

/*
RA0 is the start button for turning
RA1 is the switch for the direction forward/backward
RA2&RA3 are the switches for how long its turning

RB0 is the enable Pin at the L298 H-Bridge
RB1 is the Input1 Pin at the L298 H-Bridge
RB2 is the Input2 Pin at the L298 H-Bridge
*/

int main(void)
{
    int waittime=0;

```

```

int i=0;

CMCON = 0b00000111;
OPTION_REG = 0b11010111;
INTCON = 0x00;
TRISB = 0b00000000;    // Port B output
TRISA = 0b11111111;    // Port A input

//PORTA=0x00;
PORTB=0x00;

while(1) //endless loop
{
    //if(RA3==1) //enable-all switch?

    if(RA0==1) // Start-switch pressed?
    {
        if(RA1==1) // Direction switch on which side?
        //__delay_ms(10); // wait time
        //if(i==0) // always switch rotation direction
        {
            RB1=1; // In1=1
            RB2=0; // In2=0
            //i=1; // remember direction
        }
        else
        {
            RB1=0; // In1=0
            RB2=1; // In2=1
            //i=0; // remember direction
        }

        RB0=1; // enable
        __delay_ms(100); // wait time

        while (RA2==1) // till photo sensor blocked?
        {
            //__delay_ms(1); // wait time
        }

        RB1=0; // In1=0
        RB2=0; // In2=0
        RB0=0; // disable
    }
}

return 0;
}

```

Complete material data set PIC181					
Coefficient	Unit	Value	Coefficient	Unit	Value
Density	kg/m <sup>3</sup>	7,85E+03	N1	Hzm	1646
			N3	Hzm	2004
Qm		2200	N5	Hzm	1222
			Np	Hzm	2265
ε 11Tr		1224	Nt	Hzm	2302
ε 33Tr		1135			
ε 11Sr		740	d31	m/V	-1,08E-10
ε 33Sr		624	d33	m/V	2,53E-10
tan δ		3,0E-3	d15	m/V	3,89E-10
k31		0,315	g31	Vm/N	-1,08E-02
k33		0,662	g33	Vm/N	2,52E-02
k15		0,629	g15	Vm/N	3,59E-02
kp		0,551			
kt		0,459	e31	N/Vm	-4,50
			e33	N/Vm	14,70
Poisson (σ)		0,35	e15	N/Vm	11,00
s11E	m <sup>2</sup> /N	1,175E-11	c11E	N/m <sup>2</sup>	1,523E+11
s33E	m <sup>2</sup> /N	1,411E-11	c33E	N/m <sup>2</sup>	1,341E+11
s55E	m <sup>2</sup> /N	3,533E-11	c55E	N/m <sup>2</sup>	2,830E+10
s12E	m <sup>2</sup> /N	-4,070E-12	c12E	N/m <sup>2</sup>	8,909E+10
s13E	m <sup>2</sup> /N	-4,996E-12	c13E	N/m <sup>2</sup>	8,547E+10
s44E	m <sup>2</sup> /N	3,533E-11	c44E	N/m <sup>2</sup>	2,830E+10
s66E	m <sup>2</sup> /N	3,164E-11	c66E	N/m <sup>2</sup>	3,161E+10
s11D	m <sup>2</sup> /N	1,058E-11	c11D	N/m <sup>2</sup>	1,550E+11
s33D	m <sup>2</sup> /N	7,930E-11	c33D	N/m <sup>2</sup>	1,664E+11
s55D	m <sup>2</sup> /N	2,134E-11	c55D	N/m <sup>2</sup>	4,686E+10
s12D	m <sup>2</sup> /N	-5,235E-12	c12D	N/m <sup>2</sup>	9,182E+10
s13D	m <sup>2</sup> /N	-2,268E-12	c13D	N/m <sup>2</sup>	7,061E+10
s44D	m <sup>2</sup> /N	2,134E-11	c44D	N/m <sup>2</sup>	4,686E+10
s66D	m <sup>2</sup> /N	3,164E-11	c66D	N/m <sup>2</sup>	3,161E+10

Values are only for information - no specification!  
Simulation purpose

The data in the table was determined using testbodies with geometries and dimensions in accordance with European Standard EN 50324 2, and are typical values.

Singular parameters can deviate from catalogue values, because they were measured at samples which were taken from one block of ceramics according to the sequence of IEC483 to get maximum consistency.

Catalogue values reflect the statistical distribution of each individual specification in production and therefore also take into account spreading from material batch to material batch.



**sonosep  
Controller SC 020**

features

- + variable high frequency generator up to 7 MHz
- + integrated power output amplifier up to 20 W<sub>rms</sub>
- + drives any load impedance
- + true power output monitor
- + automated frequency & power tracking function
- + integrated variable timer for discontinuous operation
- + I/O interface (isolated) for remote control and pump synchronisation
- + automatic overload and short circuit protection

specifications

frequency range: 1 MHz to 3 MHz (standard)  
70 kHz to 7 MHz (absolute limits for customized range)

true power output: 20 W<sub>rms</sub> max. (@ 1-3 Mhz)  
HF voltage output: 30 V<sub>peak</sub> max. (request transformers for higher output amplitudes)  
HF current output: 2 A<sub>peak</sub> max.

timer function: 10 sec to 600 sec (Run time)  
1 sec to 60 sec (Stop time)

mains supply: 115V/2A or 230V/1A; 50-60 Hz

dimensions: 240 x 140 x 285 mm; 6.6 kg

more specifications: contact info@sonosep.com  
or visit www.sonosep.com

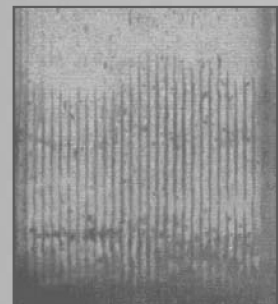
contact: **SinePhase Instruments GmbH**

Waldgasse 7  
A-2371 Hinterbruehl  
Austria/EUROPE  
tel: (Int+43) 650 4625432  
fax: (Int+43) 2236 493355

U.S. office: **SinePhase USA**

2112 Oak Grove Rd.  
Walnut Creek, CA 94598, USA  
tel: (Int+1) 925 6833673

web&mail: [www.sinephase.com](http://www.sinephase.com)  
[info@sinephase.com](mailto:info@sinephase.com)



Suspended coil in a stable ultrasonic standing wave field  
Power source: SC 020 (2-1 MHz)